博士学位論文

Efficient Creation of Ultra-High-Energy-Density States by Magnetized Fast Isochoric Laser Heating Scheme

外部磁場導入レーザー高速加熱法による効率的な超高エネルギー密度状態の生成

大阪大学大学院　理学研究科　物理学専攻

24B14807

Shohei Sakata

坂田　匠平

Abstract

Creation of high energy density (HED) states in the laboratory by a large energy, high power, high intensity laser is expected as a new approach to investigate the equation of state (EOS), atomic states nuclear reactions and energy transport in the HED stars. In particular, inertial confinement fusion (ICF) is an ultimate application of such extreme plasmas.

A few mm-scale spherical capsule, which contains deuterium-tritium (DT) fusion fuel ice layer, is used in the ICF. In the laser indirect-drive approach, the capsule surface is uniformly irradiated by X rays in a high-Z metal enclosure (hohlraum) driving a sequence of converging shock waves, and then the fusion fuel is compressed more than 1000 times solid density. Adiabatic compression heats up a DT gas initially filling the capsule interior, which then becomes the ignition spark at the final stage of the compression. The scientific break-even, energy released by fusion reaction exceeds energy contains in the compressed fusion fuel, was achieved on National Ignition Facility, however the pathway to the ICF ignition is still unclear.

Fast isochoric heating, also known as fast ignition, of a pre-compressed core, was proposed as an alternative approach to the ICF ignition that avoids the ignition quench caused by the mixing because the hot spark is generated not by the adiabatic compression but by an external energy injection within an inertial confinement time of the pre-compressed core (< 100 ps). Relativistic intensity laser pulses (> 1.37×10^{18} Wμm^2 /cm^2) efficiently produce relativistic electron beams (REB) as the external energy source by laser-plasma interactions. The cone-attached-fuel approach brings the REB generation point closer to the core by excluding the corona plasma from the path of the relativistic intensity laser pulses.

Three critical problems have been recognized as obstacles to the efficient fast heating with the REB. The first problem is that the REB becomes too energetic to heat the core in a long scalelength pre-plasma filled in the cone, the second one is that a part of the REB is scattered and absorbed in a high-Z cone tip. The third one is that the REB has a large divergence of 100 deg. as a typical full-angle, so that only a small fraction of the diverged REB collides with the core.

The long scale-length pre-plasma filled in the cone is produced by prepulse and foot pulses of the heating laser and also by the cone breakup due to high pressure of a plasma surrounding the cone. 7% of the heating efficiency was attained at OMEGA laser facility with an ignition-scale large area density (ρR ~ 0.3 g/cm^2) core after reducing the pre-plasma formation in the cone, however, the aforementioned second and third critical problems still remain to be resolved.

Here, we have introduced two novel experimental techniques. A solid ball target is used for making an open-tip cone utilizable along with the plasma compression. The solid ball compression does not generate preceding shocks and rarefactions travelling ahead of the dense shell, therefore a closed-tip is not required for preventing the cone inside from filling with a hot

plasma. In addition, a relatively cold and dense core can be produced stably by using the solid ball target. The cold core enables us to visualize REB transport region in a dense core by using monochromatic Cu-Kα imaging technique without significant energy shift of the Cu-Kα photon energy due to ionization of Cu atoms.

The other technique is a laser-driven capacitor coil target to generate kilo-tesla magnetic field. Strength of the magnetic field was measured on GEKKO-XII, LULI2000, and OMEGA-EP laser facilities. Some of the experimental results revealed that 600 – 700 T magnetic field was generated by using a tightly focused kilo-joule and nano-second infrared (λ_L = 1053 nm) laser beam. Application of external magnetic fields to the path of a REB guides the diverged REB to the dense core. The magnetic field lines are bent due to magnetic field compression associated with the ball compression. The REB can be focused by a moderate guiding field (Rm < 10) without significant loss caused by the magnetic mirror effect, here Rm is the mirror ratio. The mirror ratio is relatively moderate (Rm ~ 3) in the solid ball compression compared to the gas-filled thin shell implosion because of small magnetic Reynolds number in a shock compressed solid region.

The laser-to-core couplings were experimentally measured by varying the experimental conditions; heating laser energy, injection timing of heating laser, application of the external magnetic field or not, and open- or closed-tip cones. The coupling was calculated from the absolute number of Cu-Kα X-ray (8.05 keV) photons emitted from Cu-contained pre-compressed hydrocarbon core. Cross-sections of electron-impact K-shell ionization have a similar dependence on electron energy as collisional energy loss. The two are essentially the same process but with a different threshold energy. Collisional deposition of REB energy (J) in a Cu-contained-core can be obtained with number of Cu-Kα photons (photons/sr) emitted from the core with a correlation factor. The method employs a kilo-tesla-level magnetic field that is applied to the transport region from the REB generation point to the core which results in guiding the REB along the magnetic field lines to the core. 7.7 ± 1.3 % of the maximum coupling was achieved even with a relatively small radial area density core (ρR ~ 0.1 g/cm^2). The guided REB transport was clearly visualized in a pre-compressed core by using Cu-Kα imaging technique. A simplified model coupled with the comprehensive diagnostics yields 6.2% of the coupling that agrees fairly with the measured coupling. This model also reveals that an ignition-scale areal density core (ρR > 0.3 g/cm^2) leads to much higher laser-to-core coupling (> 10%), this coupling is much higher than that obtained with the current ICF scheme.

Contents

1. Introduction

We are exploring 'extreme states', ultra-high or low speed phenomena, temperature states, density materials, pressure etc., which bring us to new insights. In particular, creation of extremely high-energy-density (HED) state in the laboratory has a large potential for investigation of astrophysics [1,2], planetary science [3,4] and nuclear fusion energy research [5,6]. Figure 1.1 shows the ρ-T diagram of density and temperature. 1 Mbar pressure is equivalent to the pressure inside planetary cores. 1 Gbar pressure is near the pressure inside the sun. Realization of controlled fusion ignition plasma is ultimate challenge for HED plasma science.

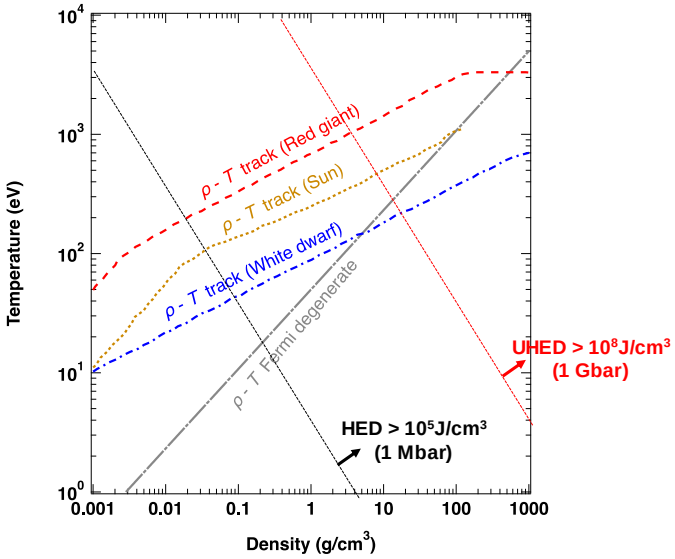

Figure 1.1 Diagram for parameter space of density vs temperature.

1.1 Inertial confinement fusion (ICF)

One of the most attractive scheme to achieve controlled fusion ignition plasma is inertial confinement fusion (ICF) proposed by Nuckolls *et. al.,* [7]. In this scheme, mm-scale Deuterium (D) – Tritium (T) capsule is irradiated by a large number of laser or X rays. The outer surface of the capsule is accelerated inward by ablation pressure due to reaction force of plasma expansion (implosion). The accelerated shell is converged into the central spot, forming a so-called hot spot which lasts within the stagnation time of 100~300 ps. The alpha particles with the energy 3.5 MeV produced by DT nuclear fusion.

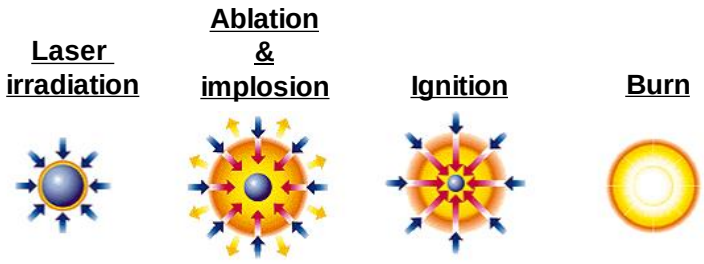

Figure 1.2 Illustration of the process of ICF.

The temperature of several tens of keV (1 eV = 11680 K) is required to overcome the Coulomb barrier between the nuclei. The produced alpha particles from fusion reactions deposits their energy into the ignited DT plasma, which increases its temperature and the fusion reaction rate. The amplification of the fusion reaction rate by plasma self-heating (or alpha-heating) leads to a fusion energy output greater than the input energy.

The DD, DT and TT reactions are following

$$D + D \rightarrow T(1.01\ \text{MeV}) + p(3.03\ \text{MeV}) \quad (1\text{-}1)$$

$$D + D \rightarrow He^3(0.82\ \text{MeV}) + n(2.45\ \text{MeV}) \quad (1\text{-}2)$$

$$D + T \rightarrow \alpha(3.5\ \text{MeV}) + n(14.1\ \text{MeV}) \quad (1\text{-}3)$$

$$T + T \rightarrow \alpha + 2n + 11.3\ \text{MeV} \quad (1\text{-}4)$$

Cross sections of above nuclear reactions are described in Figure 1.3. Two DD reactions branches with the same probability. The DT reaction cross sections is about 100 times larger than the DD reaction.

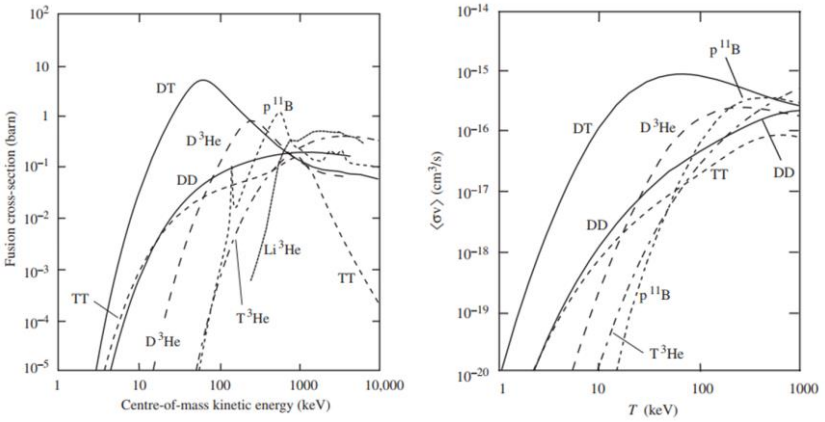

Figure 1.3 Fusion cross-sections and center-of-mass energy for
Image taken from Azteni [8]

1.1.1 Burn efficiency

Reactivity is defined as the probability of reaction per unit time and unit density of the nuclei. The averaged reactivity can be written by

$$\langle \sigma v \rangle = \int_0^\infty \sigma(v) v f(v) dv \tag{1-5}$$

v is the relative velocity of the nuclei and $f(v)$ is the distribution function of the relative velocities.

The number of fusion reactions per unit time is given by

$$\frac{dN_{fus}(t)}{dt} = \langle \sigma v \rangle n_D(t) n_T(t) V(t) \tag{1-6}$$

Where, $V(t)$ is the volume of fuel, $n_D(t)$ is the number density of deuterium, $n_T(t)$ is the number density of tritium.

$$\frac{V(t)}{V_0} = \left(1 - \frac{c_s t}{R_0}\right)^3 \tag{1-7}$$

c_s is sound velocity. Integrating Equation 1-7 over the time interval in which the fuel is confined leads to

$$\int_0^{\tau_{conf}} \frac{V(t)}{V_0} dt = \frac{R_f}{4c_s} \tag{1-8}$$

We obtain

$$N_{fus} = \frac{{n_0}^2 \langle \sigma v \rangle V_0}{4} \cdot \frac{R_0}{4c_s} \tag{1-9}$$

Burn efficiency can be written by

$$\Phi \simeq \rho R_f / H_B \tag{1-10}$$

Here, $H_B = 8c_s m_f / \langle \sigma v \rangle$

1.1.2 Hot spot and ignition temperature

In order to trigger ignition, self-heating by alpha particle must be larger than radiation, heat conduction and plasma expansion.

Self-heating power per unit time and volume is given by

$$P_\alpha = n_D n_T \langle \sigma v \rangle E_\alpha \quad erg/s \cdot cm^3 \tag{1-11}$$

Here, E_α is the energy of alpha particle.

Bremsstrahlung emission power per unit time and volume is written by

$$P_{br} = \frac{32\pi}{3} g \left(\frac{2\pi T}{3m_e} \right)^{1/2} \frac{Z^2 e^6}{m_e c^3} n_e n_i = 3.05 \times 10^{23} Z^3 \rho^2 T_{\mathrm{keV}}^{1/2} \ \ erg/s \cdot cm^3 \tag{1-12}$$

g is Gaunt factor, T_{keV} is ion temperature in keV.

Nuclear reaction and Bremsstrahlung radiation are binary collision process, resulting their power is proportional to square of the density. The self-heating and bremsstrahlung radiation can be compared without density dependence. When we consider only radiation energy loss, the threshold temperature for ignition is 4.3 keV.

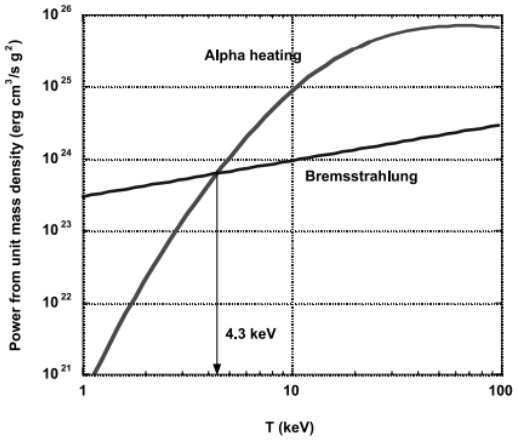

Figure 1.4 The threshold temperature for ignition. The power from alpha-heating overtakes the Bremsstrahlung loss at 4.3 keV. Image taken from Azechi [9]

1.1.3 Ignition condition

$$2 \cdot \frac{3}{2}\frac{\rho(t)}{m_{\mathrm{DT}}}\frac{\mathrm{d}T(t)}{\mathrm{d}t} = P_h(t) + P_\alpha(t) f_\alpha - \left[P_w(t) + P_e(t) + P_r(t)\right] \tag{1-13}$$

$$P_\alpha = A_\alpha \rho^2 \langle \sigma v \rangle, \qquad A_\alpha = 8.04 \times 10^{40} \ \ erg/g^2 \tag{1-14}$$

$$P_r = A_r \rho^2 T^{1/2}, \qquad A_r = 3.05 \times 10^{23} \ \ erg/g^2$$

When the volume of hot spot at pressure p changes,

$$P_w = \frac{3pv_{ex}}{R} = A_w \frac{3\rho T v_{ex}}{R}, \qquad A_w = 2.3 \times 10^{15} \ \ erg/g^2 \tag{1-15}$$

$$P_e = \frac{\kappa \nabla TS}{V} \approx A_e \frac{T^{7/2}}{R^2}, \qquad A_e = 4.1 \times 10^{19} \ \ erg/g^2 \tag{1-16}$$

$$\left(A_\alpha \langle \sigma v \rangle - A_r \sqrt{\overline{T}}\right)(\rho R)^2 - A_u v\mathrm{T} \cdot \sigma R - A_e T^{7/2} > 0 \tag{1-17}$$

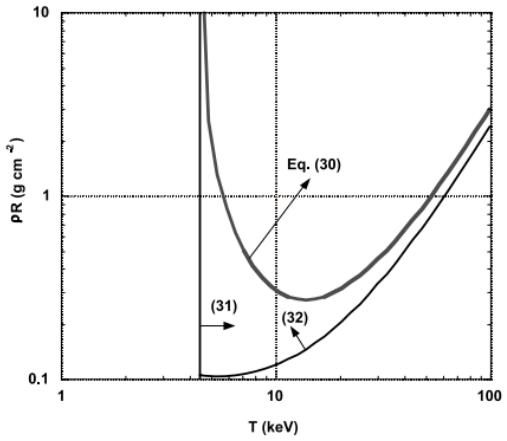

Figure 1.5

Image taken from Azechi [9]

1.2 Direct drive ICF [10]

The first ICF concept proposed by Nuckolls *et. al.,* is direct drive scheme. In direct drive ICF, multiple laser beams are illuminated on the surface of the capsule, which leads to maximize the energy coupling to the imploding DT fuel compared with other external drivers. The energy coupling from the drive laser to the DT fuel is about five to six times higher than indirect drive. For example, when a capsule is imploded by 2 MJ laser irradiation with ultraviolet is expected to acquire about 100 kJ of fuel kinetic energy compared to ~16 kJ of existing indirect-drive NIF targets. A typical target used in direct drive ICF experiments at the OMEGA laser facility is presented in Figure 1.3. The spherical capsule consists of an outer plastic shell enclosing an inner ice layer of DT filled with DT gas.

Direct drive scheme requires a spatial uniformity of laser beams with small scales (much smaller than the capsule size) to suppress hydrodynamic instabilities. A thin ablator layer is used in direct drive ICF due to the low mass ablation rate, thereby providing relatively less protection of the inner DT fuel layer from hot-electron and/or radiation preheating.

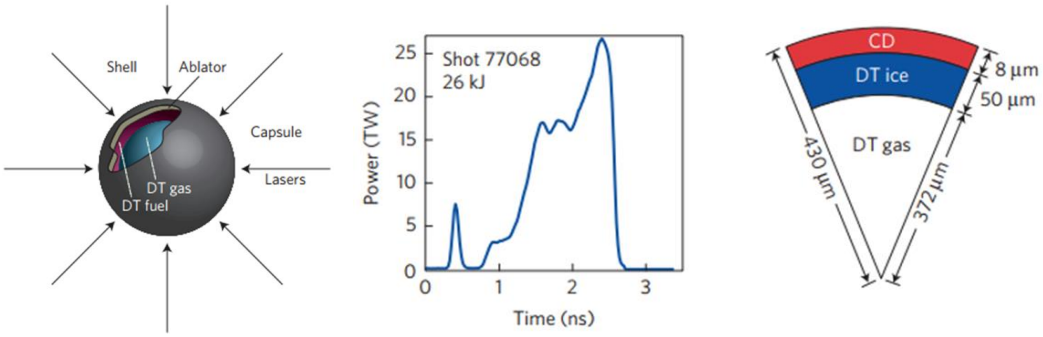

Figure 1.6 Schematic view of a concept of direct drive ICF scheme (left). Typical time evolution of the driving laser pulse (middle) and a shell target (right).
Images taken from Betti and Hurricane [11]

1.3 Indirect drive ICF [12]

Figure 1.7 shows a typical target used in indirect drive ICF experiments on the National ignition facility (NIF). The target consists of a gold hollow cylinder (hohlraum) and a spherical capsule. The cylindrical hohlraum encloses the ICF capsule supported by a thin (15–100 nm) membrane (the tent). Laser beams are irradiated into the wall of the hohlraum through the laser entrance holes (LEHs).

Whereas the bath of X-rays in the hohlraum is free of small-scale nonuniformities, laser beams exhibit speckle patterns with large variations in laser intensity. In direct drive, this leads to imprinting of small-scale laser-intensity patterns on the target surface.

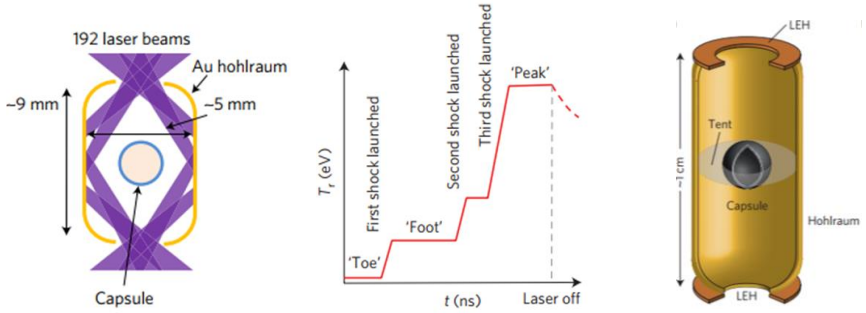

Figure 1.7 Schematic view of a concept of Indirect ICF (left). Three steps laser pulse for implosion (middle).
Image taken from Betti and Hurricane [11].

1.4 Current statue of ICF experiments

1.4.1 Indirect drive [13, 14]

Notable accomplishments in indirect drive ICF experiments are following,

1. Achieving more than a doubling of the fusion yield due to α-particle self-heating and fusion neutron yields of 26 kJ.
2. Demonstration of DT implosions that range in levels of fuel compression from $\rho R = 0.6$ g cm^{-2} to $\rho R = 1.1$ g / cm^{-2} with fuel velocities in excess of 380 km s^{-1}, with no indications of mixing of ablator material into the hotspot.

1.4.2 Direct drive [15]

Notable accomplishments in direct drive ICF experiments are following,

1. Demonstrating hotspot pressures in excess of 50 Gbar at temperatures of about 3.6 keV and neutron yields of about 5×10^{13} with approximately 26 kJ of laser energy.
2. Demonstrating close to one-dimensional areal densities of about 0.2 g cm^{-2} at adiabats of ~4 and implosion velocities of about 360 km s^{-1}
3. Demonstrating implosion performance that scales hydrodynamically to alpha-heating levels of about 2× in yield amplification at 1.9 MJ of laser energy.

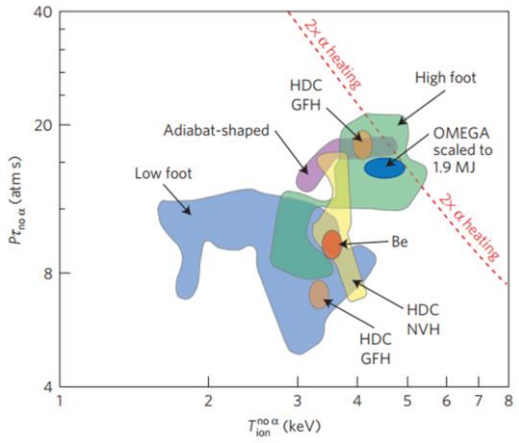

Figure 1.8 Lawson parameter Pt and ion temperature Tion.

Image taken from Betti and Hurricane [11]

1.4.3 Critical issue for current ICF experiments

Figure 1.9 shows X-ray images of hot spot at bang-time, reconstructed images and neutron images from current ICF experiment on NIF laser facility. These toroidal hot spot shape indicates that the hot spot pressure is quenched by localized thin spot due to Rayleigh-Taylor instabilities.

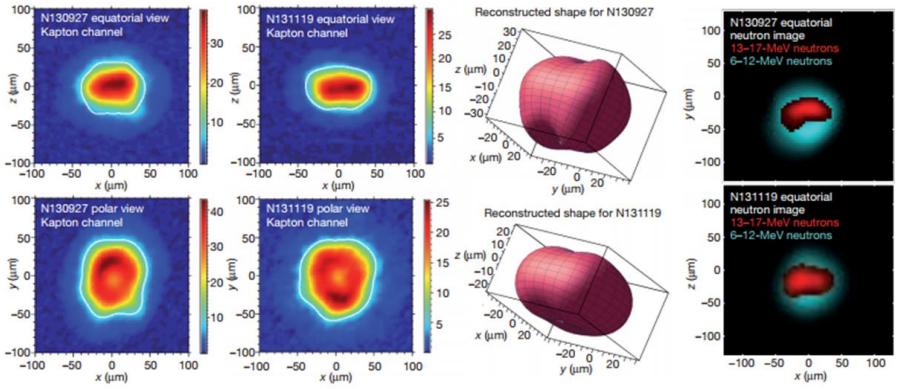

Figure 1.9 X-ray images of hot spot at bang-time (left side), reconstructed 3D images (middle) and neutron images (right). Image taken from Hurricane [11]

1.5 Concept of fast ignition (FI)

Fast ignition (FI) was proposed by Tabak *et. al.,* [15] in 1994 as an alternative scheme of ICF. A schematic view of a concept of fast ignition (FI) is shown in Figure 1.9. In FI scheme, compression of a fuel and heating of a compressed fuel stages are separated. First, a DT fuel capsule is imploded by multiple laser beams with a nano seconds pulse duration. A relatively low temperature, high-density fuel (core plasma) is assembled isochorically. Second, a high-intensity, short-pulse laser is injected into the dense core plasma at the maximum compression timing to generate a relativistic electron beam (REB) [16], which deposits it's energy into the dense core plasma. Finally, an intense localized heating by collimated REB triggers ignition. This scheme enables to avoid the fuel mixing due to hydrodynamic instability in principle.

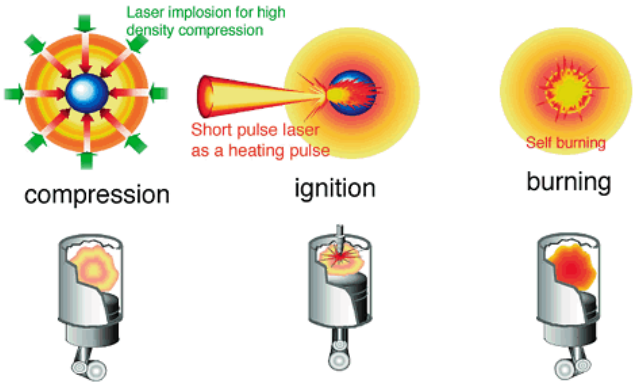

Figure 1.10 Schematic view of a concept of fast ignition scheme. FI scheme is often compared to a gasoline engine cycle (lower side).

1.5.1 Required energy for ignition [17]

In FI scheme, the hot spot is

Atzeni's ignition conditions

$$E_{opt} = 18\left(\frac{\rho}{300\mathrm{gcm}^{-3}}\right)^{-1.85} \quad \mathrm{kJ} \tag{1-18}$$

$$I_{opt} = 6.8\times10^{19}\left(\frac{\rho}{300\mathrm{gcm}^{-3}}\right)^{0.95} \quad \mathrm{Wcm}^{-2} \tag{1-19}$$

$$t_{opt} = 21\left(\frac{\rho}{300\mathrm{gcm}^{-3}}\right)^{-0.85} \ \mathrm{ps} \tag{1-20}$$

$$r_{opt} = 21\left(\frac{\rho}{300\mathrm{gcm}^{-3}}\right)^{-0.97} \ \mu\mathrm{m} \tag{1-21}$$

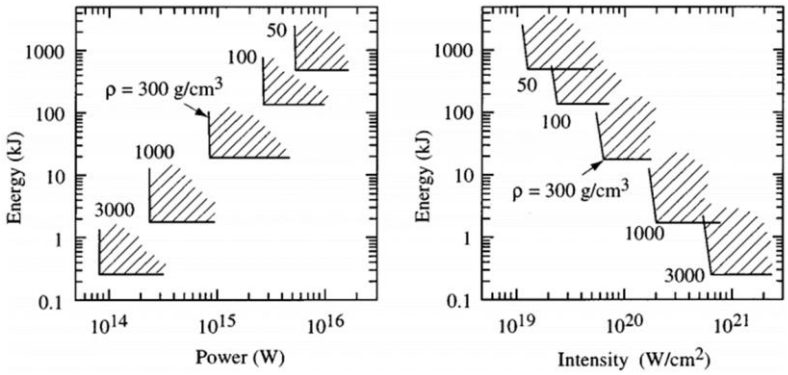

Figure 1.11 Required pulse parameters for fast ignition.
Image taken from S. Atzeni [17]

1.5.2 Channeling concept

A schematic view of channeling concept for FI is shown in Figure 1.12. A high-intensity pulse of 10^{17}–10^{19} W cm^2 with a duration of 100 ps creates a channel in the low-density corona plasma produced by implosion. During this "hole-boring" [16] process, the ponderomotive force associated with the transverse field gradient of the high-intensity channeling beam pushes the critical surface in the direction of the imploded dense core plasma. At the maximum compression, a 10^{20}–10^{21} W/cm^2 ignitor laser pulse with 10 ps duration is injected into the critical surface pathing through the channel formed by the hole-boring laser pulse. The ignitor pulse produces large amounts of energetic MeV electrons. The deposited

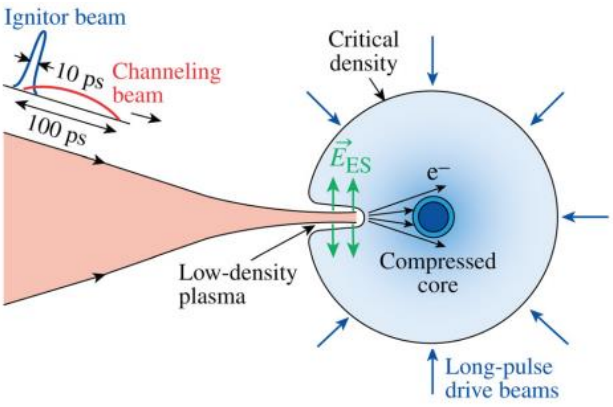

Figure 1.12 Illsutration of the channeling concept.
Image taken from J.-H. Yang and R. S. Craxton [11]

Figure 1.13 shows the time evolution of the laser light transmitted though the low-density plasma (electron density ~ 10^{20} / cm^3) and cross-sectional images of transmitted laser light with an intensity at 5×10^{14} W /cm^2 for different time *t* in the laser pulse relative to the peak of the laser pulse. Propagation of the laser light in a low-density plasma is unstable, which cannot deliver its energy into the dense plasma efficiently.

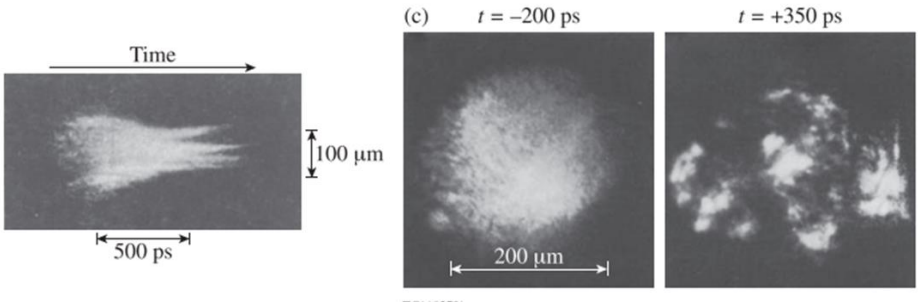

Figure 1.13 A streaked image of the spatial profile of laser light transmitted through a Bi plasma (left). Cross-sectional images of transmitted laser light with an intensity at 5×10^{14} W /cm^2 for different time *t* in the laser pulse relative to the peak of the laser pulse (left).
Images taken from Coe *et al.,* [18, 19]

1.5.3 Cone-in-shell target concept [20]

A cone-in-shell target was proposed by Kodama, *et, al*., [20] to eliminate the interaction between the coronal plasma that enables a stable propagation. Figure 1. 13 shows a photograph of the cone-in-shell target, a typical time-integrated X-ray image of imploded deuterated-polystyrene (CD) shell without injection of the heating laser and density profile of the imploded plasma.

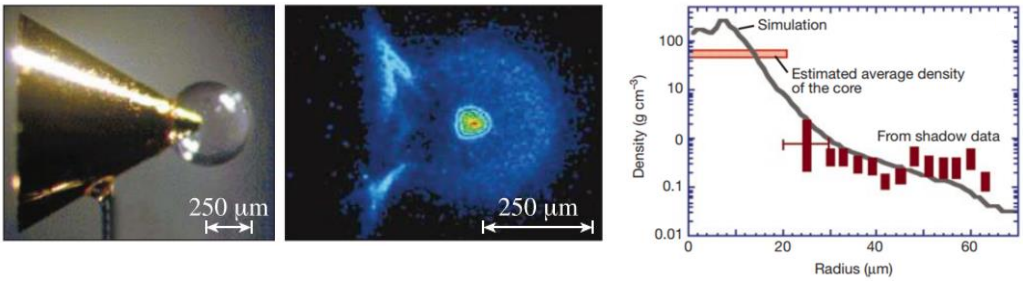

Figure 1.14 Photograph of a cone-in-shell target (left side). Time integrated X-ray image of (middle) The line represents the temporal profile of the average density of the compressed plasma from a hydrodynamic simulation (right side). Images taken from Kodama *et, al*., [20]

1000 times neutron yields enhancement was observed when high-intensity short-pulse laser was injected into the inside, whose value was higher than without injection of heating laser pulse. However, the process of energy deposition by REB into the imploded core plasma was unclear from this experiment.

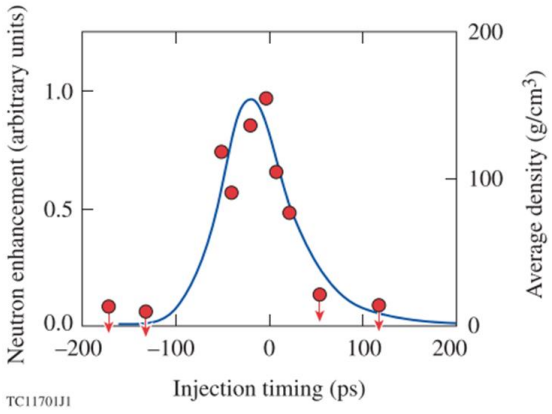

Figure 1.15 Normalized neutron yields enhancement as a function of injection timing of the heating laser. Images taken from Kodama *et, al*., [21]

1.6 The energy coupling from laser to core plasma in FI experiments

The energy coupling from laser to core plasma is the most important parameter in FI experiment. Characterization of key parameters with an accuracy to determine the energy coupling are required.

1.6.1 DD fusion neutron yields measurement using cone-in-shell target [22]

The energy coupling from laser to core plasma is inferred by neutron yields enhancements between shots, with and without the heating laser. By approximating the energy size and the density of the region where these fast electrons deposit their energy, the necessary energy required to increase the temperature by the measured difference can be calculated.

Most of the fast electrons that were transmitted through the cone wall deposited their energy in the lower-density plasma close to the tip of the cone. From Figure 1.16 (right), the peak neutron-production density occurred at the core in the absence of hot electrons.

With hot electrons, the neutron-production density is largest just to the left of the tip of the cone (Z = 60 um). The integrated simulation shows that 3.5 % of the laser energy was coupled into the imploded core plasma by REB, which corresponds to a neutron yield of 1.4 $\times 10^7$. Some fraction of REB does not contribute to deposit their energy into the core plasma. The simulation shows that only about 0.4% of the heating laser energy was coupled to densities above 100 g/cm^3.

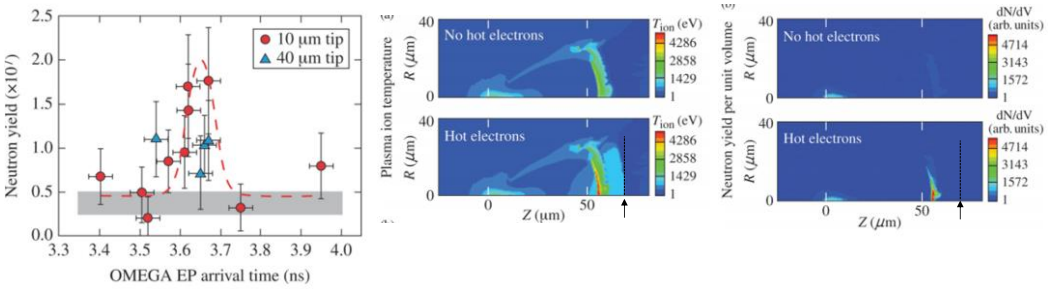

Figure 1.16 Observed neutron yields enhancement as a function of injection timing of the heating laser (left). Ion temperature distribution with or without REB from the integrated simulation (middle). Neutron yields per unit volume with or without REB from the integrated simulation (right). Images taken from Theobald *et. al.*, [22]

1.6.2 High-energy X-ray measurement using cone-in-shell attached cubic block target [23]

The energy coupling from laser to core plasma can be evaluated from absolute number and energy spectrum of high-energy X-ray converted from laser-produced REB.

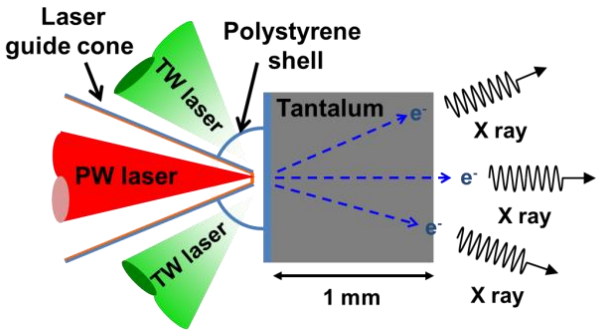

Figure 1.17 Illustration of a cone-in-shell attached the cubic block target. The generated electron beams with the energy less than 1 MeV is converted into the X-ray in the block.

The energy coupling from laser to core plasma η_{heat} can be expressed as follows,

$$\eta_{heat} = \frac{\Delta E_{core}}{E_L} = \eta_{REB} \cdot \eta_{col} \cdot \eta_{dep} = \frac{E_{REB}}{E_L} \cdot \frac{\pi r_{core}^2}{\pi r_{REB}^2} \cdot \frac{2\rho_{core} r_{core}}{R_{REB}} \qquad (1\text{-}22)$$

$$= \frac{E_{REB}}{E_L} \cdot \frac{\pi r_{core}^2}{\pi r_{REB}^2} \cdot \frac{2\rho_{core} r_{core}}{0.6 T_{REB}}$$

The laser-to-core coupling can be expressed with the probability of collision between the REB and the fuel core, and the fraction of energy deposited in the fuel core from the REB. η_{REB} is conversion efficiency from laser to electron, which is determined by the ratio of the total kinetic energy E_{REB} and the total laser energy E_L. η_{col} is the ratio between the geometrical cross-section of the fusion fuel core (πr^2_{core}). the REB (πr^2_{REB}) at the core position. η_{dep} is approximated as the ratio between the areal density of the fusion fuel core ($2\rho_{core} r_{core}$) and the average range of the REB in the compressed core (R_{REB}).

The propagated REB through the cone tip and the coronal plasma collides the metal block instead of a dense plasma core, REB is immediately converted into the bremsstrahlung X-ray. By comparing the results of Monte-Carlo simulation assuming the initial number and energy distribution of REB and the measured bremsstrahlung X-ray, the absolute number and energy distribution of REB can be estimated. The evaluated laser-to-core coupling was only 0.37 +/- 0.23 % [23].

1.6.3 K-shell radiation yields and spatial distribution measurement [24,25]

Neutron yields measurement requires accurate initial estimation of the deposited energy. However, this approach has the systematic uncertainty due to inferring a size and density of the energy deposition region.

Dopant target enable us to visualize the spatial distribution of REB and to estimate the total energy deposition from REB to a dense plasma core. Details techniques are described in Section 3 and 5, respectively. Figure 1.18 shows a photograph of Cu doped cone-in-shell target and the total Cu-Kα yields as a function of heating laser energy. The total deposition energy by REB can be estimated from the measured absolute Kα yields.

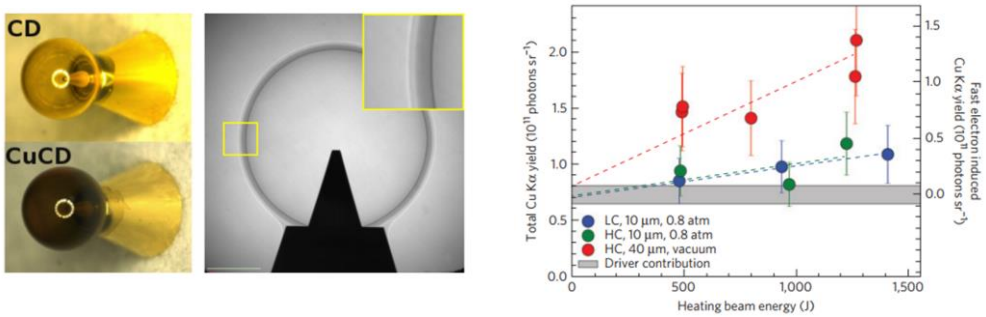

Figure 1.18 Photographs of Cu doped cone-in-shell target (left). Total Cu-Kα yields as a function of heating laser energy (right). Image taken from Jarrot *et el*., [25]

7 % of the coupling efficiency from laser to core with a large areal density (~0.3 g / cm^2) was reported by Jarrott *et. al.,*[24]. In this paper, they have concluded that such a low-energy coupling efficiency results from three combined factors. First, the large distance from the REB source to the core plasma due to pre-formed plasma created by amplified spontaneous emission (ASE) components of laser. Second, relatively low areal density core plasma cannot stop the REB efficiently. Third, a large angular divergence of REB due to beam-plasma instability reduces the collisional cross-section area for core plasma. Details will be described in section 4.

1.7 Alternative approach to electron-based FI scheme

1.5.1 Proton FI scheme [26, 27]

Proton fast ignition scheme was proposed as an alternative approach to electron-based FI

scheme. Proton beams generated by the process of target normal sheath acceleration (TNSA) [27] is used to create a hot spot instead of the REB. The proton beams enables to create a localized hot spot than the electron beams because of localized energy deposition due to their Bragg peak. A schematic view of a proton FI concept is described in Figure 1.19. The ultra-intense laser pulse is irradiated at the outer surface of the curved foil. When the accelerated electron beams reaches at the inner surface of the curved foil, resulting in the formation of an intense electric field at the target normal direction that accelerates proton beams attached the surface of the foil. The accelerated proton beams is converged into the imploded core plasma and deposits their kinetic energy.

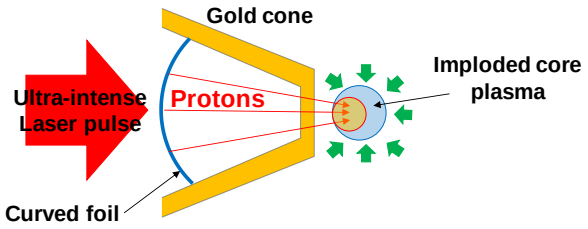

Figure 1.19 Illustration of a concept of proton fast ignition.

1.5.2 Shock ignition scheme [28]

Shock ignition scheme was introduced by Betti *et al*,. First, the DT capsule is symmetrically compressed at low velocity. The first main shock converges towards the center. At the maximum compression time, a high intensity spike laser pulse (~ 10^{16} W/cm^2) is sent to the surface of the compressed target through the same path of the first laser pulse. This spike pulse drives a strong shock that is amplified by collision with rebound shock, leading to increase of the hot spot pressure.

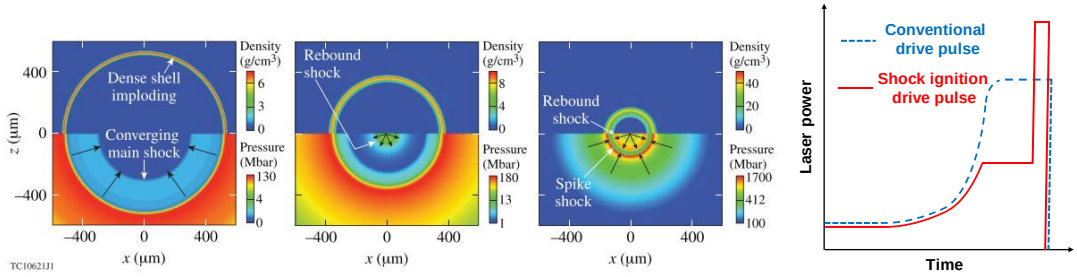

Figure 1.20 Illustration of the shock dynamics in shock ignition (left). Typical pulse shape for shock ignition experiment and conventional ICF experiment (right).
Images taken from Craxton *et al.,* [10]

1.5.3 Impact ignition scheme [29]

Impact ignition was proposed by Murakami & Nagatomo [29], in which the compressed DT fuel is ignited by a thin fragment of a spherical shell, called impactor, made of DT layer coated with a low Z ablator. A illustration of the impact ignition scheme is showon in Figure 1.21.

First, the DT fuel is asymmetrically compressed at a low speed by ns time scale laser or X-ray radiations. At the maximum compression, the a ns laser with intensity ~ 10^{15} W/cm^2 is focused on the impactor, which is accelerated in the hollow conical cone to very high speed in the order of 10^8 cm/s. Its kinetic energy is directly converted into thermal energy corresponding to > 5 keV, which leads to ignition. The first experiment of impact ignition was demonstrated by Azechi *et al*,.[30] The impactor was accelerated to ~6×10^6 cm/s and its kinetic energy was efficiently converted into thermal energy generating a temperature of ~1.6 keV. 100-fold DD fusion neutron enhancement was observed compared to the case of only implosion.

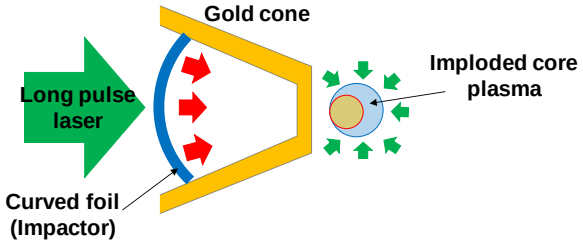

Figure 1.21 Illustration of a concept of impact ignition.

1.8 Summary of this section

A high power can create HED plasma states

1.9 Goal and contents of the thesis

The goal of this thesis is to demonstrate an efficient heating of a dense plasma with assistance of external magnetic fields for realization of high-energy-density state. In this study, we have successfully demonstrated the efficient energy deposition from laser to dense core plasma by

‘Magnetized ’fast isochoric laser heating scheme. Our results are fairly good agreement with the simple evaluation model. This model also reveals that an ignition scale plasma leads to much higher energy coupling than obtained with current ICF scheme.

The thesis is structured as follows:

Section 2 provides theoretical aspects of plasma produced by laser – plasma interaction. The understanding of the process of laser-produced electron beams is are required for realization of the efficient energy coupling from laser to core plasma in FI experiment.

Section 3 introduces diagnostics for characterization of electron beam transport. In particular, X-ray imaging and spectroscopy enables us to estimate the spatial energy deposition and the energy coupling from laser to core plasma.

Section 4 summarizes current statue of electron-base FI experiment. Three critical problems have been recognized as obstacles to the efficient fast heating. Approaches to overcome critical problems are described in this section.

Section 5 describes demonstration of the efficient energy deposition from laser to dense core plasma by ‘Magnetized ’fast isochoric laser heating scheme.

Section 6 summarizes obtained experimental results and perspective of this scheme for ignition scale condition.

References in **Section1**

[1] B. Remington, R. Drake, & D. Ryutov *Experimental astrophysics with high power lasers and Z pinches.* Rev. Mod. Phys. **78**, 755–807 (2006).

[2] S. Fujioka, H. Takabe, N. Yamamoto, D. Salzmann, F. Wang, H. Nishimura, Y. Li, Q. Dong, S. Wang, Y. Zhang, Y.-J. Rhee, Y.-W. Lee, J.-M. Han, M. Tanabe, T. Fujiwara, Y. Nakabayashi, G. Zhao, J. Zhang and K. Mima *X-ray astronomy in the laboratory with a miniature compact object produced by laser-driven implosion.* Nat. Phys. **5**, 821–825 (2009).

[3] S. Ohno, T. Kadono, K. Kurosawa, T. Hamura, T. Sakaiya, K. Shigemori, Y. Hironaka, T. Sano, T. Watari, K. Otani,T. Matsui and S. Sugita *Production of sulphate-rich vapour during the Chicxulub impact and implications for ocean acidification.* Nat. Geosci. **7**, 1–4 (2014).

[4] R. F. Smith, J. H. Eggert, R. Jeanloz, T. S. Duffy, D. G. Braun, J. R. Patterson, R. E. Rudd, J. Biener, A. E. Lazicki, A. V. Hamza, J. Wang, T. Braun, L. X. Benedict, P. M. Celliers & G. W.

Collins Ramp compression of diamond to five terapascals. Nature **511**, 330–333 (2014).

[5] D. T. Casey, D. B. Sayre, C. R. Brune, V. A. Smalyuk, C. R. Weber, R. E. Tipton, J. E. Pino, G. P. Grim, B. A. Remington, D. Dearborn, L. R. Benedetti, J. A. Frenje, M. Gatu-Johnson, R. Hatarik, N. Izumi, J. M. McNaney, T. Ma, G. A. Kyrala, S. MacLaren, J. Salmonson, S. F. Khan, A. Pak, L. Berzak Hopkins, S. LePape, B. K. Spears, N. B. Meezan, L. Divol, C. B. Yeamans, J. A. Caggiano, D. P. McNabb, D. M. Holunga, M. Chiarappa-Zucca, T. R. Kohut and T. G. Parham *Thermonuclear reactions probed at stellar-core conditions with laser-based inertial-confinement fusion.* Nat. Phys. **13**, 1227-1231 (2017).

[6] A. Zylstra, H. W. Herrmann, M. Gatu Johnson, Y. H. Kim, J. A. Frenje, G. Hale, C. K. Li, M. Rubery, M. Paris, A. Bacher, C. R. Brune, C. Forrest, V. Yu. Glebov, R. Janezic, D. McNabb, A. Nikroo, J. Pino, T. C. Sangster, F. H. Séguin, W. Seka, H. Sio, C. Stoeckl, and R. D. Petrasso *Using Inertial Fusion Implosions to Measure the T + ^{3}He Fusion Cross Section at Nucleosynthesis-Relevant Energies.* Phys. Rev. Lett. **117**, 035002 (2016).

[7] J. Nuckolls, L. Wood, A. Thiessen & G. Zimmerman *Laser Compression of Matter to Super High Densities: Thermonuclear (CTR) Applications.* Nature **239**, 139–142 (1972).

[8] S. Atzeni & J. Meyer-Ter-Vehn *The Physics of Inertial Fusion.* Oxford Science Publications (2004).

[9] H. Azechi, *J. Plasma Fusion Res.* **81**, Suppl. p.2-10 (2005). (in Japanese)

[10] R. S. Craxton, K. S. Anderson, T. R. Boehly, V. N. Goncharov, D. R. Harding, J. P. Knauer, R. L. McCrory, P. W. McKenty, D. D. Meyerhofer, J. F. Myatt, A. J. Schmitt, J. D. Sethian, R. W. Short, S. Skupsky, W. Theobald, W. L. Kruer, K. Tanaka, R. Betti, T. J. B. Collins, J. A. Delettrez, S. X. Hu, J. A. Marozas, A. V. Maximov, D. T. Michel, P. B. Radha, S. P. Regan, T. C. Sangster, W. Seka, A. A. Solodov, J. M. Soures, C. Stoeckl, and J. D. Zuegel *Direct-drive inertial confinement fusion* : *A review*. Phys. Plasmas **22** (2015).

[11] R. Betti, & O. A. Hurricane I*nertial-confinement fusion with lasers*. Nat. Phys. **12**, 435–448 (2016).

[12] Lindl, J., Landen, O., Edwards, J. & Moses, E. *Review of the National Ignition Campaign 2009-2012.* Phys. Plasmas **21**, 020501 (2014).

[13] O. A. Hurricane, D. A. Callahan, D. T. Casey, P. M. Celliers, C. Cerjan, E. L. Dewald, T. R. Dittrich, T. Do¨ppner, D. E. Hinkel, L. F. Berzak Hopkins, J. L. Kline, S. Le Pape, T. Ma, A. G. MacPhee, J. L. Milovich, A. Pak, H.-S. Park, P. K. Patel, B. A. Remington, J. D. Salmonson, P. T. Springer & R. Tommasini *Fuel gain exceeding unity in an inertially confined fusion implosion.* Nature **506**, 343–348 (2014).

[14] O. A. Hurricane, D. A. Callahan, D. T. Casey, E. L. Dewald, T. R. Dittrich, T. Döppner, S. Haan, D. E. Hinkel, L. F. Berzak Hopkins, O. Jones, A. L. Kritcher, S. Le Pape, T. Ma, A. G. MacPhee, J. L. Milovich, J. Moody, A. Pak, H.-S. Park, P. K. Patel, J. E. Ralph, H. F. Robey,

J. S. Ross, J. D. Salmonson, B. K. Spears, P. T. Springer, R. Tommasin, F. Albert, L. R. Benedetti, R. Bionta, E. Bond, D. K. Bradley, J. Caggiano, P. M. Celliers, C. Cerjan, J. A. Church, R. Dylla-Spears ,D. Edgell, M. J. Edwards, D. Fittinghoff, M. A. Barrios Garcia, A. Hamza, R. Hatarik, H. Herrmann, M. Hohenberger, D. Hoover, J. L. Kline, G. Kyrala, B. Kozioziemski, G. Grim, J. E. Field, J. Frenje, N. Izumi, M. Gatu Johnson, S. F. Khan, J. Knauer, T. Kohut, O. Landen, F. Merrill, P. Michel, A. Moore, S. R. Nagel, A. Nikroo, T. Parham, R. R. Rygg, D. Sayre, M. Schneider, D. Shaughnessy, D. Strozzi, R. P. J. Town, D. Turnbull, P. Volegov, A. Wan, K. Widmann, C. Wilde and C. Yeamans *Inertially confined fusion plasmas dominated by alpha-particle self-heating.* Nat. Phys. **12**, 800–806 (2016).

[15] M. Tabak, J. Hammer, M. E. Glinsky, W. L. Kruer, S. C. Wilks, J. Woodworth. E. M. Campbell and M. D. Perry I*gnition and high gain with ultrapowerful lasers*. Phys. Plasmas **1**, 1626 (1994).

[16] S. Wilks, W. Kruer, M. Tabak & A. Langdon *Absorption of ultra-intense laser pulses.* Phys. Rev. Lett. **69**, 1383–1386 (1992).

[18] S. E. Coe, T. Afshar-rad, and O. Willi, *Direct observations of filamentation and self-focusing in a large underdense plasma.* Opt. Commun. **73**, 299 (1989).

[19] S. E. Coe, T. Afshar-rad, and O. Willi, *Experimental observations of thermal whole beam self-focusing*. Europhys. Lett. **13**, 251 (1990).

[20] R. Kodama, P. A. Norreys, K. Mima, A. E. Dangor, R. G. Evans, H. Fujita, Y. Kitagawa, K. Krushelnick, T. Miyakoshi, N. Miyanaga, T. Norimatsu, S. J. Rose, T. Shozaki, K. Shigemori, A. Sunahara, M. Tampo, K. A. Tanaka, Y. Toyama, T. Yamanaka & M. Zepf *Fast heating of ultrahigh-density plasma as a step towards laser fusion ignition.* Nature **412**, 798–802 (2001).

[21] R. Kodama, H. Shiraga, K. Shigemori, Y. Toyama, S. Fujioka, H. Azechi, H. Fujita, H. Habara, T. Hall, Y. Izawa, T. Jitsuno, Y. Kitagawa, K. M. Krushelnick, K. L. Lancaster, K. Mima, K. Nagai, M. Nakai, H. Nishimura, T. Norimatsu, P. A. Norreys, S. Sakabe, K. A. Tanaka, A. Youssef, M.Zepf, T. Yamanaka *Nuclear fusion: Fast heating scalable to laser fusion ignition.* Nature **418**, 933–934 (2002).

[22] W. Theobald, A. A. Solodov, C. Stoeckl, K. S. Anderson, R. Betti, T. R. Boehly, R. S. Craxton, J. A. Delettrez, C. Dorrer, J. A. Frenje, V. Yu. Glebov, H. Habara, K. A. Tanaka, J. P. Knauer, R. Lauck, F. J. Marshall, K. L. Marshall, D. D. Meyerhofer, P. M. Nilson, P. K. Patel, H. Chen, T. C. Sangster, W. Seka, N. Sinenian, T. Ma, F. N. Beg, E. Giraldez, and R. B. Stephens *Initial cone-in-shell fast-ignition experiments on OMEGA.* Phys. Plasmas **18**, 056305 (2011).

[23] S. Fujioka, T. Johzaki, Y. Arikawa, Z. Zhang, A. Morace, T. Ikenouchi, T. Ozaki, T. Nagai, Y. Abe, S. Kojima, **S. Sakata**, H. Inoue, M. Utsugi, S. Hattori, T. Hosoda, S. H. Lee, K. Shigemori, Y. Hironaka, A. Sunahara, H. Sakagami, K. Mima, Y. Fujimoto, K. Yamanoi, T.

Norimatsu, S. Tokita,Y. Nakata, J. Kawanaka, T. Jitsuno, N. Miyanaga, M. Nakai, H. Nishimura, H. Shiraga, H. Nagatomo, and H. Azechi, Heating *Efficiency Evaluation with Mimicking Plasma Conditions of Integrated Fast-Ignition Experiment* Phys. Rev. E **91**, 063102 (2015).

[24] L. C. Jarrott, M. S. Wei, C. McGuffey, A. A. Solodov, W. Theobald, B. Qiao, C. Stoeckl, R. Betti, H. Chen, J. Delettrez, T. Döppner, E. M. Giraldez, V. Y. Glebov, H. Habara, T. Iwawaki, M. H. Key, R. W. Luo, F. J. Marshall, H. S. McLean, C. Mileham, P. K. Patel, J. J. Santos, H. Sawada, R. B. Stephens, T. Yabuuchi and F. N. Beg *Visualizing fast electron energy transport into laser-compressed highdensity fast-ignition targets*. Nat. Phys. **12,** 499–504 (2016).

[25] L. C. Jarrott, C. McGuffey, F. N. Beg, A. A. Solodov, W. Theobald, B. Qiao, C. Stoeckl, R. Betti, H. Chen, J. Delettrez, T. Doppner, E. M. Giraldez, V. Y. Glebov, H. Habara, T. Iwawaki, M. H. Key, R. W. Luo, F. J. Marshall, H. S. McLean, C. Mileham, P. K. Patel, J. J. Santos, H. Sawada, R. B. Stephens, T. Yabuuchi and M. S. Wei *Transport and spatial energy deposition of relativistic electrons in copper-doped fast ignition plasmas.* Phys. Plasmas **24**, 102710 (2017).

[26] M. Roth T. E. Cowan, M. H. Key, S. P. Hatchett, C. Brown, W. Fountain, J. Johnson, D. M. Pennington, R. A. Snavely, S. C. Wilks, K. Yasuike, H. Ruhl, F. Pegoraro, S. V. Bulanov, E. M. Campbell, M. D. Perry, and H. Powell1 *Fast Ignition by Intense Laser-Accelerated Proton Beams.* Phys. Rev. Lett. **86**, 436 (2001).

[27] M. H. Key *Status of and prospects for the fast ignition inertial fusion concept.* Phys. Plasmas **14**, 055502 (2007).

[28]

[29] M. Murakami & H. Nagatomo *A new twist for inertial fusion energy : Impact ignition.* Nucl. Instrum. and meth. in Phys. Res. A **544**, 67-75 (2005).

[30] H. Azechi T. Sakaiya, T. Watari, M. Karasik, H. Saito, K. Ohtani, K. Takeda, H. Hosoda, H. Shiraga, M. Nakai, K. Shigemori, S. Fujioka, M. Murakami, H. Nagatomo, T. Johzaki, J. Gardner, D. G. Colombant, J. W. Bates, A. L. Velikovich, Y. Aglitskiy, J. Weaver, S. Obenschain, S. Eliezer, R. Kodama, T. Norimatsu, H. Fujita, K. Mima, and H. Kan *Experimental Evidence of Impact Ignition: 100-Fold Increase of Neutron Yield by Impactor Collision.* Phys. Rev. Lett. **102**, 235002 (2009).

2. Laser absorption mechanism

When the intense laser pulse interacts with the matter, the laser pulse is absorbed through some processes, which produces the energetic (relativistic) particle beams and self-generated electro-magnetic fields. The accelerated particles propagates through a large variety of plasmas accompanied with self-generated fields. The understanding of process of generation at the below critical density plasma and propagation of such particles in the dense plasma, in particular electrons, are required for realization of the efficient energy coupling from laser to core plasma in FI experiment. This section briefly summarizes the ionization in the strong laser electric field and laser absorption process as main topics.

2.1 General properties of plasma

2.1.1 Landau length

The Landau length is defined as the minimum approach distance between two electrons in the plasma. The average Landau length r_0 is described by solving Equation 2-1,

$$\frac{1}{2}m_e v_e^2 = k_B T_e = \frac{e^2}{4\pi\varepsilon_0 r_0} \tag{2-1}$$

$$r_0 = \frac{e^2}{4\pi\varepsilon_0 k_B T_e} \tag{2-2}$$

2.2.2 Debye length

The range of Coulomb interaction is suppressed due to the screening effect. The plasma system is neutral, i.e. one can look at the ions as a neutralizing background for the plasma electrons having a temperature T_e. The equation of motion of the electron fluid in this case is given by

$$f_e + f_{pe} = 0 \;\Rightarrow\; -n_e e\nabla\Phi(r) - k_B T_e \nabla n_e = 0 \;\Rightarrow\; \frac{1}{n_e}\frac{dn_e}{dr} = -\frac{e}{k_B T_e}\frac{d\Phi}{dr} \tag{2-3}$$

This equation can be integrated, giving the Boltzmann distribution of electrons in the electrostatic potential:

$$n_e(r) = n_{e,0}\exp\left(-\frac{e\Phi(r)}{k_B T_e}\right) \simeq n_{e,0}\left(1 - \frac{e\Phi(r)}{k_B T_e}\right) \tag{2-4}$$

The ion potential Φ can be evaluated by using the Maxwell-Poisson equation:

$$\nabla E = -\Delta\Phi = \frac{\rho}{\epsilon_0} = \frac{-en_e + q_i n_{e,0}}{\epsilon_0} = -\frac{n_e - n_{e,0}}{\epsilon_0} e \tag{2-5}$$

Substituting equation 2-4 into equation 2-5 and the solution of equation 2-6 is

$$\Delta\Phi = \frac{n_e e^2}{\epsilon_0 k_B T_e}\Phi \quad \Rightarrow \quad \Phi = \frac{q_i}{4\pi\epsilon_0 r}\exp\left(-\frac{r}{\lambda_D}\right) \tag{2-6}$$

Here $\lambda_D = \sqrt{\epsilon_0 k_B T_e / n_e e^2}$ is Debye length

The number of electrons in the Debye sphere is given by

$$N_D = \frac{4}{3}\pi n_e \lambda_D^3 \tag{2-7}$$

2.2.3 Coulomb logarithm

The Coulomb logarithm is defined as the ratio between maximum and minimum impact parameter. The maximum impact parameter $b_{\max}$ is equal to the Debye length. The minimum impact parameter $b_{\min}$ is chosen as Landau length. The impact parameter is defined as

The Coulomb logarithm can be expressed as

$$\ln\Lambda = \ln\left(\frac{b_{\max}}{b_{\min}}\right) = \max\left[\ln\left(\frac{\lambda_D}{\max(r_{ei})}\right), 2\right] \tag{2-8}$$

2.2 Ionization

2.2.1 Ionization threshold

Bohr radius is written as

$$a_B = \frac{\hbar^2}{me^2} = 5.3 \times 10^{-9} \quad \text{cm} \tag{2-9}$$

The electric field strength is

$$E_a = \frac{e}{a_B^2} \simeq 5.1 \times 10^9 \quad \text{V/m} \tag{2-10}$$

The laser intensity I_a which equal to the binding strength of the electron to atom is

$$I_a = \frac{cE_a^2}{8\pi} \simeq 3.51 \times 10^{16} \quad \text{W/cm}^2 \tag{2-11}$$

If the laser intensity is larger than I_a, any target material will be ionized.

2.2.2 Ionization of atom in the laser field

Above threshold ionization (ATI)

The electron absorbs more energy than consistent with the minimum number n of photons. The final kinetic energy is given by an extended Einstein's formula,

$$E_f = (n+s)\hbar\omega - E_{ion} \tag{2-12}$$

Where n is the number of photons required for multiphoton ionization, s is excess absorbed.

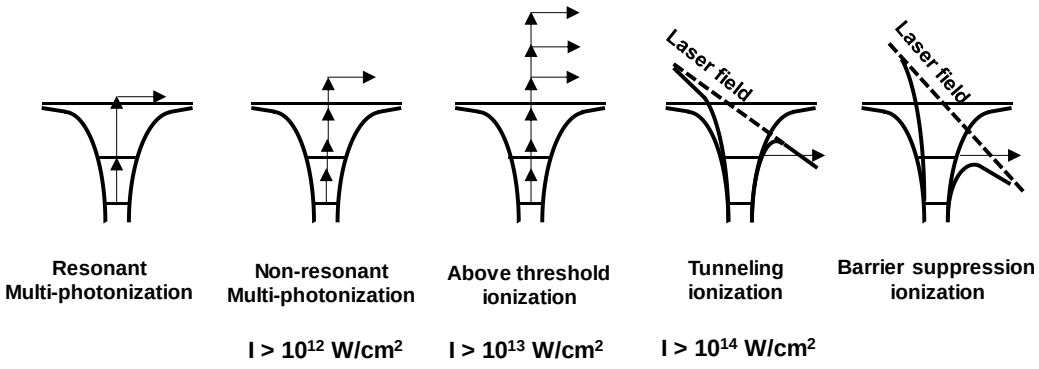

Figure 2.1 Schematic picture of multiphoton and tunneling ionization process.

Tunneling ionization

$$\gamma = \omega_L \sqrt{\frac{2E_{ion}}{I_L}} \sim \sqrt{\frac{E_{ion}}{\Phi_{pond}}} \tag{2-13}$$

As a rule of thumb, tunneling appears for strong fields and long wavelengths, for < 1 ; multiphoton ionization for $\gamma > 1$.

Barrier suppression

If the barrier is lower than the ion electric static potential, the electron can escape spontaneously. This process is known as barrier suppression ionization (BSI).

$$x_{max} = (Ze/\varepsilon) \tag{2-14}$$

The threshold field strength at which BSI occurs is

$$\varepsilon_c = \frac{E_{ion}^2}{4Ze^3} \tag{2-15}$$

Equating this critical field to the peak electric field of the laser yields an effective appearance intensity for ion created with charge Z:

$$I_{app} = \frac{c}{8\pi}\varepsilon_c^2 = \frac{cE_{ion}^4}{128\pi Z^2 e^6} \tag{2-16}$$

2.3 Linear absorption mechanism

2.3.1 Collisional absorption

Collisional absorption becomes dominant at intensities $I\lambda^2 \leq 10^{15}\mathrm{W}/cm^{-2}\mu m^2$. In this process, the electrons in the laser electric field increases their kinetic energy during a collision with an ion. Then the oscillated electrons by the laser electric field losses their energy to the background ions in the plasma via collisions.

The equation of motion of the electron in an electromagnetic wave including the collision term is given by

$$m_e \frac{d\boldsymbol{v}}{dt} = -eE - m\nu_{ei}\boldsymbol{v} \tag{2-17}$$

here v is the electron oscillatory velocity and ν_{ei} is the electron-ion collision frequency. Solving above equation gives

$$v = \frac{eE}{m_e\omega}\left(\frac{i - \nu_{ei}/\omega}{1 + (\nu_{ei}/\omega)^2}\right) \tag{2-18}$$

The current $\boldsymbol{J} = -n_e e v$ is given by

$$J = \frac{ne^2 E}{m_e \omega}\left(\frac{i - \nu_{ei}/\omega}{1 + (\nu_{ei}/\omega)^2}\right) \tag{2-19}$$

The absorption coefficient is

$$k_{\mathrm{ca}} = 3.1 \times 10^{-7} Z n_e^2 ln\Lambda T_e^{-3/2} \omega^{-2}\left(1 - \frac{\omega_p^2}{\omega^2}\right)^{1/2} \tag{2-20}$$

Figure 2.2 shows the laser absorption rate as a function of laser intensity for various wavelength. The absorption rate is higher than the shorter wavelength case. This is due to higher collision frequency for shorter wavelength case.

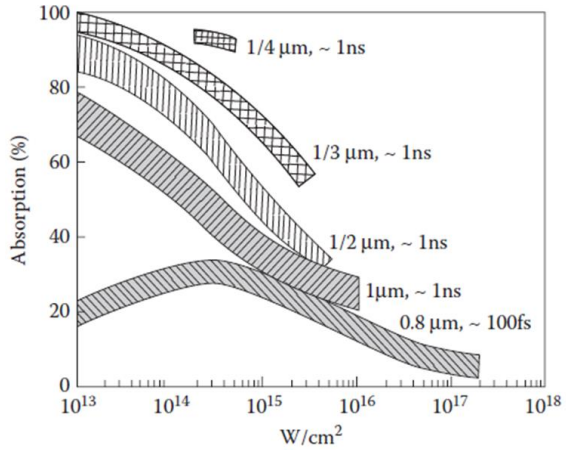

Figure 2.2 Laser absorption rate as a function of laser intensity for various wavelength. Image taken from Eliezer

2.3.3 Resonance absorption

When a linear polarized laser light is incident obliquely into a plasma with density gradient in the direction of incidence, the plasma wave is resonantly excited at the critical surface. This process is called resonant absorption. The energy is transferred to the plasma through collisional or collisionless damping of the plasma wave. When an electromagnetic wave (p polarized light) is incident into the plasma with density gradient in the direction of incidence at an angle θ, the component for electric field perpendicular to the surface at the turning point appears. This electric field oscillates the electrons across the non-uniform density region, which causes a large amplitude electron-plasma wave in the direction perpendicular to the surface. Geometry for

resonance absorption is shown in Figure 2.2.

For s polarized light, critical density can be described as

$$n_e(\theta) = n_{cr}\cos^2\theta \tag{2-21}$$

On the other hand, the electric field can tunnel through the plasma and couple energy to (Langmuir waves). The incident angle for resonant absorption is determined by following parameters,

$$\sin\theta = \left(\frac{c}{\omega_L L}\right)^{1/3} \tag{2-22}$$

Where ω_L is laser frequency and L is plasma scale length.

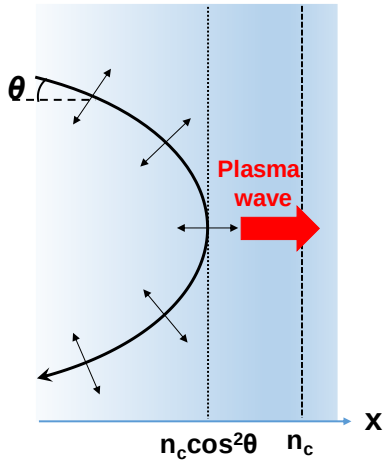

Figure 2.3 Geometry for resonance absorption. The double arrow show the vibration direction of laser electric field.

2.4 Non-linear absorption mechanism

2.4.1 Ponderomotive force

The ponderomotive force arises from the time-average of the magnetic-field term in the Lorentz force. The time-average force is nonzero when there is a gradient in the electromagnetic field along the direction of propagation. Let us consider a linear polarized laser with an electric field $\boldsymbol{E} = \boldsymbol{E_0}(\boldsymbol{r}, t)\cos(\omega_L t)$ and a magnetic field **B**(**r**, t), the equation of motion of the single electron is

described as follows:

$$m_e \frac{d\boldsymbol{v}}{dt} = -e\left(\boldsymbol{E}(\boldsymbol{r},t) + \frac{\boldsymbol{v}}{c} \times \boldsymbol{B}(\boldsymbol{r},t)\right) \tag{2-23}$$

The first order electron velocity $\boldsymbol{v}_1$ and the trajectory $\boldsymbol{r}_1$ are

$$\boldsymbol{v}_1 = -\frac{e}{m_e \omega_L} \boldsymbol{E}(\boldsymbol{r_0},t) \tag{2-24}$$

$$\boldsymbol{r}_1 = \frac{e}{m_e \omega_L^2} \boldsymbol{E}(\boldsymbol{r_0},t) \tag{2-25}$$

Here considering the second order of the Equation 2-23, the equation of motion of the single electron can be written as

$$m_e \frac{d\boldsymbol{v}_2}{dt} = -e\left[(\boldsymbol{r}_1 \cdot \nabla)\boldsymbol{E}(\boldsymbol{r_0},t) + \frac{\boldsymbol{v_1}}{c} \times \boldsymbol{B}(\boldsymbol{r_0},t)\right] \tag{2-26}$$

Substituting the $\boldsymbol{r}_1$ into Equation 2-1, and by using Maxwell-Faraday's equation,

$$m_e \frac{d\boldsymbol{v}_2}{dt} = -\frac{e^2}{m_e \omega_L^2}\left[(\boldsymbol{E}_1 \cdot \nabla)\boldsymbol{E}_1 - \omega_L \boldsymbol{E}_1 \times \int (\nabla \times \boldsymbol{E}_1)dt\right] \tag{2-27}$$

Taking the average of Equation 2-27 over a single laser period,

$$\langle m_e \frac{d\boldsymbol{v}_2}{dt}\rangle = -\frac{e^2}{m_e \omega_L^2}\langle(\boldsymbol{E}_1 \cdot \nabla)\boldsymbol{E}_1 + \boldsymbol{E}_1 \times \nabla \times \boldsymbol{E}_1\rangle \tag{2-28}$$

Using the following vectorial identity

$\nabla(AB) = (A \cdot \nabla)B + (B \cdot \nabla)A + A \times \nabla \times B + B \times \nabla \times A$

Equation 2-28 can be expressed using above formula as below,

$$\langle m_e \frac{d\boldsymbol{v}_2}{dt}\rangle = -\frac{1}{4}\frac{e^2}{m_e \omega_L^2}\nabla\langle \boldsymbol{E}_1^2\rangle = -\frac{1}{4}\frac{e^2}{m_e \omega_L^2}\langle\left[\left(\nabla\left|\boldsymbol{E}_0^2\right|\right) + \nabla\left|\boldsymbol{E}_0^2\right|\cos(2\omega_L t)\right]\rangle \tag{2-29}$$

The slowly variable term of equation 2-29 compared to the laser frequency is called pondromotive force,

$$\langle \boldsymbol{F}_p\rangle = -\frac{1}{4}\frac{e^2}{m_e \omega_L^2}\nabla\left|\boldsymbol{E}_0^2\right| \tag{2-30}$$

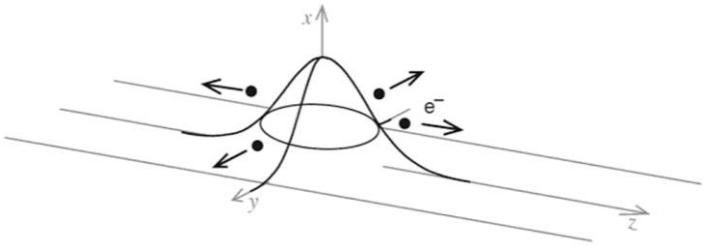

Figure 2.4 Schematic view of ponderomotive force $\boldsymbol{F}_{\mathrm{p}}$. Electrons are ejected from the center of the beam. $\boldsymbol{F}_{\mathrm{p}}$ of the laser pulse acts onto electrons along the intensity gradients of the envelope field.
Image taken from Schwoerer

2.4.2 Parametric instabilities

Figure 2.5 shows schematic view of the possible position creation for parametric instabilities at different electron density. The stimulated Raman scattering and the two plasmon decay occurs below the quarter of the critical density. The stimulated Brillouin scattering and the ion acoustic decay occurs below the critical density.

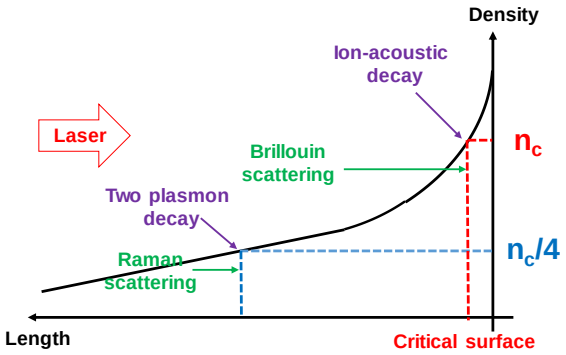

Figure 2.5 Schematic view of the possible position creation for the parametric instabilities.

・Stimulated Raman scattering (SRS) : The incident wave decays into an electron plasma wave and into a diffused electromagnetic wave ($\omega_{\mathrm{L}} = \omega_{pe} + \omega_{\mathrm{EM,diff}}$)

・Stimulated Brillouin scattering (SBS) : The incident wave decays into an ion acoustic wave and a diffused electromagnetic wave. ($\omega_{\mathrm{L}} = \omega_{ia} + \omega_{\mathrm{EM,diff}}$)

・Two plasmon decay : The incident wave decays into two electron plasma waves. ($\omega_{\mathrm{L}} = \omega_{\mathrm{pe}} + \omega'_{\mathrm{pe}}$)

・Ion acoustic decay : the incident waves decays into an electron plasma wave and into an ion acoustic wave. ($\omega_{\mathrm{L}} = \omega_{\mathrm{pe}} + \omega'_{\mathrm{pe}}$)

Figure 2.6 shows dispersion diagram for parametric three-wave process.

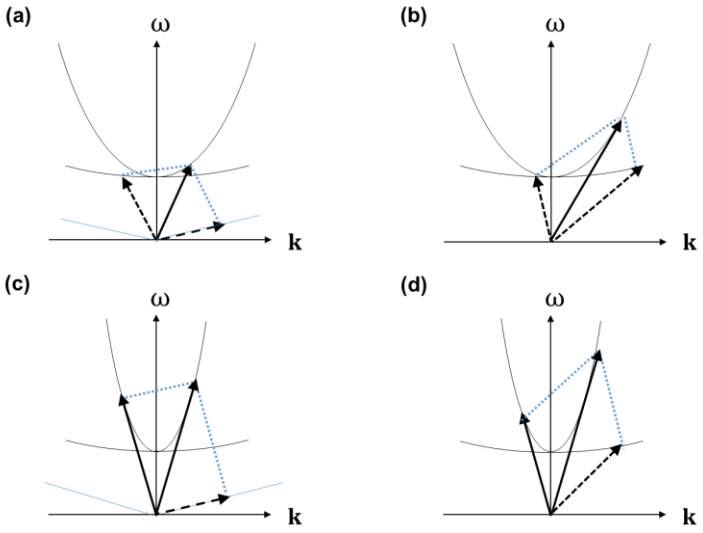

Figure 2.6 Dispersion diagram for parametric three-wave process. (a) parametric decay, (b) two-plasmon decay, (c) Brillouin scattering, (d) Ramman scattering.

3. Diagnostics for characterization of laser-accelerated electron beams

The energy coupling from laser to core plasma is the most important parameter in FI experiments. The laser-accelerated electron beams propagates through the core plasma and deposits their kinetic energy. A characterization of the energy and spatial distribution of REB are required to evaluate the laser-to-core energy coupling. In particular, the understanding of the process of the energy deposition by REB into the core plasma is a key issue for current FI experiments. This section provides that diagnostics for characterization of laser-accelerated electron beams as well as deposited energy into the dense core plasma.

3.1 Electron energy analyzer

Energy distribution of laser-accelerated electron beams is measured by magnet-based electron energy analyzer [1]. Figure 3.1 shows schematic view of a magnet-based electron energy analyzer.

Electrons are dispersed by the magnetic field according to their kinetic energies, whereby electrons with different kinetic energies are incident on the Image plate (IP: BAS-SR2025, Fuji Film) at different positions. The location of each electron is determined by a Larmor radius, which is dependent on the magnetic flux density and the electron kinetic energy.

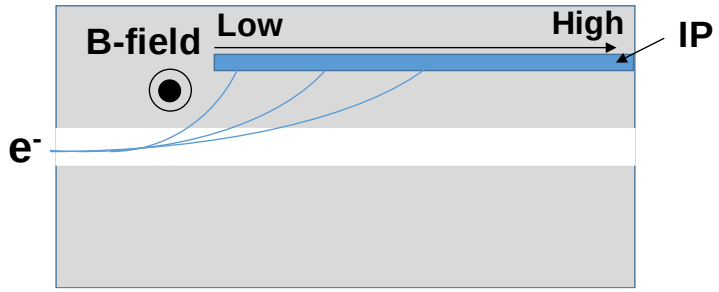

Figure 3.1 Schematic view of a magnet-based electron energy analyzer.

The electron kinetic energy at the position (l) of the IP is given by

$$\varepsilon(l) = m_e c \left[\sqrt{\left(\frac{l^2 + h^2}{2h} \right)^2 \left(\frac{eB}{m_e c} \right)^2 + 1} - 1 \right] \tag{3-1}$$

where ε is the electron kinetic energy, h is the height of the entrance slit from the IP surface, e is the elementary charge, B is the magnetic flux density, m_e is the mass of electron, and c is the speed

of light.

3.2 High-energy X-ray spectrometer for characterization of REB energy distribution

More quantitative absolute number and energy distribution of REB can be provided by bremsstrahlung X-ray spectroscopy without being affected by self-generated electrostatic and magnetic fields at the target surface compared to an electron energy analyzer.

3.2.1 Differential energy threshold (DET) X-ray spectrometer [2]

The REB with the energy from 1 to 3 MeV has the ideal stopping range for efficient energy deposition in the core plasma. The differential energy threshold (DFT) X-ray spectrometer which covers the energy range from 1 to 3 MeV was developed.

The spectrometer consists of 13 filters of increasing Z from Al to Pb. Pb with different sickness is used for differential filtering. The filters are covered with a 250 μm-thick plastic sheet on both sides to suppress the background signal due to secondary electrons with below 150 keV.

The electron spectra can be obtained from back-calculated a number of ways including fitting sample spectra.

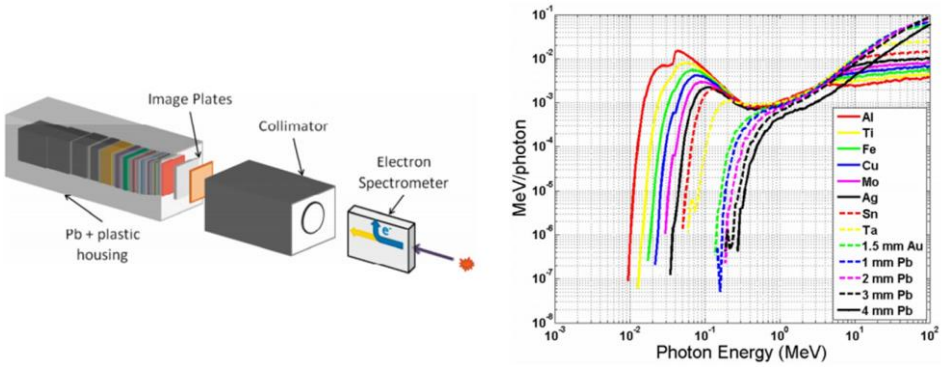

Figure 3.2 A schematic view of DFT spectrometer (left side). Calculated spectrometer channel response for each filters. Images taken from Chen [2].

3.2.2 Compton X-ray spectrometer [3]

A Compton X-ray spectrometer is proposed to obtain a higher energy resolution than the DET X-ray spectrometer.

Compton scattering effect becomes the dominant process in the energy range higher than 0.5 MeV. The total energy and momentum of a scattered X ray and a recoil electron are equivalent to the energy of an incident X ray and electron before scattering. According to the energy conservation law, measurement of the energy and scattered angle of the recoil electron enable us to estimate the energy of incident X ray. Equation 3-2 shows the relationship between the energies of an incident X ray ($h\nu$) and an recoiled electron (E_e) in the forward direction.

$$E_e = h\nu - \frac{h\nu}{1 + {2h\nu}/{0.511}} \tag{3-2}$$

Incident X-rays are converted to recoil electrons by Compton scattering in the X-ray electron converter. The absolute number and energy distribution of the scattered electrons is measured with a magnet-based electron-energy analyzer. By using the relationship shown in Figure 3-2, the energy of incident X-ray can be estimated directly from the measured energy of the recoil electron.

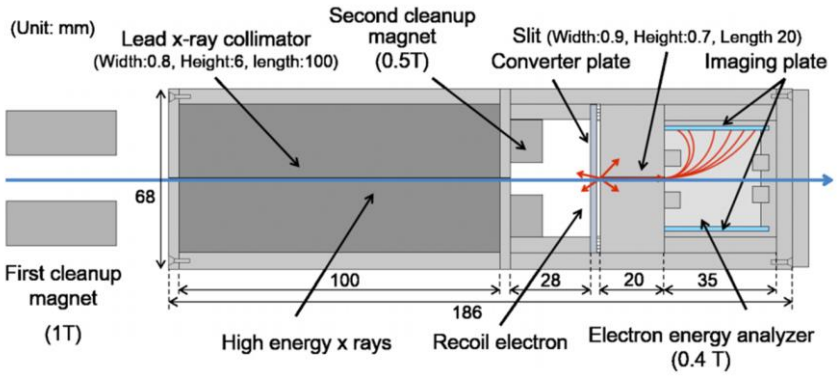

Figure 3.3 Schematic view of the Compton X-ray spectrometer.

3.2.3 Photonuclear reaction based high-energy X-ray spectrometer [4]

Although nuclear activation via photonuclear reaction was used in the previous studies, its accuracy in the energy range less than 10 MeV was insufficient for the FI research.

The number of neutrons generated via photonuclear reactions in an element is approximately proportional to the number of x-ray photons within the full width at half maximum (FWHM) of the element's cross-section. An x-ray spectrum ranging from 10 to 30 MeV can be obtained by comparing the numbers of neutrons that are generated in different elements.

The number of neutrons Nn generated by photonuclear reactions in a photon-neutron converter is calculated with the following equation:

$$N_n = \rho_A l \int_{S_\gamma}^{\infty} N_\gamma(h\nu)\sigma(h\nu)dh\nu \tag{3-3}$$

where ρ_A is the number density of the converter element, l is the thickness of the converter, Sγ is the photonuclear reaction threshold, N_γ (hν) is the x-ray fluence, and σ(hν) is the photonuclear cross-section. This formula can be approximated by using averaged values as

$$N_n = \rho_A l N_\gamma(\sigma) \tag{3-4}$$

where Nγ is integrated photon numbers within the FWHM of the cross-section of σ(hν). σ is a cross-section averaged on the FWHM. The generated neutron is detected by using bubble detector spectrometer (BDS). The number of bubble signals N_b can be calculated as follows:

$$N_b = N_n \eta_\Omega \varepsilon \tag{3-5}$$

here $\eta\Omega$ is the geometrical efficiency from the converter to the BDS, ε is the averaged detection efficiency of BDS. Finally, N_γ can be described as

$$N_\gamma = N_b / \rho_A l \langle\sigma\rangle \eta_\Omega \varepsilon \tag{3-6}$$

In addition, x-ray energies ranging from 2 to 10 MeV can be calculated from the energy spectrum of the neutrons that are generated in deuterium elements. The energy of neutrons (En) generated by the photodisintegration of deuterium atoms is written as $h\nu = 2E_n - E_b$, here $h\nu$ is an incident photon energy, and E_b is the binding energy of the photonuclear reaction,

respectively. The energy spectrum of the neutron can be measured by using BDS detectors (0.1, 0.6, 1, 2.5, and 10 MeV) with different energy thresholds.

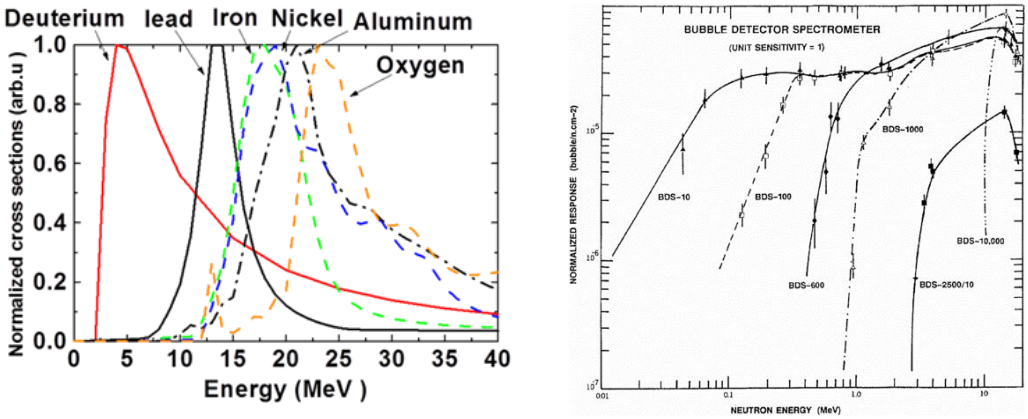

Figure 3.4 Peak normalized photo-nuclear cross-sections for various materials (left side). Sensitivity curve for various neutron energy (right side).

In our spectrometer design, neutrons are counted with a bubble detector (BDS series) [5] that is insensitive to x-rays. A bubble detector contains 10^4–10^5 superheated liquid droplets (with diameters of ~20 μm), which are dispersed uniformly over 8 cm^3 of a transparent polymer. When a neutron deposits sufficient energy (equal to or exceeding the threshold energy) to vaporize a droplet, the droplet becomes a visible bubble (with a diameter of ~1 mm). It is validated that no bubbles form for x-ray fluences less than 10^{10} photons/cm^2, which is equal to the fluence of the proof-of-principle experiment.

Dominant source of the background signal is neutron from the outside of the spectrometer, the background neutrons are generated by scattered x-rays in experimental apparatuses and room structure surrounding the spectrometer. A 20-cmthick paraffin block was placed in front of the spectrometer to absorb the neutrons from the outside of the spectrometer. Figure 2 shows a schematic of the spectrometer to measure 10–30 MeV x-rays. The 5-mm-thick cylindrical converters cover the bubble detectors that have the same threshold energy (0.6 MeV). The detectors were arranged concentrically.

Uncovered bubble detectors were also allocated to measure the background. The PHITS code,15 which is a Monte Carlo code for simulating interactions of a quantum with a matter, clarifies that the neutron counts caused by cross-talk between neighboring detectors are about 5% of the total counts. The other spectrometer was used to measure 2–10 MeV x-rays which are

not covered with the above spectrometer. The photon energy (2–10 MeV) of the incident x-rays is calculated from the energy of the photoneutron with the relation $h\nu = 2E_n - E_b$. The five bubble detectors, which have different threshold energies (0.1, 0.6, 1, 2.5, and 10 MeV), are placed in heavy or light water.

Contamination from oxygen atoms of water molecules can be removed by comparing neutrons from the light and heavy water. The quantum efficiency of this spectrometer was designed to be 10^{-7}, 10^{-4}, 10^{-5}, respectively, for 2–10, 11–15, and 15–25 MeV of photon energy ranges. Values of ρ_A, $\sigma(h\nu)$ at the peak energy, l, η of the x-ray spectrometer are summarized in Table I.

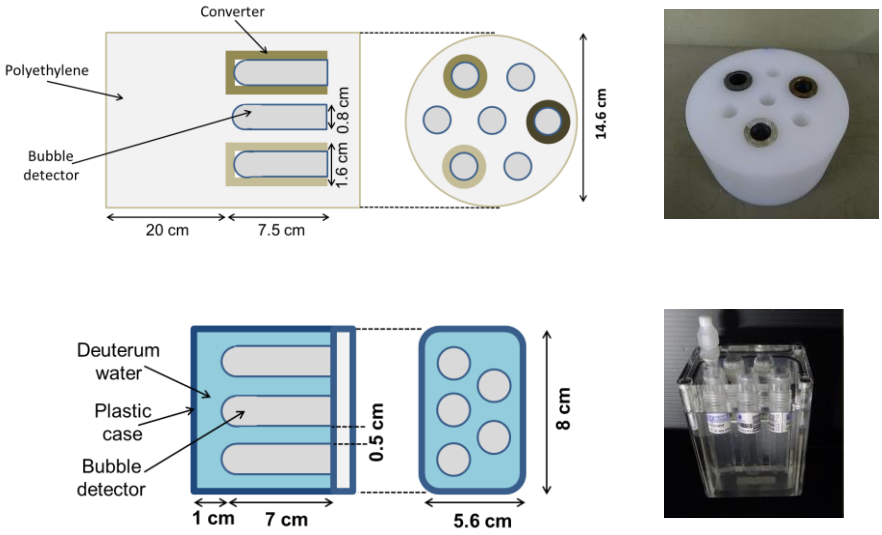

Figure 3.5 Schematic view of photonuclear reaction based X-ray spectrometers. Three metals (upper side), heavy water and light water (bottom side) are used as a converter.

TABLE I. Values of ρ_A, $\sigma(h\nu)$ at the peak energy, l, η_Ω of the x-ray spectrometer.

	$\rho_A(\times 10^{22})$ (cm^{-3})	σ (mb) at peak energy	l(cm), front/side	η_Ω
Deuterium	3.3	2.45	1.0/0.5	0.3
Lead	3.3	565	0.5/0.5	0.3
Iron	8.5	79.3	0.5/0.5	0.3
Aluminum	6.0	43.3	0.5/0.5	0.3

Table 3.1. Values of ρ_A, $\sigma(h\nu)$ at the peak energy, l, η of the x-ray spectrometer.

The proof-of-principle experiment was performed at ISIR. Bremsstrahlung x-rays were produced by irradiating a 5-mm-thick lead target with electrons, the energy and number of which are respectively 16 ± 0.32 MeV and 1.0×10^{-6} C. The x-ray detectors were set at distances of 135 cm and 150 cm from the lead target with angles of 30◦ from the normal to the target. The x-ray detectors used in this experiment were covered with light water, heavy water, lead, iron, and aluminum converters.

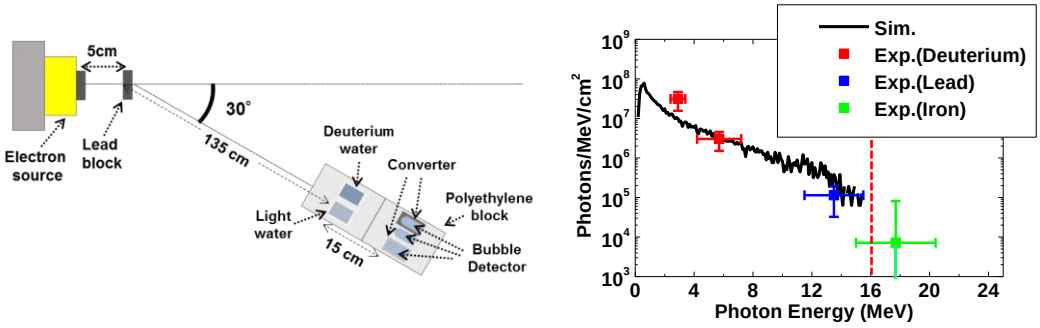

Figure 3.6 The proof-of-principle experimental setup (left side) and the measured X-ray spectrum.

3.3 Coherent transition radiation (CTR) [6]

Transition radiation (TR) occurs when a charged particle across the interface between two media with different dielectric constants. When the wavelength of emitted radiation is longer than the bunch length, the radiation becomes coherent. Coherent transition radiation (CTR) is directly related to the laser-accelerated ultrashort periodic bunches of relativistic electrons. Therefore, the spatial distribution of CTR enables us to provide the REB spatial distribution at the rear surface. The energy W emitted per unit angular frequency and solid angle in the forward direction in the case of a charged particle perpendicular to the interface separating a medium with relative dielectric constant ε_r to the vacuum is

$$\frac{d^2W}{d\omega d\Omega} = \frac{e^2}{\pi^2 c}\frac{\beta^2\sin^2\theta}{(1-\beta^2\cos^2\theta)^2} \times \left| \frac{(\varepsilon_r - 1)\left[1 - \beta^2 - \beta\left(\varepsilon_r - \sin^2\theta\right)^{1/2}\right]}{\left[\varepsilon_r\cos\theta + (\varepsilon_r - \sin^2\theta)^{1/2}\right]\left[1 - \beta(\varepsilon_r - \sin^2\theta)^{1/2}\right]} \right|^2 \qquad (3\text{-}7)$$

In the limit of $|\varepsilon_r| \to \infty$ corresponding to plasma, Equation 3-8 can be written as

$$\frac{d^2W}{d\omega d\Omega} = \frac{e^2}{\pi^2 c}\frac{\beta^2\sin^2\theta}{(1-\beta^2\cos^2\theta)^2} \tag{3-8}$$

The formation length L_f for a medium with relative dielectric constant ε_r is written as

$$L_f = \frac{c}{\omega}\frac{\beta}{|1-\beta\varepsilon_r{}^{1/2}\cos\theta|} \tag{3-9}$$

In the case of dielectric constant ($\varepsilon_r \simeq 1$) and the emission angle $\theta \simeq 1/\gamma$, the formation length L_f can be approximately written as

$$L_f \simeq \frac{c}{\omega}\gamma^2 \tag{3-10}$$

The total emitted TR energy W per unit angular frequency and unit solid angle is given as

$$\frac{d^2W}{d\omega d\Omega} = \frac{e^2N}{\pi^2 c}\left[\int d^3p\left(\varepsilon_{\parallel}{}^2+\varepsilon_{\perp}{}^2\right)\right. \tag{3-11}$$
$$\left. +(N-1)\left(\left|\int d^3p g(p)\varepsilon_{\parallel}F\right|^2+\left|\int d^3p g(p)\varepsilon_{\perp}F\right|^2\right)\right]$$

Here g(p) shows the momentum distribution function of electrons, $\varepsilon_{\parallel}$ and $\varepsilon_{\perp}$ are the Fourier-transformed electric fields in the plane parallel and perpendicular to the radiation plane, respectively. F is a coherence function considering the exact time and position when the electrons reaches at the interface. Considering the interface between a perfect conductor and vacuum is reasonable assumption, $\varepsilon_{\parallel}$ and $\varepsilon_{\perp}$ can be simplified,

$$\varepsilon_{\parallel}(\theta,\alpha,\phi,\psi,u) = \frac{u\cos\psi\left[u\sin\psi\cos(\phi-\alpha)-\left(1+u^2\right)^{1/2}\sin\theta\right]}{\left[(1+u^2)^{1/2}-u\sin\psi\cos(\phi-\alpha)\sin\theta\right]^2-u^2\cos^2\psi\cos^2\theta} \tag{3-12}$$

$$\varepsilon_{\perp}(\theta,\alpha,\phi,\psi,u) = \frac{u^2\cos\psi\sin\psi\sin(\phi-\alpha)\cos\theta}{\left[(1+u^2)^{1/2}-u\sin\psi\cos(\phi-\alpha)\sin\theta\right]^2-u^2\cos^2\psi\cos^2\theta} \tag{3-13}$$

The coherence function depends on the phase term from the case of single-electron. The coherence function F is given by

$$F = \frac{1}{g(\boldsymbol{p})}\int d^2\boldsymbol{r}_{\perp}e^{-ik_{\perp}\cdot\boldsymbol{r}_{\perp}}\int_{-\infty}^{+\infty}dt e^{iz(\omega-k_{\perp}\cdot v_{\perp})/v_z}h(\boldsymbol{r},\boldsymbol{p}) \tag{3-14}$$

here $h(r, p)$ is the normalized six-dimensional electron distribution function. The $\perp$ and z subscripts shows the projections onto the plane of the interface and onto the z-axis, respectively.

The coherence function F is rewritten as

$$F = \frac{1}{g(\boldsymbol{p})} \int d^2\boldsymbol{r}_\perp e^{-ik_\perp \cdot \boldsymbol{r}_\perp} \int_{-\infty}^{+\infty} dt e^{i\omega t} h(\boldsymbol{r}_\perp, t, \boldsymbol{p}) \tag{3-15}$$

If a time and space function of the six dimensional distribution function are independent, the coherence function F can be factorized into the product,

$$F(\omega, \boldsymbol{k}_\perp, \boldsymbol{p}) = F_1(\omega, \boldsymbol{p}) F_1(\boldsymbol{k}_\perp, \boldsymbol{p}) \tag{3-16}$$

The phase term that enters in Equation 3-15 is

$$\Phi = \boldsymbol{k}_\perp \cdot \boldsymbol{r}_\perp - \omega t \tag{3-17}$$

With reference to Figure 3.7 (left), consider two charged particles at positions $A_1 = (r_{\perp 1}, 0)$ and $A_2 = (r_{\perp 2}, 0)$. The two particles reach the interface at the times t_1 and t_2, respectively. An observer at point C, which is arbitrary in the x–z plane, is at a distance L from the origin and the observation vector forms an angle θ with the z-axis.

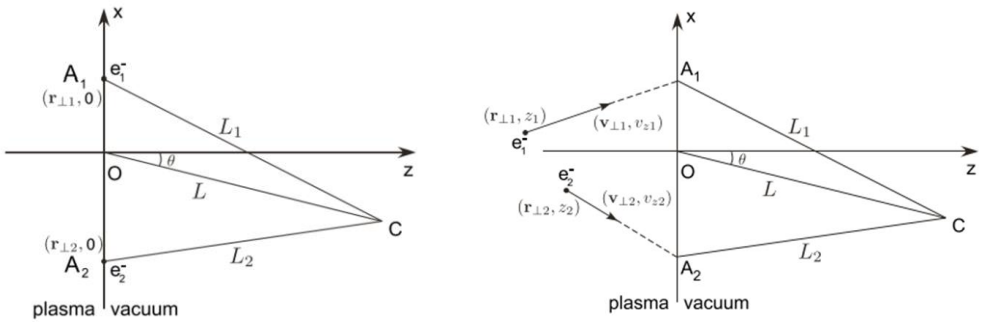

Figure 3.7 Parameters for the evaluation of the phase term of single electron for different geometrical case.

The plane waves emitted at positions A_1 and A_2 reach the observer after having travelled a distance L_1 and L_2, respectively. It is readily seen that

$$L_{1,2}^2 = \overline{OA}_{1,2}^2 + L^2 - 2\overline{OA}_{1,2} L \sin\theta \tag{3-18}$$

Subtracting the two relations leads to

$$L_1 - L_2 = \frac{\overline{OA}_1^2 - \overline{OA}_2^2 - 2\left(\overline{OA}_1 - \overline{OA}_2\right)\sin\theta}{L_1 + L_2} \tag{3-19}$$

Assuming that the observer is in the radiation zone the equation 3-19 can be

$$L_1 - L_2 \simeq \left(\overline{OA}_2 - \overline{OA}_1\right)\sin\theta \tag{3-20}$$

At this point the phase difference between the two waves can be determined, which is the sum of a spatial s and a temporal t component. The spatial phase From equation (17) and defining $|k_\perp| = \omega/c \sin\theta$ as the component of the wave vector in the plane x–y,

$$\Delta\Phi_s = 2\pi\frac{L_1 - L_2}{\lambda} \simeq (\overline{OA}_2 - \overline{OA}_1)\sin\theta \tag{3-21}$$

The temporal component is

$$\Delta\Phi_t = \omega(t_2 - t_1) \tag{3-22}$$

When the two particles reach the interface with a time difference $\tau_{1,2} = -z_{1,2}/v_{z1,2}$, their distance from the origin is written as

$$\overline{OA}_{1,2} = r_{\perp 1,2} - v_{\perp 1,2}\frac{z_{1,2}}{v_{z1,2}} \tag{3-23}$$

From equations 3-23 and 3-20, the spatial phase difference is given by

$$\Delta\Phi_s = 2\pi\frac{L_1 - L_2}{\lambda} = \boldsymbol{k}_\perp \cdot (\boldsymbol{r}_{\perp 2} - \boldsymbol{r}_{\perp 1}) - \boldsymbol{k}_\perp \cdot \left(\frac{z_2}{v_{z2}}\boldsymbol{v}_{\perp 2} - \frac{z_1}{v_{z1}}\boldsymbol{v}_{\perp 1}\right) \tag{3-24}$$

The temporal term is given by

$$\Delta\Phi_t = \omega\left(\frac{z_2}{v_{z2}} - \frac{z_1}{v_{z1}}\right) \tag{3-25}$$

Therefore, from the total phase difference $\Delta\Phi = \Delta\Phi s + \Delta\Phi_t$ the phase term in equation 3-14 can be described as

$$\Phi = \boldsymbol{k}_\perp \cdot \boldsymbol{r}_\perp + \frac{z}{v_z}(\omega - \boldsymbol{k}_\perp \cdot \boldsymbol{r}_\perp) \tag{3-26}$$

3.5 Diagnostics for K-shell radiation imaging and spectroscopy

3.5.1 K-shell ionization cross-section [7]

When the electron with energy higher than the binding energy of the K-shell incident, the K-shell electron is kicked out. When an ionization process occurs, the ion can decay down to a more stable state by filling-in the inner shell gap with an electron coming from an outer shell. The released energy is transferred to another atomic electron (Auger electron) or to be emitted as a characteristic X-ray.

Kα transitions are split into two possible transitions, Kα_1 ($2p_{1/2}$-1s) and Kα_2 ($2p_{3/2}$-1s), respectively. K$_\beta$ ($3p$-1s) emission also occur less possible than the Kα emission. These energy levels for copper atoms are shown in Figure 3.9.

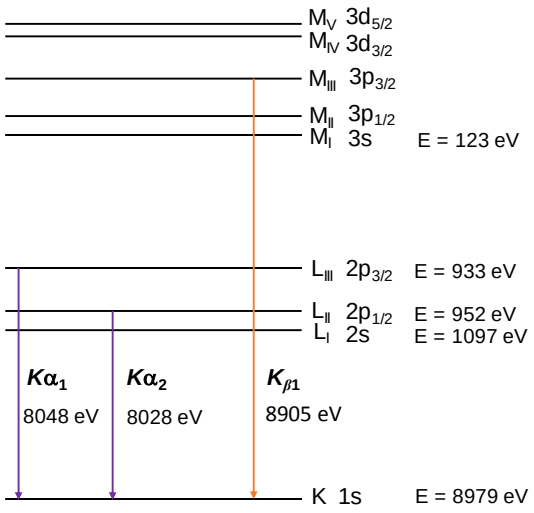

Figure 3.9 The energy levels for copper atoms.

The K-shell emission cross-section can be written by following,

$$\sigma_{\mathrm{K}} = f_{\mathrm{K}}\sigma_{\mathrm{ion}} \tag{3-27}$$

where $\sigma_{\mathrm{ion}}$is K-shell ionization cross-section. f_{K} is fluorescence yield, which can be expressed

with obtained by fitting measurements all used fluorescence yield.

$$f_{\mathrm{K}} = 0.985\frac{(\mathrm{Z}/30.896)^{3.847}}{1+(\mathrm{Z}/30.896)^{3.847}} \tag{3-28}$$

σ_{ion} can be described by Hombourger's expression as follows,

$$\sigma_{\mathrm{ion}} = \sigma_0 G'\left(\frac{R}{B}\right)^{f}\left(1-\frac{1.335}{U}+\frac{0.6006}{U^2}\right)\ln U \tag{3-29}$$

Here $U = E/B$ is dimensionless parameter called overpotential. R is Rydberg energy (13.606 eV). B is binding energy.

$$\sigma_0 = \frac{N_{\mathrm{K}}175}{B_{\mathrm{keV}}^{1.0305}} \text{ barns} \tag{3-30}$$

$$f = -\frac{0.316}{U}+\frac{0.1545}{U^2} \tag{3-31}$$

Grysinski's relativistic factor can be written as follows,

$$\mathrm{G} = \frac{1+2J}{U+2J}\left(\frac{U+J}{1+J}\right)^2\left[\frac{(1+U)(U+2J)(1+J)}{J^2(1+2J)+U(U+2J)(1+J)^2}\right]^{1.5} \tag{3-32}$$

which is intended to convert a nonrelativistic expression for energy exchange in a binary collision between electrons with kinetic energies E and B to a relativistically correct expression. Here the new parameter G' can be expressed as,

$$\mathrm{G}' = \frac{G}{2(\gamma-1)} = \frac{JG}{2U} \tag{3-33}$$

Davies' expression for the K-shell emission cross-section of copper is

$$\sigma_{\mathrm{K,Davies}} = \left(1-\frac{0.2824}{U}\right)\left(\frac{20.95}{\beta^2}\right)\times\ln\left[\left(\frac{U+113.8}{114.8}\right)^{1/2}\frac{57.0098U}{56.9+0.1098U}\right] \text{ barns} \tag{3-34}$$

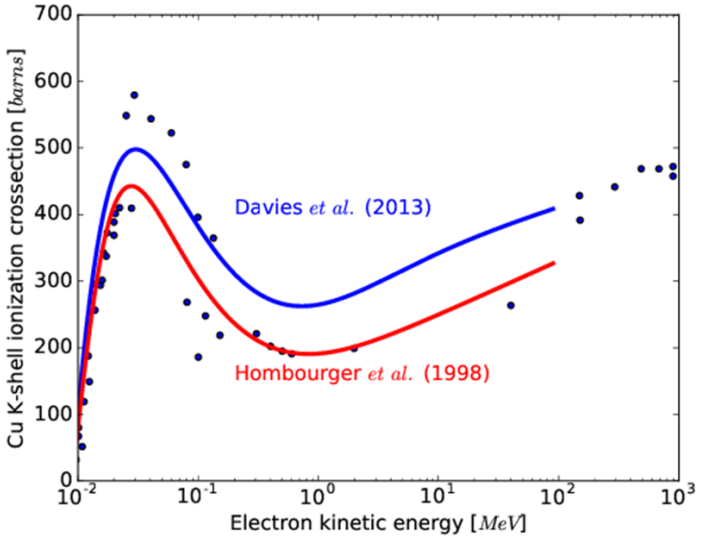

Figure 3.10. Davies and Hombourger's K-shell emission cross-section of copper.

3.5.5 Spherically bent crystal imager [8]

A spherical crystal microscope is widely used to investigate the REB transport and its energy deposition region in HED physics experiments. In that experiment, middle-Z tracer is used as X-ray sources (emission of He-like ions or from cold Kα emission.). The emitted or transmitted through the object X-rays is imaged with a spherically bent Bragg crystal imager. This must be operated at near-normal incidence to reduce aberrations. Figure 3.11 shows the schematic view of the system for X-ray backlight imaging with a 2D curved Bragg crystal. In the backlight imaging experiment, a high intensity, short pulse laser is irradiated at a metal plate to generate monochromatic X-ray (characteristic X rays) as a probing beam. The generated X-ray pulse duration is much shorter than the time scale of hydrodynamic motion, which enable us to provide the correct transmitted image without blur.

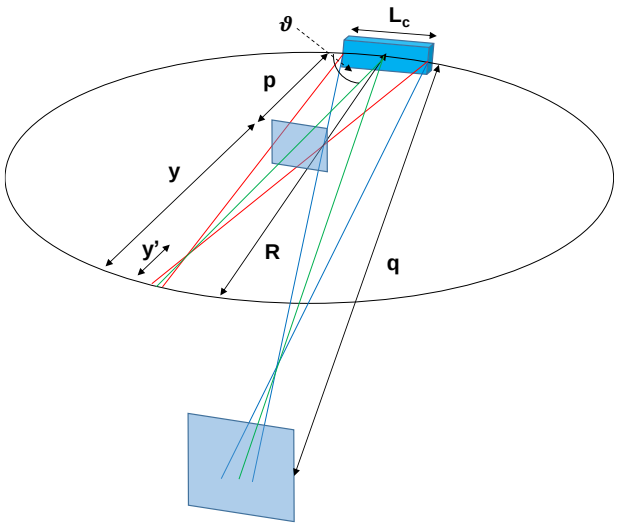

Figure 3.11 Schematic view of the backlight system using a spherically bent crystal with aperture L_c and a laser-produced X-ray source inside the Rowland circle.

The paraxial lens equations that govern image formation of a toroidal crystal are known as Coddington's equations,

$$\frac{1}{p}+\frac{1}{q_m}=\frac{2}{R_m \sin\vartheta} \tag{3-35}$$

$$\frac{1}{p}+\frac{1}{q_s}=\frac{2\sin\vartheta}{R_s} \tag{3-36}$$

The distance p needs to satisfy below relation to image,

$$R_m \sin\vartheta > p > \frac{R_m \sin\vartheta}{2} \tag{3-37}$$

The meridional (f_m) and sagittal (f_s) focal lengths are different for Bragg angles $\vartheta \neq 90°$. f_m and f_s can be written as respectively,

$$f_m=\frac{R_m \sin\vartheta}{2} \tag{3-38}$$

$$f_s=\frac{R_s}{2\sin\vartheta} \tag{3-39}$$

A toroidal crystal can achieve equal focal lengths when R_s can be written as

$$R_s = R_m \sin^2 \vartheta \tag{3-40}$$

The object must be set at two different distances in the meridional and sagittal planes

$$p_m = \frac{R_m (M+1) \sin \vartheta}{2M} \tag{3-41}$$

$$p_s = \frac{R_s (M+1)}{2M \sin \vartheta} \tag{3-42}$$

If the mirror is operated at near-normal incidence ($\sin \vartheta \approx 1$), a spherical crystal system realizes a good image.

$$p = \frac{R}{2} \frac{M+1}{M} \tag{3-43}$$

which is approximately midway between p_m and p_s. The image distance can be expressed as

$$q = \frac{R}{2 - R/p} \tag{3-44}$$

When the X-ray source is located on the Rowland circle, the distance y between object and source is given by

$$y = R \sin \vartheta - p \tag{3-45}$$

By differentiating the Bragg equation, the angular range $\Delta\vartheta$ can connect to the spectral bandwidth $\Delta E/E$,

$$\Delta\vartheta = \frac{\Delta E}{E} \tan \vartheta \tag{3-46}$$

Here, ΔE is the FWHM of the spectral line. The spatial extent Δs line of a spectral line projected to the Rowland circle (assuming zero curvature) can be written as

$$\Delta\vartheta = R \sin \vartheta \tan \vartheta \frac{\Delta E}{E} \tag{3-47}$$

Figure 3.12 shows diagram of spatial resolution vs Bragg angle. Spatial resolution strongly depends on Bragg angle. Even though it has lower magnification, the spatial resolution for the case of backlight system has much better resolution compared to the self emission imager.

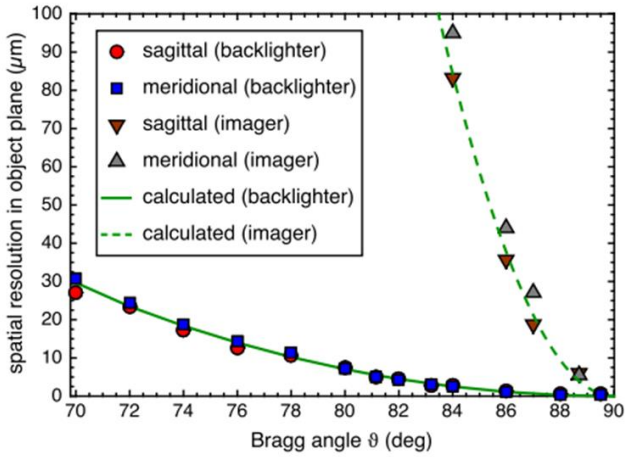

Figure 3.12 Spatial resolution vs Bragg angle.

3.5.4 Highly oriented pyrolytic graphite (HOPG) crystal [9]

HOPG consists of a large number of small crystallites which is called a mosaic crystal. The angular distribution of the crystallites, with plane orientations off the normal axis to the surface, is called mosaic spread. Even for a fixed angle of incidence to the crystal surface, mosaicity makes it possible that an energy distribution of photons can be reflected. Each photon of this energetic distribution can be incident into a crystallite plane at the right Bragg angle. Therefore the mosaicity can realize the dramatic increase of integral reflectivity for mosaic crystals compared to perfect crystals. The width of the reflected energy distribution of photons depends on the mosaic spread. The mosaicity also gives rise to mosaic focusing (parafocusing), which further enhances the intensity in the image plane.

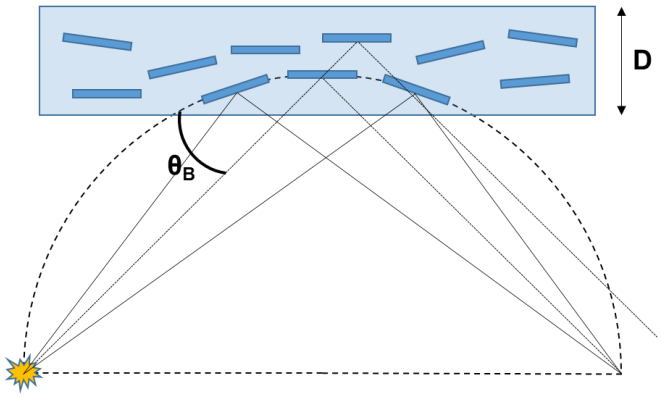

Figure 3.2 Diffraction properties of HOPG.

3.6 Summary of Section 3

In fast isochoric heating scheme, a characterization of the energy and spatial distribution of REB as well as deposited energy into the dense core plasma and its density are most important parameters. By measuring an absolute number and energy distribution of converted X-ray, an accurate number of REB at the generation point can be without being affected by self-generated electrostatic and magnetic fields at the target surface. X-ray imaging technique, for backlight and self-emission (Kα X ray), provides a density distribution of dense plasma and energy deposition region by REB, respectively. From an absolute number of Kα X ray induced by REB recorded with a X-ray spectrometer using a Bragg crystal, the laser-to-core energy coupling can be estimated. The obtained results by these diagnostics will be describe in the later section.

The author developed the photonuclear reaction based high-energy X-ray spectrometer shown in ref. [4] to characterize the absolute number and energy distribution of laser-accelerated electron beams. The author also contributed to proof-of-principle experiment of the Compton X-ray spectrometer shown in ref. [3]

References in **Section3**

[1] T. Ozaki, S. Kojima, Y. Arikawa, H. Shiraga, H. Sakagami, S. Fujioka, and R. Kato *An*

electron/ion spectrometer with the ability of low energy electron measurement for fast ignition experiments. Rev. Sci. Instrum. **85**, 11E113 (2014).

[2] C. D. Chen, J. A. King, M. H. Key, K. U. Akli, F. N. Beg, H. Chen, R. R. Freeman, A. Link, A. J. Mackinnon, A. G. MacPhee, P. K. Patel, M. Porkolab, R. B. Stephens, and L. D. Van Woerkom *A Bremsstrahlung spectrometer using K-edge and differential filters with image plate dosimeters*. Rev. Sci. Instrum. **79**, 10E305 (2008).

[3] S. Kojima, T. Ikenouchi, Y. Arikawa, **S. Sakata**, Z. Zhang, Y. Abe, M. Nakai, H. Nishimura, H. Shiraga, T. Ozaki, S. Miyamoto, M. Yamaguchi, A. Takemoto, S. Fujioka and H. Azechi *Development of Compton X-ray spectrometer for high energy resolution single-shot high-flux hard X-ray spectroscopy*. Rev. Sci. Instrum. **87**, 043502 (2016).

[4] **S. Sakata**, Y. Arikawa, S. Kojima, T. Ikenouchi, T. Nagai, Y. Abe, H. Inoue, A. Morace, M. Utsugi, R. Kato, H. Nishimura, M. Nakai, H. Shiraga, S. Fujioka and H. Azech *Photonuclear reaction based high-energy x-ray spectrometer to cover from 2 MeV to 20 MeV.* Rev. Sci. Instrum. **85**, 11D629 (2014).

[5] H. Ing, R. A. Noulty & T. D. McLean *Bubble detectors - A maturing technology*. Radiat. Meas. **27**, 1 (1997).

[6] C. Bellei, J. R. Davies, P. K. Chauhan and Z. Najmudin *Coherent transition radiation in relativistic laser–solid interactions*. Plasma Phys. Control. Fusion **54**, 035011 (2012).

[7] J. R. Davis, R. Betti, P. M. Nilson, and A. A. Solodov *Copper K-shell emission cross sections for laser-solid experiments.* Phys. Plasmas. **20**, 083118 (2013).

[8] M. S. Schollmeier, M. Geissel, J. E. Shores, I. C. Smith and J. L. Porter *Performance of bent-crystal x-ray microscopes for high energy density physics research.* Appl. Optics **54**, 5147 (2015).

[9] H. Legall, H. Stiel, V. Arkadiev, and A.A. Bjeoumikhov *High spectral resolution x-ray optics with highly oriented pyrolytic graphite*. Opt. Express **14**, 4570 (2006).

4. Current states of fast ignition experiments

This section summarizes the current status of electron-based FI and relevant experiments. Three critical problems have been recognized as obstacles to the efficient fast heating. The first problem is that the REB becomes too energetic to heat the core in a long-scale-length pre-plasma filled in the cone, the second one is that a part of the REB is scattered and absorbed in a high-Z cone tip. The third one is that the REB has a large divergence of 100 deg. as a typical full-angle, so that only a small fraction of the diverged REB can collide with the core after the long distance transport. Approaches to overcome critical problems are described in this section.

4.1 Controlling of REB energy distribution

4.1.1 Improvement of laser pulse contrast

Figure 4.1 shows a typical energy distribution of laser accelerated REB using block target described in section 1. Only 8 % of total energy of REB that contribute to efficient energy deposition to a dense core plasma was observed.

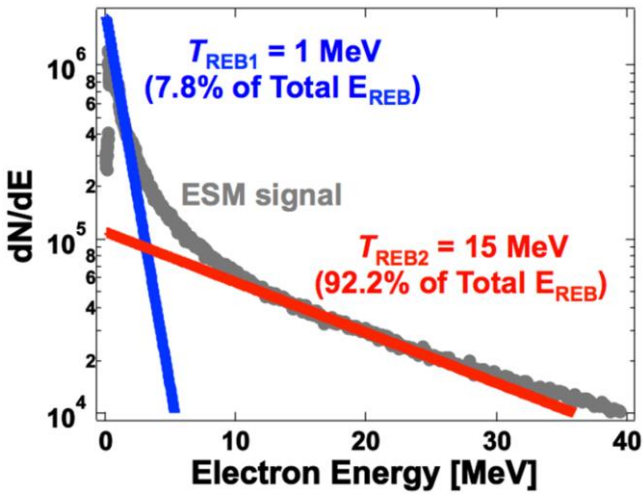

Figure 4.1 Typical electron energy distribution recoded by the magnet-base electron energy analyzer. Ref. [] from Section 1.

When a high-intensity laser pulse interacts the long-scale plasma (pre-formed plasma), the energetic electrons are produced mainly in the pre-plasma region and their energy are much higher than those for the case without the pre-plasma due to larger interaction length.

Figure 4.2 shows results of particle-in-cell simulation. Much higher energy electron is clearly seen in the case of with a pre-plasma.

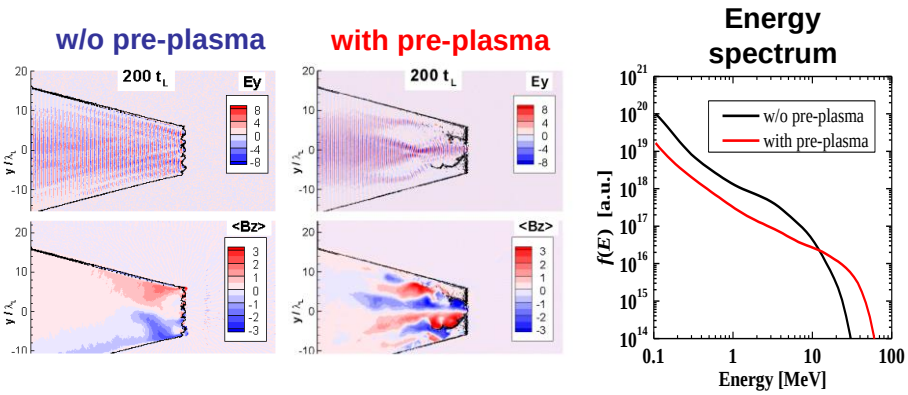

Figure 4.2 Spatial profiles of laser electric and magnetic fields for with and without pre-plasma (left). Time- and space-integrated fast electron energy spectrum (right).
Images taken from Johzaki *et al.,* [1]

4.1.2 Improvement of laser pulse contrast [2,3]

Plasma mirror (PM) is used to improve the laser pulse contrast, which reduces a pre-formed plasma. The PM consists of a transparent dielectric (BK7 glass) with an antireflective (AR) coating. The reflectivity of is about 0.1%. The plasma is generated on the surface of the PM by laser flux above the breakdown threshold. Figure 4.3 shows schematic view of operating principle of the PM. When the plasma at the critical density ($n_c = 1.1 \times 10^{21}$ cm^{-3} for a 1.053 μm laser) is generated, the main laser pulse is reflected in the same fashion as a classic metal mirror. The pre-pulse flux on the PM with is lower than the breakdown threshold and is then transmitted, increasing the pulse contrast by almost three orders of magnitude.

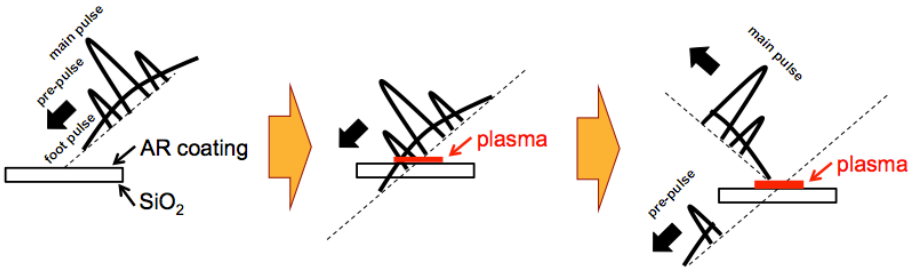

Figure 4.3 Schematic view of operating principal of the plasma mirror.

Figure 4.4 shows Comparison of laser pulse with and without PM. The blue line shows the nanosecond and picosecond components of the laser pedestal. In the clearly noticeable from the change in pattern at −0.3 ns. The red line represents the upper boundary of the estimated pedestal level with the PM. In the last 100ps before the main pulse it is possible to generate a pre-plasma on the front surface.

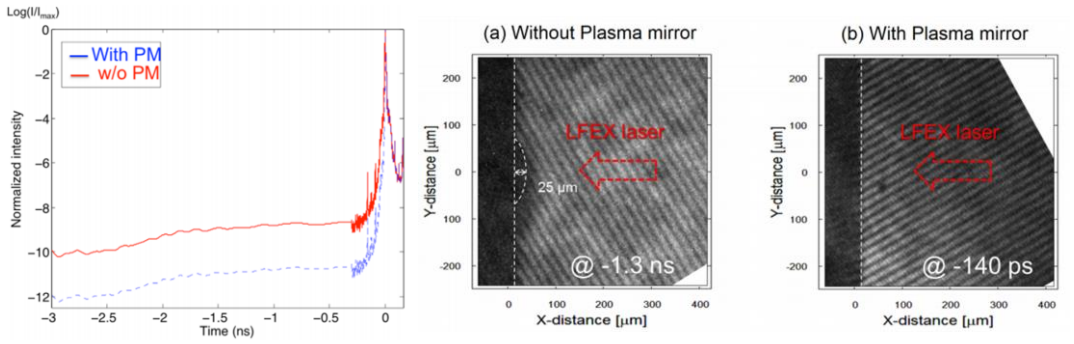

Figure 4.4 Comparison of laser pulse with and without PM (left). Comparison of interferometry image with and without PM.
Images taken from Morace *et al.,* [3]

4.2 Formation of high-areal density core plasma by cone-in-shell target [4]

The experiment for high-areal density formation by using a cone-in-shell target was carried out at OMEGA laser facility. The experimental configurations are shown in Figure 4.7. The shell is irradiated by 54 OMEGA ultraviolet beams to assemble the high-density core plasma. The OMEGA EP laser was focused to a Cu foil to produce the Kα X-ray emission around the maximum compression timing. The transmitted Kα X-ray through a compressed shell target was imaged with a spherical Bragg bent crystal imager onto an imaging plate.

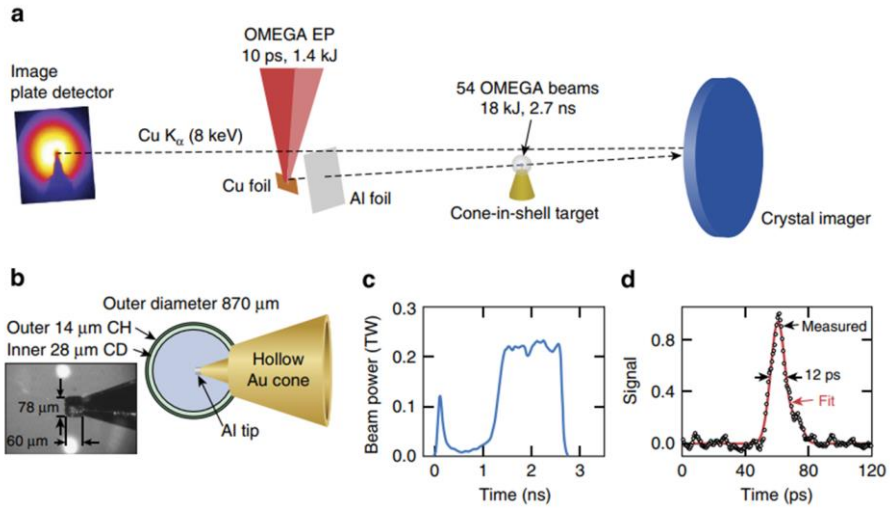

Figure 4.5 (a) Schematic view of the experimental setup for X-ray flash backlight measurement. (b) A photograph of cone-in-shell target. (c) Laser pulse shape for implosion of the shell. (d) Time history of the generated Kα X-ray emission.
Image taken from Theobald *et al.,* [4].

The measured and computed areal density for various times are shown in Figure 4.10. The experimental data sets are in good agreement with the hydrodynamic simulation. High-areal density (~ 0.3 g / cm^3) was formed at distance of ~ 50 μm in front of the cone tip. Such areal density is enough to stop REB with the energy from 1 to 3 MeV, which is required for igniting the fuel.

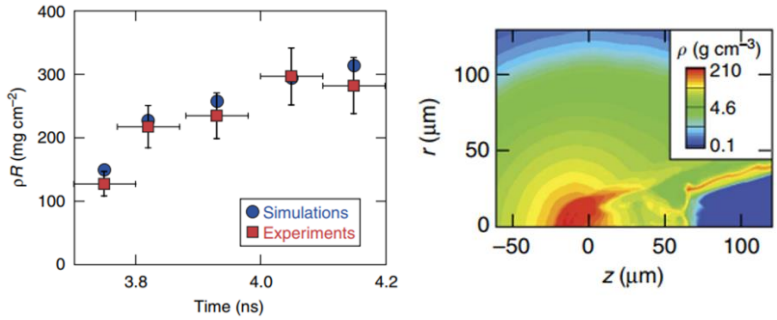

Figure 4.6 Measured and computed areal density for various times (left). Computed mass density profile at 3.96 ns (right).

Image taken from Theobald *et al.,* [4]

4.3 Formation of high-areal density core plasma by solid sphere target

4.3.1 Stable dense core plasma formation [5]

The experiment was conducted at GEKKO-XII and LFEX laser facility. A 200 μm diameter solid CD sphere was attached to a Au cone, whose open angle, wall thickness, and tip diameter were 45 degrees, 7 μm, and 100 μm, respectively. The sphere was irradiated by 9 GEKKO-XII beams without spatial beam smoothing. Around the maximum compression time, Kα X-ray was produced by LFEX laser irradiating on the Ti plate. The transmitted X-ray through the compressed sphere was imaged by a spherically bent crystal imager.

Figure 4.2 shows optical depth profiles of the compressed sphere attached a gold cone target for different time from the laser peak. The formation of a dense core plasma well separated from the con tip can be clearly seen at 4.38 ns in Figure 4.2. Comparison between experimental and computed areal density are shown in Figure 4.3.

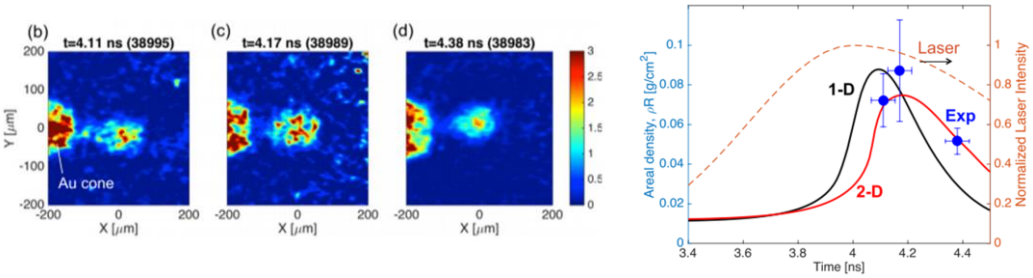

Figure 4.7 Experimental optical depth profiles for different time from the laser peak (left). Comparison between experimental and computed areal density (right).

Image taken from Sawada *et al.,*[5]

The inferred ρRs with the overall errors are 72 +/- 13 mg/cm^2, 87 +/- 26 mg/cm^2, and 51 +/- 7 mg/cm^2 at t = 4.11, 4.17, and 4.38 ns, respectively. These experimental data agrees with the 2D hydrodynamic simulation. High-areal density core plasma was assembled stably despite no spatial beam smoothing.

4.3 Controlling of the large divergence of REB by self-generated magnetic fields

4.3.1 Angular distribution of laser-produced REB [7]

Figure 4.11 shows rear side emission for various thickness. The measured divergence angle

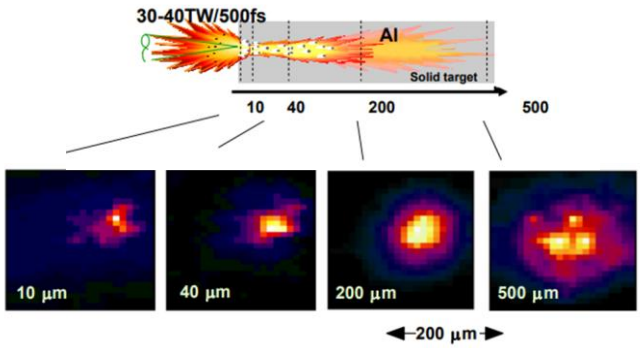

Figure 4.11 REB divergence angle as a function of laser intensity.
Image taken from R. Kodama *et, al.*, [7]

Figure 4.12 shows REB divergence angle as a function of laser intensity. The REB has a large divergence of >70 deg. as a typical full-angle at the intensity 10^{19} W/cm^2, so that only a small fraction of the diverged REB collides with the core.

There are two possible explanations for the increase of divergence with intensity. According to previous simulation by Wilks *et al*., [], a rippled density surface at the target front with the scale of the laser wavelength in addition to the larger scale hole boring is created. The laser fields around the ripple surface determines the electron beam divergence. One might then expect the beam divergence with very short laser pulses, say less than 50 fs, to be smaller than for pulses of 100 fs or more. Simulations performed by Ren *et al*. [8] and Adam *et al*. [9] have predict that the

large electron divergence is due to deflection by strong magnetic fields produced by the filamentation instability of the electron beam as it propagates through the target.

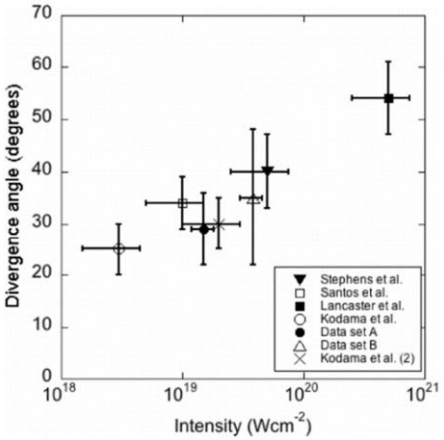

Figure 4.12 REB divergence angle as a function of laser intensity.
Image taken from J. S. Green *et, al.*, [7]

4.3.2 Resistive guiding concept [10, 11]

This scheme is based on using a structured target in which the resistivity (through the atomic number Z) varies in the direction transverse to the electron beam propagation. The physical basis of this is that to leading order the magnetic field grows according to

$$\frac{\partial B}{\partial t} = \eta \nabla \times \mathbf{j} + (\nabla \eta) \times \mathbf{j} \qquad (4\text{-}1)$$

The second term in the right-hand side of Equation 4-1 implies that a magnetic field will grow at resistivity gradients which acts to drive electrons into the regions of higher resistivity.

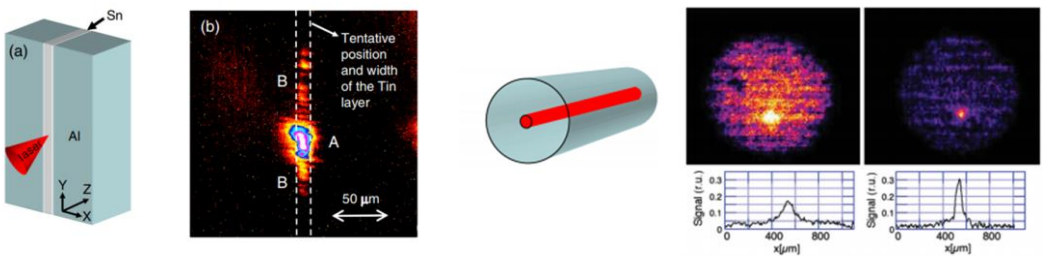

Figure 4.13 Schematic view of the sandwich target. The experimentally obtained time-integrated image of optical transition radiation from the rear side (left).
Images taken from Kar *et al.*,[10] and Ramakrishna *et al.,* [11].

4.4 Controlling of the large divergence of REB by external magnetic fields

4.4.1 Concept of guiding of REB by external magnetic fields [12, 13, 14, 15]

When a strong external magnetic field is applied along the direction of electron beam propagation, the electrons' motion in the direction perpendicular to the beam propagation is limited. Efficient beam transport along the beam direction can expected.

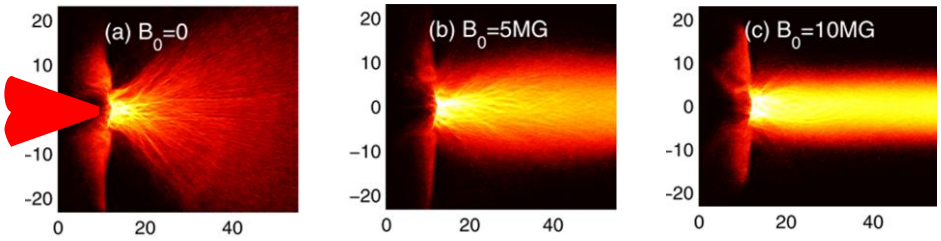

Figure 4.14 The REB energy density distribution with energy between 0.5 < E (MeV) < 5 for different imposed magnetic fields. (left) without B-fields. (middle) B = 5 MG (500 T), (right) B = 10 MG (1 kT).
Image taken from Cai *et al.,* [12]

Figure 4.5 shows the REB energy density distribution with energy between 0.5 < E (MeV) < 5 for different imposed magnetic fields along the path of REB obtained by particle-in-cell simulation. The produced REB are very divergent for the case without imposed external magnetic fields. On the other hand, it is clearly seen that REB is guided by imposed external magnetic fields along the field lines.

4.4.2 Generation of kilo-Tesla magnetic fields by laser-driven capacitor-coil target [16, 17]

Two nickel disks are connected by a U-turn coil. Kilojoule, nanosecond laser pulses are focused onto the first disk through a hole in the second disk. A plasma is generated at the first disk, and suprathermal hot electrons with temperatures exceeding 10 keV are emitted from the plasma corona. The hot electrons stream down the electron density gradient ahead of the expanding plasma plume and impact the second disk. The second disk acquires a negative charge, and a large electrical potential develops between the disks. That potential difference drives a current in the U-turn coil. A strong magnetic field pulse is generated in the coil.

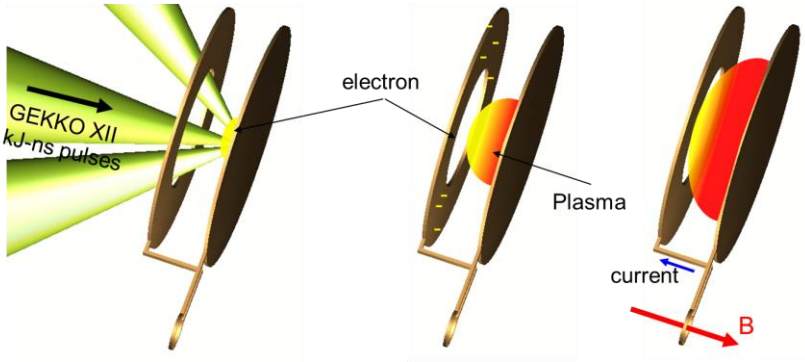

Figure 4.15 Schematic view of laser-driven capacitor-coil target.

$$V_c = R_c I_c + L_c \frac{dI_c}{dt} \tag{4-1}$$

R_c is the coil resistance and L_c is the inductance.
They are described as follows,

$$R_c = \eta l_w / s_w$$
$$L_c \simeq \mu_0 a \ln(a/b) \tag{4-1}$$

The nikel

$\eta_{\mathrm{Ni}} \simeq 7 \times 10^{-8} \Omega\mathrm{m}$

The charging diode current

$$I_d = e\pi r_h^2 n_h \Delta\Omega \int_{eV_c}^{\infty} d\varepsilon v f_h(\varepsilon) \tag{4-1}$$

$$C_d V_c = \int_0^t d\,t' I_d(t') \tag{4-1}$$

The diode potential

$$eV_c \simeq T_h \ln\left(\frac{\omega_{ph}^2 t_{las} d}{v_h} \frac{r_h^2}{S_d}\right) \tag{4-1}$$

$eV_c =$

$$C_d V_c = \int_0^t d\,t' I_d(t') \tag{4-1}$$

4.4.3 Direct measurement of laser-driven magnetic fields by proton deflectmetry [18, 19, 20]

A differential magnetic probe (so-called B-dot probe) was used in previous experiments to measure both amplitude and temporal evolutions of the magnetic field. However, it could provide a precise measurement only if the probe is set several centimeters away from the coil center to avoid hard X-ray ionization and the too high voltage induced by the extremely rapid temporal change of the B-field amplitude. The Faraday rotation measurement was also used to measure the magnetic field. A strong limitation for this diagnostic is represented by the rapid increase in optical density of the Faraday medium due to the large electric current induced by the sharply increasing magnetic field flux. Therefore, the Faraday rotation measurement provides only the initial rising edge of the magnetic field. As well as B-dot probe measurement, this has an uncertainty due to

On the other hand, proton deflectometry technique enables to direct measurement of magnetic fields by a laser-driven capacitor-coil target compared to above techniques. Figure 4.6 shows the experimental set up for direct measurement of magnetic fields by proton deflectmetry at the GEKKO-LFEX laser facility [19].

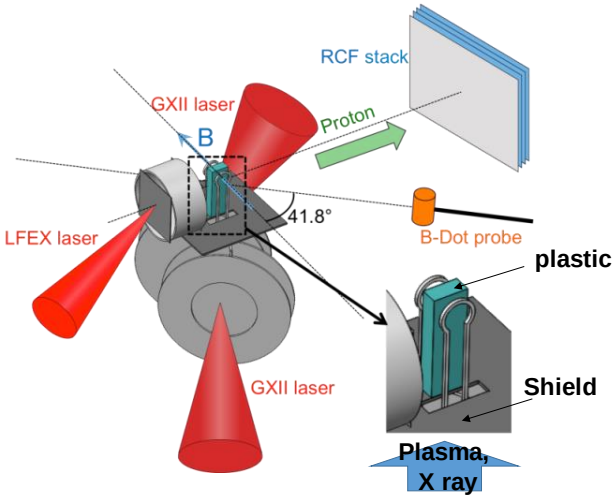

Figure 4.15 Experimental set up for generation of magnetic fields with two laser-driven capacitor-coil targets. Between the two coils, a 250 μm-thick polystyrene foil was placed to investigate magnetic field diffusion in the plastic medium.

A 610 +/- 30 T of B-field was evaluated from the experimentally obtained proton pattern comparing with Monte-Carlo calculations. The experimental results and calculations are shown in Figure 4.16. Distributions of normalized proton number along the line connecting two sideway

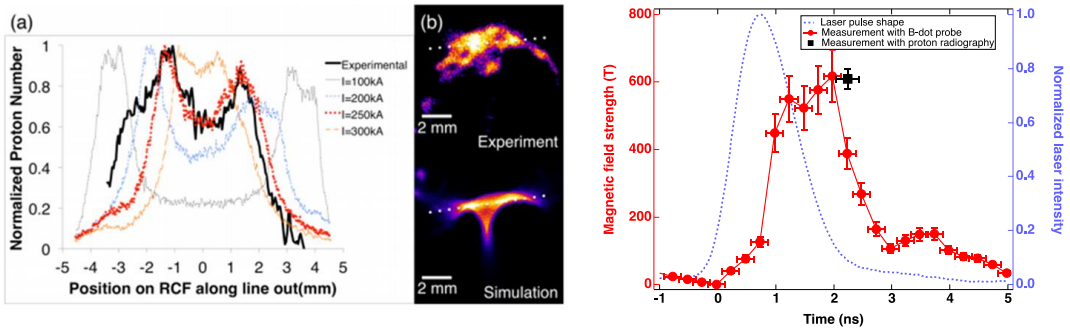

Figure 4.16. Distributions of normalized proton number along the line connecting two sideway spots (left). Proton patterns obtained from experiment and from simulation corresponding to 610 T (middle). Temporal evolution of evaluated magnetic field amplitude at coil center (red solid line) and GEKKO XII laser pulse (blue dotted line) (right).

spots are compared between the experimental signal and the simulated one. The obtained value from the proton deflectmetry was consistent with the amplitude independently measured by B-dot probe. The pulse width of B-field was 2 ns (FWHM). This can be explained considering the

change in coil resistivity due to wire Ohmic heating. Figure 4.18 shows optical shadow graphic image of time evolution of coil expansion.

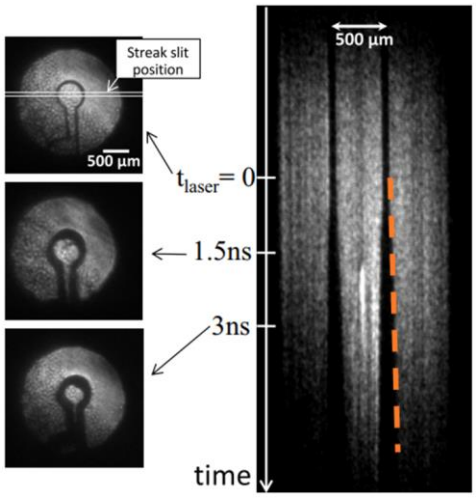

Figure 4.17. Optical shadow graphic image of time evolution of coil expansion for gated (left) and streak (right) image, respectively.
Image taken from

4.3.5 Guiding of relativistic electron beams in dense matter by laser-driven magnetostatic fields [21]

The experiments were carried out at the LULI pico 2000 laser facility. The Ni coil target was irradiated to produce kilo-Tesla level magnetic fields by a long-pulse laser beam (LP laser), whose wavelength, pulse shape, pulse duration, energy and intensity were 1.06 μm, flat top, 1 ns, 500 +/- 30 J, (1.4 +/- 0.6) $\times 10^{17}$ W / cm^2, respectively. At different delays Δt with respect to the LP-laser, a high-intensity short pulse beam (SP laser) was focused into the REB transport target at normal incidence to produce REB. The duration, energy and intensity of SP laser were 1ps, 47-49 J, (1.5-3) $\times 10^{19}$ W / cm^2, respectively. The schematic view of experimental configuration is shown in Figure 4.17 (left).

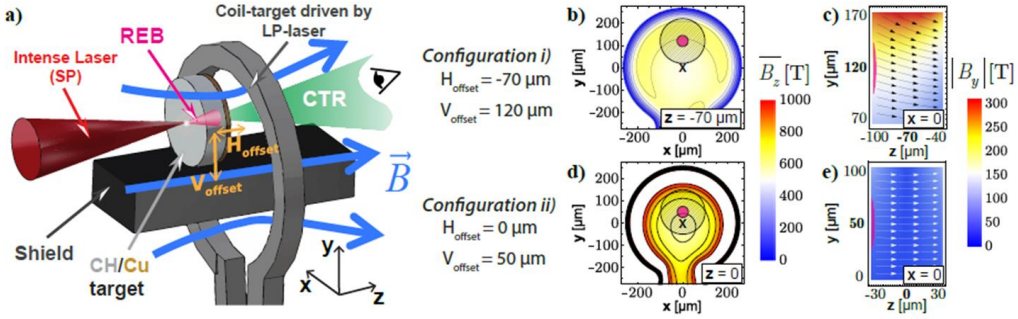

Figure 4.18 Experimental configuration for REB guiding with imposed B-field (left). Amplitude of the B-field longitudinal and vertical component for two configuration (right). Images taken from Bailly-Grandvaux *et al.,* [21]

The REB transport targets were 200 µm-diameter and 50 μm-thick plastic (CH) cylinders attached a10 µm-thick Cu plate on the rear surface. The axis of cylinder was invariably parallel to the coil axis. The position of the REB transport target was shifted from the coil plane (with horizontal and vertical offsets of the target centre with respect to the coil centre of H_{offset} = 70 μm, V_{offset} = 120 μm), and at the coil plane (H_{offset} = 0 μm, V_{offset} = 50 μm). The effect of 3D spatial distributions of the imposed external magnetic fields for REB transport can be explored. For each of the two configurations, the choice of t controlled the time allowed for B-field diffusion in the transport targets prior to REB injection, testing REB-transport in different conditions of target magnetization.

The diffusion time scale is is determined by the electrical conductivity and spatial size of the targets. According to the simulation, The B-field resistive diffusion inside the target at the B-field rises up to its peak value (rise-time of 1 ns, consistent with the duration of the LP-laser driver). The simulation results predicts that the B-field are fully diffused into the transport target in 1 ns and the spatial distribution inside the target is then similar to the distribution expected in vacuum at the target position. This diffusion time agrees with a simple of B-field diffusive time $\tau_{diff} = \mu_0 L^2/\eta \approx$ 1 ns over the length L = 50 μm of the target CH-layer assuming a constant resistivity = 10^6 S / m (expected for CH at 1 eV).

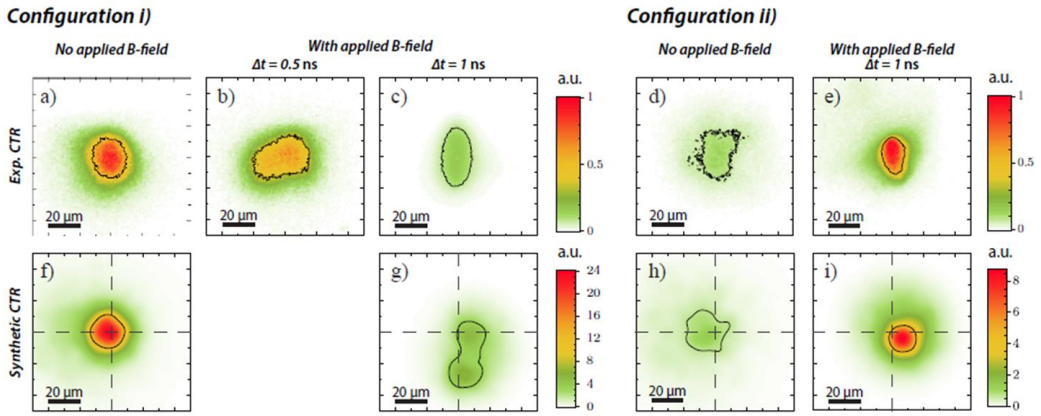

Figure 4.19 Experimentally obtained CTR patterns (first row) and synthetic CTR (second row), for the two configurations.
Images taken from Bailly-Grandvaux *et al.,* [21]

The REB transverse pattern after crossing the target thickness was investigated by imaging the Coherent Transition Radiation (CTR) emission from the rear surface at twice the laser frequency. The emitting surface was imaged at a 22.5 horizontal angle from the target normal into an optical streak camera used with a wide slit aperture as a fast gated 2D frame grabber.

In the case of without externally imposed B-field shown in Figure 4.18 (a) and (d), rather large fairly symmetrical CTR patterns (14.2 μm half width-half-maximum, HWHM) was observed. In the case of with the external B-field for the target configuration (i) and varying the delay of REB-injection, the CTR patterns are twisted and its yield is slightly weaker at Δt =0.5 ns shown in Figure 4.19 (b). The average size of the above case is comparable to the case without B-field. This is due to not fully as discussed above. At Δt =1 ns, significant CTR patterns were obtained different than the case without B-field, for both target positions (i) and (ii) [respectively Figure. 2-(c) and (e)]. The CTR-patterns are clearly narrower horizontally. Vertically, the signal is also narrower for conguration ii), while it is elongated for conguration (i). These correspond to half-height areas of equivalent radius 13 μm for conguration (i) and 9 μm for conguration (ii). The CTR yield decreased for conguration (i) and increased for conguration (ii) compared to signals without B-field case. As discussed above, the delay t = 1 ns corresponds to REB transport in magnetized targets. A 600 T field can radially confine the MeV electrons along the filed lines due to smaller Larmor radius than the REB initial radius.

The differences in the patterns shape and yield between conguration (i) and (ii) were observed. This is due to the B-field spatial distribution inside the transport targets, as shown in Figure 4-c)

and e). The reduction of CTR yield for conguration (i) can be explained further below by means of REB transport simulations. The REB momentum distribution inside the target is broadened by the B_y-component. As result, the REB propagation axis is deviated further away from the solid emission angle of the CTR. On the other hand, a radially-pinched CTR patterns were clearly observed in Figure 4. 18 (e) compared to Figure 4. 18 (d) in the case of conguration (ii) because of the symmetrical field distribution in the transport target. The significant enhancement of the CTR yield by a factor 6 compared to without the B-field case is direct evidence of the efficient REB transport by the external imposed B-field.

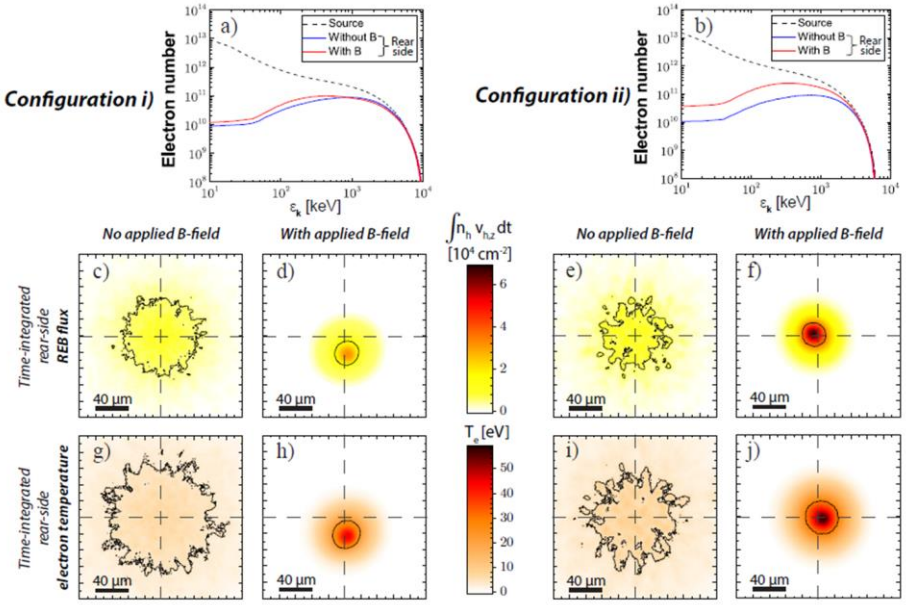

Figure 4.20 Computed REB energy distribution (first row), REB density flux at the rear side (second row) and background electron temperature (third row).
Images taken from Bailly-Grandvaux *et al.,* [21]

In order to estimate the REB density from experimentally obtained CTR patterns, a 3D particle-in-cell (PIC) hybrid simulation was performed. The initial total REB kinetic energy was set to 30% of the SP-laser energy on target. The REB with a 25 μm-radius (HWHM) corresponding to empiric factors 4 or 3 of the SP-laser focal spot size (HWHM), respectively for conguration (i) or (ii) was injected at the front surface of the target. The injected electron kinetic energy spectra were shown in Figure 4. 19 (a) and (b) for both configurations.

characterized by power laws for the low energy part 1:6k $\mu_0 L^2/\eta \approx$and exponential laws for the high energy part / exp (=Th) with Ti) h = 2 MeV and T (ii) h = 1:3MeV, as predicted by the ponderomotive potential for the corresponding laser parameters. The injected angular distribution of has a 30° mean divergence angle and a 55° dispersion angle. All the above geometric and energy REB source parameters are the same conditions compared to previous experiment. A post-processor for synthetic CTR-emission applied to the transport code output was used to compare with the experimentally obtained data. CTR is reconstructed by the coherently added transition radiation fields produced by each simulated macro-particle.

Synthetic CTR patterns are shown in Figure 4.19, which reproduces fairly well the experimentally obtained CTR patterns for various imposed B-field case. The ratio of CTR yield for both target configuration case are reproduced with 15 +/- 2% relative errors. The synthetic CTR for the imposed B-field case, the reconstructed pattern is in good agreement with the experimental data for configuration (i) and (ii). The experimentally obtained CTR radius with or without external B-field was reproduced with 15 +/- 5% relative errors, except for the imposed B-field case of configuration (i). The elliptic shape of the experimental signal is not exactly the same compared to the synthetic patterns with the relative error amounts to +/- 33%.

Figure 4.19 shows the simulation results of the REB energy flux (J/cm^2) at the rear surface of the 60 μm-thick targets for two target configurations. Figure 4. 20 (a) and (b) shows the computed electron energy distribution with (red line) and without (blue line) B-field, compared to the corresponding spectrum at the REB injection surface (dashed black). A large number of electrons with energy less than 100 keV are absorbed or scattered out of the simulation box before crossing the target. These are slightly moderated by the symmetric B-field in the case of configuration (ii). The radially pinched time-integrated REB flux patterns due to imposed external B-field are shown in Figure 4.19 (d) and (f). The peak intensity are increased by factors 15 and 20 and decreasing the beam mean radius by factor 3 and 2, respectively for configurations (i) and (ii). The filamented REB patterns are smoothed by the imposed external B-field compared to without B-field case, for both target configuration. The Figure 4.19 (g)-(j) shows the background electron temperature at the peak value, which is higher than the case without B-field by a factor 5.9 for both target configurations.

4.3.7 Integrated simulation for magnetized fast isochoric heating

4.3.2 Formation of moderated mirror magnetic fields [6]

A large mirror magnetic field ($R_m \sim 100$) is formed in the case of shell implosion due to large convergence ratio. Almost REB cannot reach the high-density region due to large mirror field. In contrast, the magnetic field lines are much smoother and the mirror ratio is smaller due to the small magnetic Reynolds number, and then the compression of the magnetic field is not efficient compared with the ideal magnetohydrodynamics case. This moderated field leads to efficient REB guiding. Simulation results are shown in Figure 4.10.

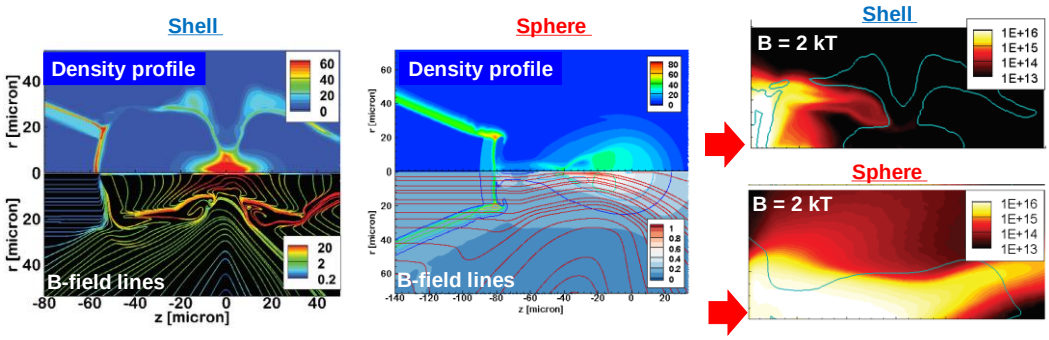

Figure 4.21 Computed two dimensional density profiles (upper left) and magnetic field lines (bottom left) for shell target at the maximum compression. Computed two dimensional density profiles (upper middle) and magnetic field lines (bottom left) for sphere target at the maximum compression. Spatial profile of REB energy density (erg / cm^3) for the case of shell and sphere target.
Images taken from Johzaki *et al.,* [6]

4.3.3 Efficient transport of low energy electron beams by elimination of the tip

The preceding shocks and rarefactions travelling ahead of the dense shell can be avoid by using a solid sphere target. A closed-tip enable to provide the efficient transport without preventing for inside the cone from filling with . In addition, a relatively cold and dense core can be produced stably by using the solid ball target. Figure 4.11 shows the simulated density profile and magnetic field lines of the sphere attached 'tipless' cone target at the maximum compression. Sharp boundary at the surface inner the cone is kept until maximum compression time.

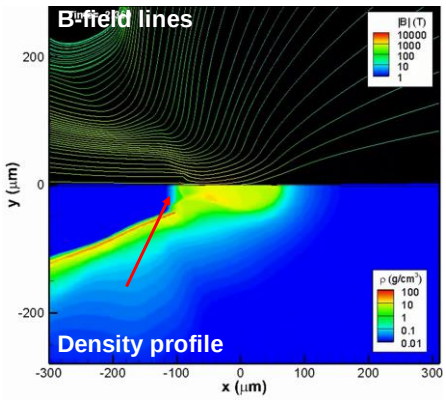

Figure 4.22 Two dimensional hydrodynamic simulation for sphere attached 'tipless' cone target. Performed by Prof. Nagatomo.

Figure 4.23 shows total REB energy transported after tip region for both cases. A significant reduction is seen in the case of with a 7 μm-thickness tip. On the other hand,

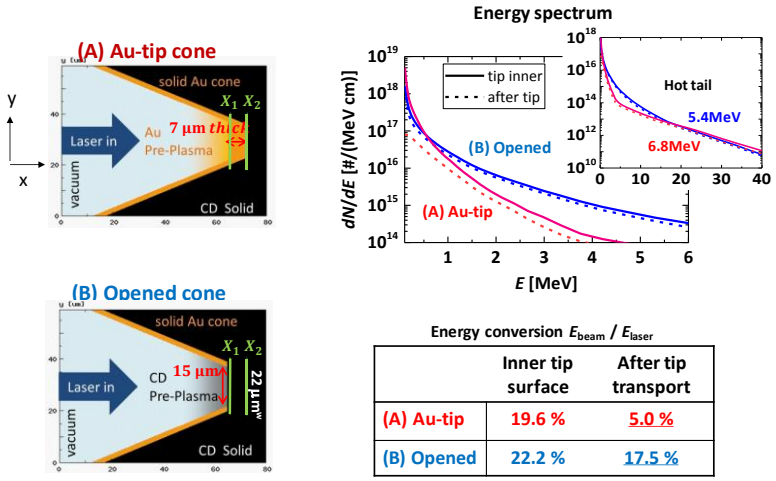

Energy conversion E_{beam} / E_{laser}

	Inner tip surface	After tip transport
(A) Au-tip	19.6 %	5.0 %
(B) Opened	22.2 %	17.5 %

Figure 4.23 Computed REB energy distribution in the case of with and without a tip (upper right). Total REB energy for different position (lower right).
Performed by Prof. Johzaki

4.3.4 Integrated simulation for magnetized fast laser heating

To enhance the core heating efficiency in fast ignition laser fusion, the concept of relativistic

electron beam guiding by external magnetic fields was evaluated by integrated simulations. Figure 4.20 show results of the integrated simulation.

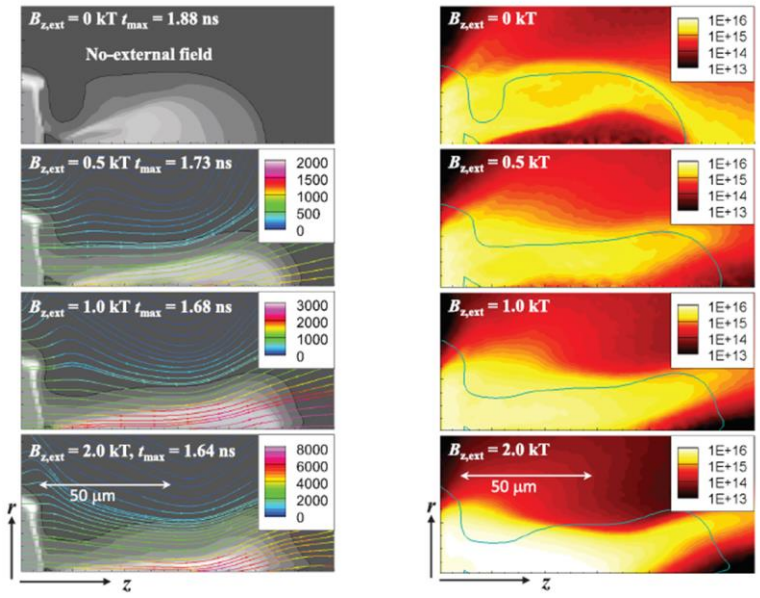

Figure 4.24 Magnetic field line profiles at the maximum compression for various strength (left). REB energy density (erg/cm^3) profiles at the peak intensity of REB for various strength (right).
Images taken from Johzaki *et al*., [6]

In the case without an external B-field, the REB is spatially diverged by the Biermann battery effect. the large angular spread. Around the central axis, there is a region where the beam energy density becomes low. Due to the REB heating, the direction of the bulk electron temperature gradient becomes non-parallel to that of the bulk electron density gradient around the dense core edge, which causes the Biermann battery fields in the direction to scatter the fast electrons.

In the case of $B_{z,ext}$ = 0.5 kT, the guided REB along magnetic field lines can be clearly seen. The external guiding fields suppresses the scattering effect due to the Biermann battery field. However, this magnetic fields ($B_{z,ext}$ = 0.5 kT) at the REB generation point cannot trap the MeV electrons efficiently. Besides, the shape of core is elongated by the external field [22]. The dramatically enhancement of the laser-to-core coupling by applying an external field is not observed. In the case of $B_{z,ext}$ = 1.0 kT, the guiding effect becomes significant than the case for $B_{z,ext}$ = 0.5 kT. However, the REB at the beam edge region are not sufficiently guided to the core,

even so more REB are guided to the core compared to the case of $B_{z,ext}$ = 0.5 kT. The laser-to-core coupling becomes clearly higher than the case for without an external field. For the further stronger imposed B-field case, the guiding effect becomes more remarkable.

4.5 Summary of Section 4

Three critical problems have been recognized as obstacles to the efficient fast heating. Energetic electron beams produced by interaction between a long scale plasma and a high intensity laser pulse, which cannot stop in the dense core plasma. The plasma mirror provides to eliminate a long scale pre-formed plasma

This work was performed by contribution

The author designed target and laser configuration for direct measurement of kilo-Tesla magnetic fields by laser-driven capacitor-coil target shown in ref. [19].

References in **Section4**

[1] T. Johzaki, H. Nagatomo, A. Sunahara, H.-B. Cai, H. Sakagami, Y. Nakao and K. Mima *Pre-plasma effects on core heating and enhancing heating efficiency by extended double cone for FIREX*. Nucl. Fusion **51**, 073022 (2011).

[2] Y. Arikawa, S. Kojima, A. Morace, M. Hata, **S. Sakata**, S. Fujioka, T. Kawashima, Y. Hironaka, K. Shigemori, Y. Abe, Z. Zhang, X. Vaisseau, S. Lee, T. Gawa, K. Matsuo, K.F.F. Law, Y. Kato, S. Matsubara, S. Tosaki, A. Yogo, H. Nagatomo, S. Tokita, Y. Nakata, T. Jitsuno, N. Miyanaga, J. Kawanaka, Y. Fujimoto, K. Yamanoi, T. Norimatsu, M. Nakai, H. Nishimura, H. Shiraga, FIREX GROUP, LFEX GROUP, H. Azechi, A. Sunahara, T. Johzaki, T. Ozaki and H. Sakagami *Improvement in the heating efficiency of fast ignition inertial confinement fusion through suppression of the preformed plasma*. Nucl. Fusion **57,** 066022 (2017).

[3] A. Morace, S. Kojima, Y. Arikawa, S. Fujioka, A. Yogo, S. Tosaki, **S. Sakata**, Y. Abe, S.H. Lee, K. Matsuo, A. Sagisaka, K. Kondo, A.S. Pirozhkov, T. Norimatsu, T. Jitsuno, N. Miyanaga, H. Shiraga, M. Nakai, H. Nishimura and H. Azechi *Plasma mirror implementation on LFEX laser for ion and fast electron fast ignition.* Nucl. Fusion **57**, 126018 (2017).

[4] W. Theobald, A.A. Solodov, C. Stoeckl, K.S. Anderson, F.N. Beg, R. Epstein, G. Fiksel, E.M. Giraldez, V. Yu. Glebov, H. Habara, S. Ivancic, L.C. Jarrott, F.J. Marshall, G. McKiernan, H.S.

McLean, C. Mileham, P.M. Nilson, P.K. Patel, F. Pe´rez, T.C. Sangster, J.J. Santos, H. Sawada, A. Shvydky, R.B. Stephens & M.S. Wei T*ime-resolved compression of a capsule with a cone to high density for fast-ignition laser fusion.* Nat. Commun. **5**, 5785 (2014).

[5] H. Sawada*,* S. Lee, T. Shiroto, H. Nagatomo, Y. Arikawa, H. Nishimura, T. Ueda, K. Shigemori, A. Sunahara, N. Ohnishi, F. N. Beg, W. Theobald, F. Perez, P. K. Patel and S. Fujioka *Flash Kα radiography of laser-driven solid sphere compression for fast ignition*. Appl. Phys. Lett. **108**, 254101 (2016).

[6] T. Johzaki*,* H. Nagatomo, A. Sunahara, Y. Sentoku, H. Sakagami, M. Hata, T. Taguchi, K. Mima, Y. Kai, D. Ajimi, T. Isoda, T. Endo, A. Yogo, Y. Arikawa, S. Fujioka, H. Shiraga and H. Azechi I*ntegrated simulation of magnetic-field-assist fast ignition laser fusion.* Plasma Phys. Control. Fusion **59,** 014045 (2017).

[7] J. S. Green*,* V. M. Ovchinnikov, R. G. Evans, K. U. Akli, H. Azechi, F. N. Beg, C. Bellei, R. R. Freeman, H. Habara, R. Heathcote, M. H. Key, J. A. King, K. L. Lancaster, N. C. Lopes, T. Ma, A. J. MacKinnon, K. Markey, A. McPhee, Z. Najmudin, P. Nilson, R. Onofrei, R. Stephens, K. Takeda, K. A. Tanaka,W. Theobald, T. Tanimoto, J. Waugh, L. Van Woerkom, N. C. Woolsey, M. Zepf, J. R. Davies, and P. A. Norreys *Effect of Laser Intensity on Fast-Electron-Beam Divergence in Solid-Density Plasmas*. Phys. Rev. Lett. **100**, 015003 (2008).

[8] C. Ren, M. Tzoufras, F. S. Tsung, W. B. Mori, S. Amorini, R. A. Fonseca, L. O. Silva, J. C. Adam, and A. Heron *Global Simulation for Laser-Driven MeV Electrons in Fast Ignition*. Phys. Rev. Lett. **93**, 185004 (2004).

[9] J. C. Adam, A. Heron, and G. Laval, *Dispersion and Transport of Energetic Particles due to the Interaction of Intense Laser Pulses with Overdense Plasmas*. Phys. Rev. Lett. **97**, 205006 (2006).

[10] S. Kar, A. P. L. Robinson, D. C Carroll, O Lundh, K. Markey, P. McKenna, P. Norreys, and M. Zepf *Guiding of Relativistic Electron Beams in Solid Targets by Resistively Controlled Magnetic Fields*. Phys. Rev. Lett. **102**, 055001 (2009).

[11] B. Ramakrishna, S. Kar, A. P. L. Robinson, D. J. Adams, K. Markey, M. N. Quinn, X. H. Yuan, P. McKenna, K. L. Lancaster, J. S. Green, R. H. H. Scott, P. A. Norreys, J. Schreiber, and M. Zepf *Laser-Driven Fast Electron Collimation in Targets with Resistivity Boundary*. Phys. Rev. Lett. **105**, 165001 (2010).

[12] H. Cai, S. Zhu and X. T. He *Effects of the imposed magnetic field on the production and transport of relativistic electron beams*. Phys. Plasmas **20**, 072701 (2013).

[13] D. J. Strozzi, M. Tabak, D. J. Larson, L. Divol, A. J. Kemp, C. Bellei, M. M. Marinak, and M. H. Key *Fast-ignition transport studies: Realistic electron source, integrated particle-in-cell and hydrody-dnamic modeling, imposed magnetic fields*. Phys. Plasmas **19**, 072711 (2012).

[14] W.-M. Wang P. Gibbon, Z.-M. Sheng and Y.-T. Li Magnetically Assisted Fast Ignition. *Phys. Rev. Lett*. **114**, 015001 (2015).

[15] T. Johzaki, H. Nagatomo, A. Sunahara, Y. Sentoku, H Sakagami5, M. Hata, T. Taguchi, K. Mima, Y. Kai, D. Ajimi, T. Isoda, T. Endo, A. Yogo, Y. Arikawa, S. Fujioka, H. Shiraga and H. Azechi *Integrated simulation of magnetic-field-assist fast ignition laser fusion*. Plasma Phys. Control. Fusion **59** 014045 (2017).

[16] H. Daido F. Miki, K. Mima, M. Fujita, K. Sawai, H. Fujita, Y. Kitagawa, S. Nakai, and C. Yamanaka *Generation of a strong magnetic field by an intense CO_2 laser pulse*. Phys. Rev. Lett. **56**, 846 (1986).

[17] S. Fujioka, Z. Zhang, K. Ishihara, K. Shigemori, Y. Hironaka, T. Johzaki, A. Sunahara, N. Yamamoto, H. Nakashima, T. Watanabe, H. Shiraga, H. Nishimura & H. Azechi *Kilotesla Magnetic Field due to a Capacitor-Coil Target Driven by High Power Laser*. Sci. Rep. **3**, 1170 (2013).

[18] J. J. Santos, M. Bailly-Grandvaux, L. Giuffrida, P. Forestier-Colleoni, S. Fujioka, Z. Zhang, P. Korneev, R. Bouillaud, S. Dorard, D. Batani, M. Chevrot, J. E. Cross, R Crowston, J-L. Dubois, J. Gazave, G. Gregori, E. d'Humières, S. Hulin, K. Ishihara, S. Kojima, E. Loyez, J-R. Marquès, A. Morace, P. Nicolaï, O. Peyrusse,A. Poyé, D. Raffestin, J. Ribolzi, M. Roth, G. Schaumann, F .Serres, V. T. Tikhonchuk, .P. Vacar and N. Woolsey *Laser-driven platform for generation and characterization of strong quasistatic magnetic fields*. New J. Phys. **17**, 083051 (2015).

[19] K. F. F. Law, M. Bailly-Grandvaux, A. Morace, **S. Sakata**, K. Matsuo, S. Kojima, S. Lee, X. Vaisseau, Y. Arikawa, A. Yogo, K. Kondo, Z. Zhang, C. Bellei, J. J. Santos, S. Fujioka and H. Azechi *Direct measurement of kilo-tesla level magnetic field generated with laser driven capacitor-coil target by proton deflectometry*. Appl. Phys. Lett. **108**, 091104 (2016).

[20] C. Goyon, B. B. Pollock, D. P. Turnbull, A. Hazi, L. Divol, W. A. Farmer, D. Haberberger, J. Javedani, A. J. Johnson, A. Kemp, M. C. Levy, B. Grant Logan, D. A. Mariscal, O. L. Landen, S. Patankar, J. S. Ross, A. M. Rubenchik, G. F. Swadling, G. J. Williams, S. Fujioka, K. F. F. Law, and J. D. Moody, *Ultrafast probing of magnetic field growth inside a laser-driven solenoid*. Phys. Rev. E **95**, 033208 (2017).

[21] M. Bailly-Grandvaux J.J. Santos , C. Bellei, P. Forestier-Colleoni, S. Fujioka , L. Giuffrida, J.J. Honrubia, D. Batani, R. Bouillaud, M. Chevrot, J.E. Cross, R. Crowston, S. Dorard, J.-L. Dubois, M. Ehret, G. Gregori, S. Hulin, S. Kojima, E. Loyez, J.-R. Marquès, A. Morace, Ph. Nicolaï1, M. Roth, **S. Sakata**, G. Schaumann, F. Serres, J. Servel, N. Woolsey & Z. Zhang *Guiding of relativistic electron beams in dense matter by laser-driven magnetostatic fields.* Nat. Commun. **9**, 102 (2018).

[22] K. Matsuo, H. Nagatomo, Z. Zhang, Ph. Nicolai, T. Sano, **S. Sakata**, S. Kojima, S. Lee, K.

F. F. Law, Y. Arikawa, Y. Sakawa, T. Morita, Y. Kuramitsu, S. Fujioka, and H. Azechi *Magnetohydrodynamics of laser-produced high-energy-density plasma in a strong external magnetic field* Phys. Rev. E **95**, 053204 (2017).

5. Magnetized fast isochoric laser heating for efficient creation of ultra-high-energy density states

Owing to the strong dependence of the ignition energy on the REB divergence, significant improvements to the collimation are a necessary requirement for making progress in FI research.

Here we have demonstrated enhanced laser-to-core energy coupling with the magnetized fast isochoric heating. The method employs a kilo-tesla-level magnetic field that is applied to the transport region from the REB generation point to the core which results in guiding the REB along the magnetic field lines to the core. 7.7 ± 1.3 % of the maximum coupling was achieved even with a relatively small radial area density core ($\rho R \sim 0.1$ g/cm^2). A simplified model coupled with the comprehensive diagnostics yields 6.2% of the coupling that agrees fairly with the measured coupling. This model also reveals that an ignition-scale areal density core ($\rho R > 0.3$ g/cm^2) leads to much higher laser-to-core coupling (> 10%), this coupling is much higher than that obtained with the current ICF scheme.

5.1 Magnetized fast isochoric laser heating for efficient creation of ultra-high-energy density states

5.1.1 Stable formation of high areal-density core plasma

Density profile measurement of pre-compressed Cu(II) oleate ball

Flash X-ray backlighting with monochromatic imager was used to measure two-dimensional density profiles of pre-compressed Cu(II) oleate solid balls under an external magnetic field. The experimental layout is shown in Figure 5.5 (left). The X-ray shadows of compressed cores were imaged using imaging plates with the same spherically bent quartz crystal used in the laser-to-core coupling experiment. The solid ball specifications and the laser parameters of the compression and magnetic field generation beams were also identical to those used in the laser-to-core coupling measurement. The LFEX laser was used for flash Cu-Ka X-ray backlight generation in this experiment.

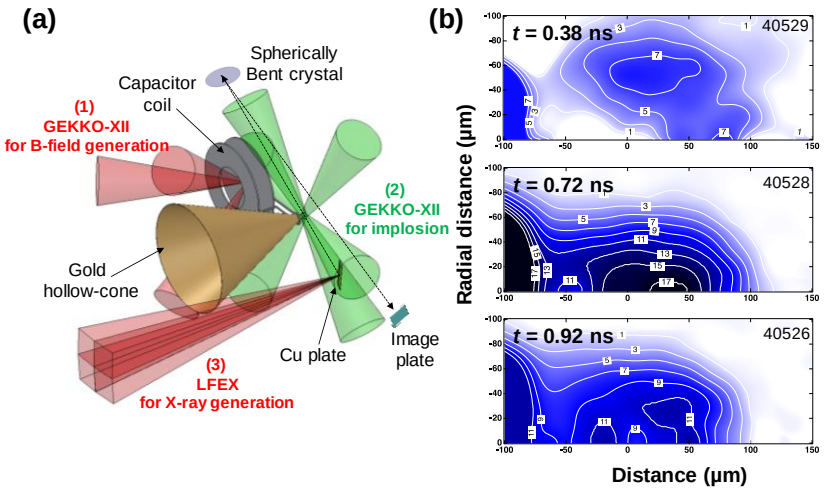

Figure 5.5 Experimental set up of X-ray flash backlight for density profile measurement. the core density profiles at t = +0.38, +0.72, and +0.92 ns.

The LFEX laser was defocused to produce a 350 μm-diameter spot on a 20 μm-thick Cu foil 3 mm behind the solid ball along the line of sight of the crystal imager to generate a large format backlight.

An X-ray shadow is converted to an X-ray transmittance profile by interpolating the backlight X-ray intensity profile within the core region from the outside of the core region. The area density of the pre-compressed core was calculated from the X-ray transmittance profile with a calculated opacity of 100 eV Cu(II) oleate for 8.05 keV X rays. A two-dimensional density profile of the core was obtained after applying an inverse Abel transformation to the area density profile, assuming rotational symmetry of the core along the cone axis. Figure 5.5 shows the core density profiles at t = +0.38, +0.72, and +0.92 ns. The converging shock wave was still travelling to the center of the ball at t = +0.38 ns, maximum compression was reached at around t = +0.72 ns, and the core had already begun to disassemble at t = +0.92 ns. The area densities and average density of the core along the REB path were, respectively, rL = 0.08 g/cm2 and r = 5.7 g/cm^3 at t = +0.38 ns, rL = 0.16 g/cm^2 and r = 11.3 g/cm^3 at t = +0.72 ns. These values were used in the calculation of the correlation factor described in the next section.

5.1.2 Experimental setup for the laser-to-core coupling measurement

The experiment was conducted on the GEKKO-LFEX laser facility at the Institute of Laser Engineering, Osaka University. The fusion fuel surrogate was made of a 200 μm-diameter solid Cu(II) oleate ball [$Cu(C_{17}H_{33}COO)_2$], whose surface was coated with a 25 μm-thick polyvinyl alcohol (PVA) layer to prevent the Cu atoms from being ionized directly by the compression beams. The Cu(II) oleate contains 9.7% Cu atoms in weight for visualization of the relativistic electron beam (REB) transport in the core and for measurement of the laser-to-core energy coupling. The fuel surrogate was attached to the Au cone, whose open angle, wall thickness, and tip diameter were 45 degree, 7 μm, and 100 μm respectively. The outer surface of the Au cone was coated with a 50 μm thick PVA layer to delay the cone breakup time. Open-tip or closed-tip Au cones were used in the experiments; the tips of the closed Au cones were covered with a 7 μm-thick Au layer.

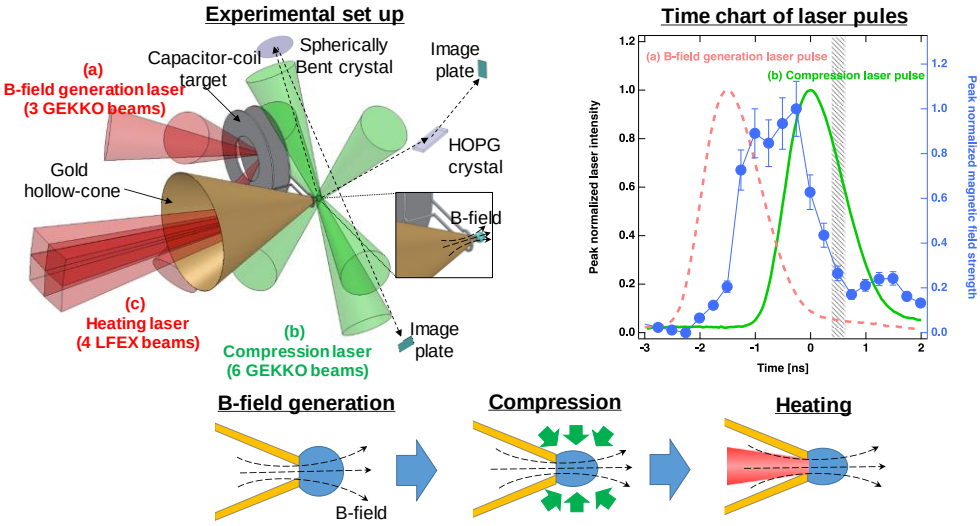

Figure 5.9 (a) A schematic drawing of the experimental layout for the magnetized fast isochoric heating. (b) Timing chart of the magnetic field generation laser (pink broken line), fuel compression laser (green solid line) and laser-produced magnetic field (blue circular marks) pulses. The hatching area indicates the injection timing of the heating laser.

The solid ball was compressed by six GEKKO-XII laser beams, whose wavelength, pulse shape, pulse duration, and energy were 526 nm, Gaussian, 1.3 ns full width at half maximum (FWHM), and 240 ± 15 J / beam, respectively. The center of the nickel-made coil, which had a 500 μm diameter, was located 230 μm from the center of the ball to generate a strong magnetic field near the REB generation point and the solid ball.

The first disk of the laser-driven capacitor was irradiated through the hole of the second disk by three tightly focused GEKKO-XII laser beams, whose wavelength, pulse shape, pulse duration, and energy were 1053 nm, Gaussian, 1.3 ns (FWHM), and 600 ± 20 J / beam, respectively.
The tip of the cone was irradiated to produce a REB by four LFEX laser beams, whose wavelength, pulse shape, and pulse duration were 1053 nm, Gaussian, 1.8 ± 0.3 ps (FWHM), respectively. The total energy of the four LFEX beams on the tip was varied from 620 to 1500 J. The focal spot diameter was 50 μm (FWHM) and contained 30% of the total energy, producing an average intensity of 9×10^{18} W/cm^2 at the maximum energy shot. The time origin (t = 0 ns) is defined as the peak of the compression laser pulse. The peak of the magnetic field generation laser pulse was set to t = –1.5 ns, and the heating 3 laser was injected in the time window (t = +0.38 – +0.72 ns) around the maximum compression timing.

5.1.3 Two dimensional Cu-Kα emission profiles

Figure 3 shows two dimensional Cu-Kα emission profiles and density profiles of the pre-compressed core at two different timings (t = 0.40 +/- 0.03 ns and 0.67 +/- 0.05 ns) and also the comparison of Cu-Kα emission profiles between with and without the external magnetic field application at the two different timings.

Here the density profiles were measured in separate experiments that are explained in the Supplement. These images were obtained after applying an inverse Abel transformation to the area density profile, assuming rotational symmetry of the core along the cone axis. The Cu-Kα emission profile reflects the energy deposition rate in the core.

Copper Kα X-rays (8.05 keV) were imaged using a spherically bent quartz (2131) crystal to visualize the transport of the REB in a pre-compressed core from the direction perpendicular to the LFEX incident axis. The magnification, spatial resolution, and spectral bandwidth were 20, 13 μm (FWHM), and 5 eV (FWHM), respectively.

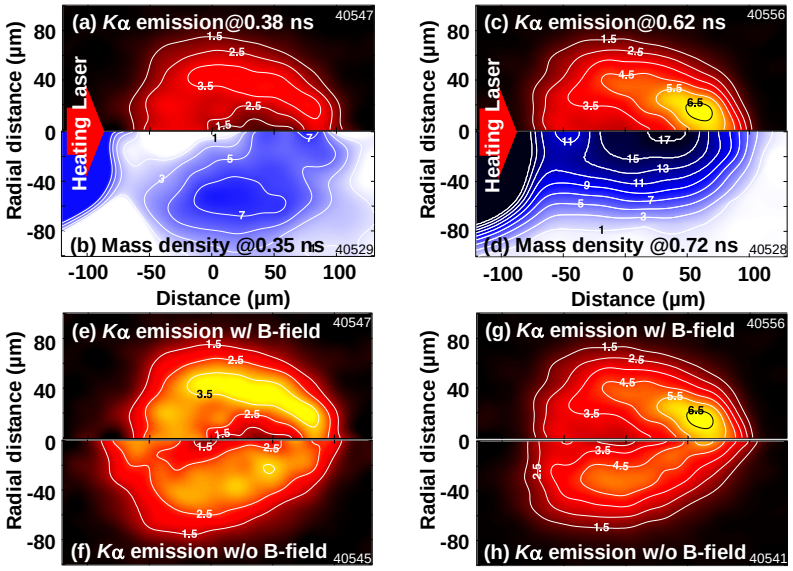

Figure 5.10 Two dimensional profiles of Cu-Kα emission (a,c,e,g) and mass density (b,d) measured in the experiments with the application of the external magnetic field at t = 0.40 ± 0.03 ns (a, b, e) and t = 0.67 ± 0.05 ns (c,d,g). Cu-Kα emission profiles are compared between those obtained with (e,f) and without (g,h) application of the external magnetic field at two different injection timings. The Cu-Kα emission profiles (a, c, g, h) are drawn with the same color scale excepting for (e) and (f). These images were obtained after applying an inverse Abel transformation to the area density profile, assuming rotational symmetry of the core along the cone axis.

Table 1: Summary of laser-to-core coupling efficiencies

Shot ID	**Cone Tip Condition**	**Heating Energy** [J]	**Compression Energy** [J]	**B-generation Energy** [J]	**Heating Timing** [ns]	**Cu-Kα number** [photons/sr]	**Coupling Efficiency** [%]
40545	Open	899	1422	**N/A**	0.42	5.58×10^{11}	2.9 ± 0.5
40541	Open	683	1428	**N/A**	0.65	5.53×10^{11}	3.9 ± 0.7
40558	Open	1516	1386	1761	0.4	1.19×10^{12}	3.1 ± 0.5
40556	Open	1016	1332	1698	0.61	1.02×10^{12}	4.3 ± 0.8
40547	Open	1100	1530	1824	0.38	1.28×10^{12}	5.5 ± 1.0
40549	Open	668	1548	1794	0.37	7.29×10^{11}	5.8 ± 1.0
40543	Open	625	1494	1842	0.72	9.32×10^{11}	7.7 ± 1.3
40560	**Close**	1523	1404	1794	0.38	8.23×10^{11}	2.5 ± 0.4
40562	**Close**	1378	1374	1725	0.65	7.96×10^{11}	2.7 ± 0.5

Table 5.1 Summary of laser-to-core coupling efficiensies.

At t = 0.40 0.03 ns, the converging shock wave was still travelling to the center of the ball, and the shock front is clearly observable in Figure 5.10 (b). Strong Cu-Kα emission region locates near the shock front in Figure 5.10 (a, e). Externally applied magnetic field lines were accumulated in the downstream of the shock wave, therefore REB was guided to the shock compressed region along the field lines. This feature was not observed without the external magnetic field as shown in Figure 5.10 (f). At t = 0.67 0.05 ns, the solid ball reached the maximum compression. The strong Cu-Kα emission spot appeared at 50 μm longitudinal distance, which was more than 100 μm away from the REB generation point namely the cone tip as shown in Figure 5.10 (c, g). This Cu-Kα emission feature is the evidence of REB guiding by the externally applied magnetic field as well as significant enhancement of the laser-to-core coupling. This strong emission spot disappeared, when the external magnetic field was not applied, as shown in Figure 5.10 (h). Energy shift of the Cu-Kα X ray due to ionization of Cu atoms in a hot core could be the reason why the Cu-Kα emission was weak in the core central region.

5.1.4 Derivation of correlation factor between Cu-Kα photons and deposited REB energy

The X-ray spectrometer, which utilizes a planar highly oriented pyrolytic graphite (HOPG), was installed at 40 deg. from the LFEX incident axis to measure the absolute Cu-Ka yield. The absolute integral reflectance of the HOPG was measured using an Xray diffractometer with an accuracy of ±15%. The spectral resolution of the spectrometer was 17.9 eV (FWHM). Figure 5.11 shows example Cu-Kα spectra. The vertical error bar corresponds to the error in the integral reflectance measurement, and the horizontal error bar is equal to the spectral resolution. The Cu-Kα photon yields were integrated within the energy range of 8.0 keV to 8.1 keV after Bremsstrahlung X-ray background subtraction.

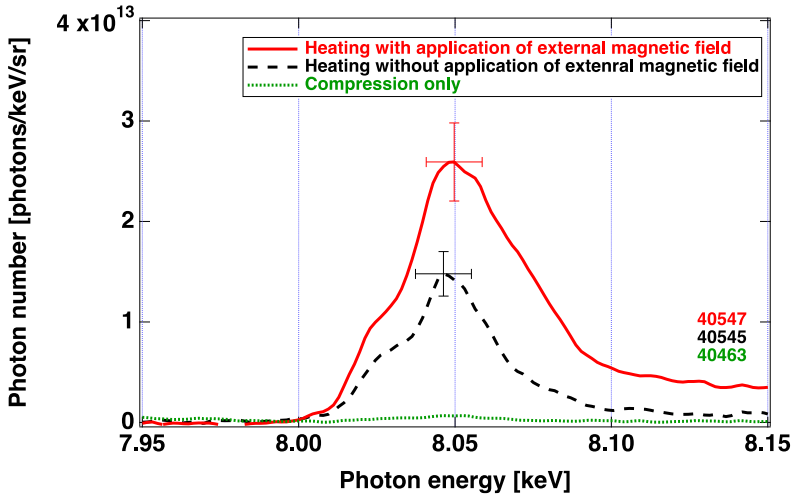

Figure 5.11 Example Cu-Ka spectra peaked at 8.05 keV. Red solid, black dashed, and green dotted lines are, respectively, spectra obtained by heating with application of external magnetic field, heating without the application, and only fuel compression. The vertical error bar corresponds to the 15% error in the absolute integrated reflectance of the HOPG. The horizontal error bar is equal to 17.9 eV of the spectral resolution of the spectrometer. The Cu-Kα photon yields were integrated within the energy range of 8.0 keV to 8.1 keV.

Cross-sections of electron-impact K-shell ionization have similar a dependence on electron energy as collisional energy loss. The two are essentially the same process but with a different threshold energy. The energy deposited from the REB to the core can be obtained from absolute Cu-Kα photon yields using a correlation factor between Cu-Kα yield (photons/sr) and deposited REB energy (J). We have derived the correlation factor (J/photons/sr) for the core produced in this experiment. The Solodov model was used to calculate the mass stopping power S(E) of the REB in a core. Both Davies and Hombourger models were used to calculate the electron-impact K-shell ionization cross-section σKα (E). The differences in cross-section between the two models are considered to be model-dependent errors. The ratio between the stopping power and K-shell ionization cross section is the correlation factor (C). Note that the Hombourger model gives a 1.3 times higher correlation factor than the Davies model. The correlation factor C is defined as follows,

$$C = \frac{\int_0^L \int_{10\ \mathrm{keV}}^{1\ \mathrm{GeV}} \varepsilon_{dep}(E,x)\,dE\,dx}{\int_0^L \int_{10\ \mathrm{keV}}^{1\ \mathrm{GeV}} P_{K\alpha}(E,x)\,dE\,dx} = \frac{\int_0^L \int_{10\ \mathrm{keV}}^{1\ \mathrm{GeV}} \upsilon(E,x) f(E,x) S(E,\rho)\,dE\,dx}{\int_0^L \int_{10\ \mathrm{keV}}^{1\ \mathrm{GeV}} \upsilon(E,x) f(E,x) n_{cu} \sigma_{K\alpha}(E)/4\pi\,dE\,dx} \qquad (5\text{-}1)$$

where $\varepsilon_{dep}(E, x)$, $P_{K\alpha}(E, x)$, $v(E, x)$, $f(E, x)$, ρ, and n_{Cu} are the total deposited energy by the REB to the dense core, the probability of Cu-Kα emission, the relativistic electron velocity, the REB energy distribution, the mass density of the Cu (II) oleate solid ball, and the number density of Cu atoms, respectively. The initial REB energy distribution was a Boltzmann function as $f(E, 0) = \exp(-E/T_{REB})$ at the generation point ($x = 0$), here TREB is the slope temperature of the energy distribution. Slowing down of the REB during the transport was calculated as $f(E, x+dx) = f(E + |\varepsilon_{dep}(E,x)|dx, x)$.

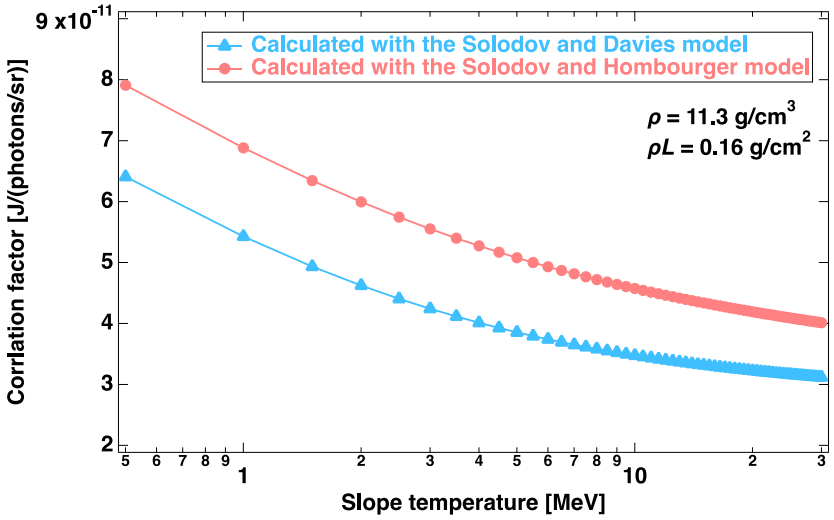

Figure 5.12 Dependence of the correlation factor between the deposited energy (J) and Cu-Ka yield (photons/sr) on the REB slope temperature. The data were calculated using the Davies (blue circular marks) and Hombourger (red triangular marks) models of electron-impact K-shell ionization for a 11.3 g/cm3 and 0.16 g/cm2 Cu(II) oleate, which correspond to the average core density and area density at t = 0.72 ns (maximum compression timing).

Figure 5.12 shows the calculated correlation factor at different REB slope temperatures (T_{REB}) for a 11.3 g/cm3 Cu(II) oleate plasma, which is equal to the average core density observed at t = +0.72 ns. The correlation factor also depends weakly on the core density. The spatial fluctuation of the core density observed in Fig. S2(b) took into account the correlation factor derivation as an error of the correlation factor. Dependence of the correlation factor on TREB must be considered in the coupling evaluation. Energy distributions of electrons that escaped from the plasma into vacuum were measured using an electron energy analyzer positioned along the LFEX incident axis. Although the energy distribution of the vacuum electrons is not exactly identical to that at

the generation point due to scattering, absorption, and reflection by the cone, core, and spontaneous electromagnetic field, we found that the slope temperatures of the escaped electrons are close to those in the transport region estimated from Bremsstrahlung X-ray spectra. Therefore, the energy distribution of the measured vacuum electrons was used in the following analysis.

The energy distribution of the escaped electrons was fitted with a two-temperature Boltzmann distribution function as $f(E) = A \exp(-E/T_{REB1}) + (1-A) \exp(-E/T_{REB2})$, where A and E are the intercept and electron energy, and TREB1 < TREB2. The correction factor (C) is finally given with correlation factors for two temperatures [$C(T_{REB1})$,

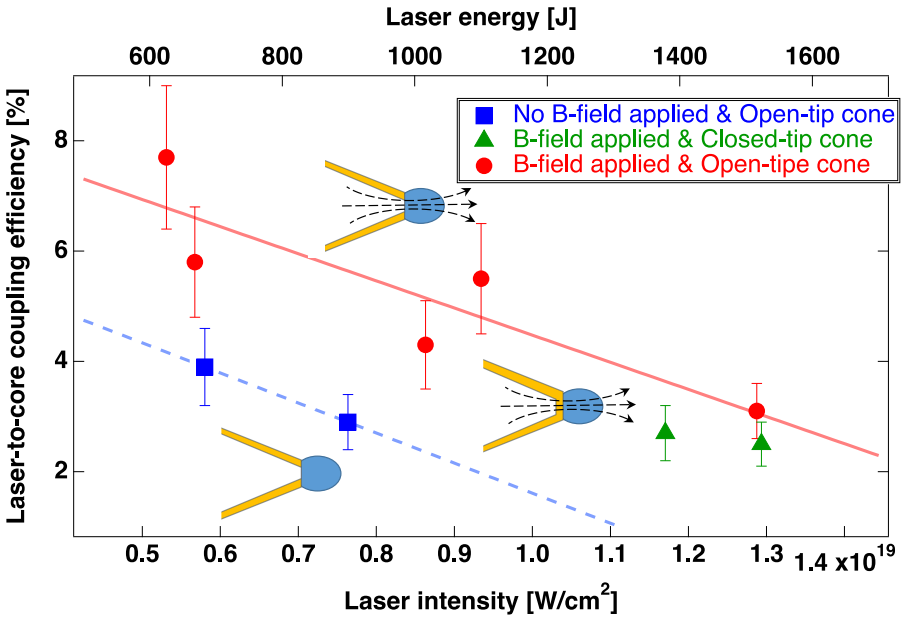

Figure 5.13 Dependence of laser-to-core energy coupling on heating laser intensity (bottom axis) and energy (top axis). The blue rectangular, green triangle and red circle marks represent laser-to-core coupling efficiencies obtained with the following conditions; no application of external-magnetic-field with open-tip cone, application of external magnetic field with closed-tip cone, and application of external magnetic field with open-tip cone, respectively.

The correlation factor calculated for each shot is summarized in Table S1 along with other measured parameters. The error in the deposited energy was evaluated taking into account the difference in the correlation factor between the ionization models, density fluctuations in the core, and the error in the integral reflectance of the HOPG.

The laser-to-core coupling () can be simplified as a product of laser-to-REB energy conversion

efficiency (REB), REB collision probability (coll), and energy deposition rate of REB in the core (dep). The previous experiments show REB = 0.4 and coll = 0.7. dep = 0.22 was calculated by the simplified model with the measured area density and REB temperatures written in the Supplement, yielding = REB coll dep = 6.2%. This simple evaluation seems consistent fairly with the measured coupling (7.7 +/- 1.3 %), and the simple evaluation reveals that higher area density core leads to higher laser-to-core coupling.

An energy density increment of the heated core is close to 1 Gbar, which corresponds to 50 J of the energy deposition in a 100 μm-diameter spherical volume. An ultra-high-energy density state could be efficiently created by the magnetized fast isochoric heating.

5.1.4 Initial magnetic field profile

An externally applied magnetic field penetrates diffusively into the target from the outside. The diffusion time scale is determined by the electrical conductivity and spatial size of the targets. Based on a previous study, the externally applied magnetic field is guaranteed to penetrate rapidly into an "insulator" hydrocarbon, however, the diffusion dynamics of the magnetic field into the gold cone remain unclear. The temporal change in magnetic field strength drives a diamagnetic current in the gold cone, and the current ohmically heats the gold. The electrical conductivity of a material is not well understood in the warm-dense-matter state, which the gold cone may access during the magnetic field diffusion. The magnetic diffusion time (t_{diff}) is expressed as $t_{diff} = \mu_0 s L^2$, where μ_0, s, and L are the permeability, electrical conductivity, and diffusion layer thickness, respectively. For a 7 μm gold cone wall, the diffusion times are tdiff = 2.5 ns, 120 ps and 60 ps at room temperature (s = 4×10^7 S/m), 0.1 eV (s = 2×10^6 S/m) and 1 eV (s = 1×10^6 S/m), respectively (14). The small temperature increment helps to rapidly soak the cone in the magnetic field.

250 kA of current was generated with a capacitor-coil target driven by one GEKKO-XII beam, which was measured using proton radiograph. 430 kA of current, which is 3 times larger than that generated with one beam, can be driven by using three GEKKO-XII beams. Figure S3 shows the two-dimensional profile of the magnetic field calculated at the maximum magnetic field strength timing generated using a 430 kA Gaussian current pulse with a 1 ns (FWHM) pulse width. The profiles were calculated using two different electrical conductivities (s = 4×10^7 and 10^6 S/m) and neglecting temporal changes in the temperature, density, and conductivity of the gold cone. The magnetic field strength around the tip was 320 and 640 T, respectively.

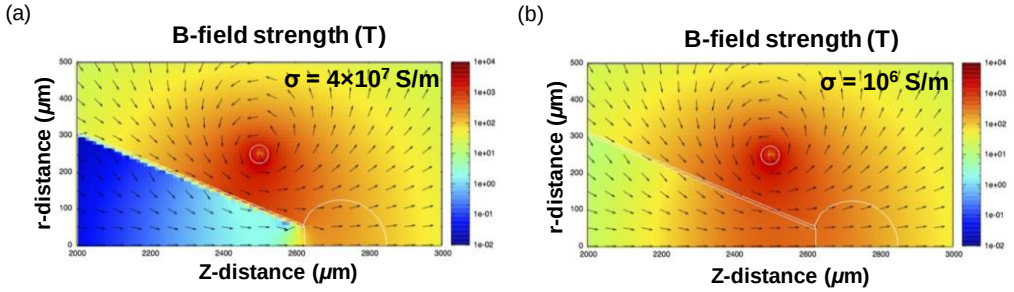

Figure 5.14 Two-dimensional profile of the magnetic field generated with a coil, in which 430 kA of current flows at the field peak timing. The magnetic field diffusion was taken into account using two electrical conductivities [(a) s = 4×10^7 S/m and (b) 2×10^6 S/m].

5.2 Scaling for ignition

[]

Section1

Uniform density

Ignition energy E_{ig} and intensity I_{ig} can be expressed as a function of the density

$$E_{ig} = E_{opt} = 140\left(\frac{\rho}{100\ \mathrm{g/cm^3}}\right)^{-1.85}\ \mathrm{kJ} \tag{5-1}$$

$$I_{ig} = I_{opt} = 2.4\times10^{19}\left(\frac{\rho}{100\ \mathrm{g/cm^3}}\right)^{0.95}\ \mathrm{W/cm^2} \tag{5-1}$$

$$t_p = t_{opt} = 54\left(\frac{\rho}{100\ \mathrm{g/cm^3}}\right)^{-0.85}\ \mathrm{ps} \tag{5-1}$$

$$r_b = r_{opt} \simeq 60\left(\frac{\rho}{100\ \mathrm{g/cm^3}}\right)^{-0.97}\ \mu\mathrm{m} \tag{5-1}$$

$$E_{ig} \geq E_{opt}(\rho) \times \max\left(1, \frac{\mathcal{R}}{\mathcal{R}_0}\right) \times \begin{cases} \max\left(1; \dfrac{r_b}{r_{\mathrm{opt}}}\right), & r_b \leq 2.5 r_{\mathrm{opt}} \\ 2.5\left(\dfrac{r_b}{2.5 r_{\mathrm{opt}}}\right)^2, & r_b \geq 2.5 r_{\mathrm{opt}} \end{cases} \tag{5-1}$$

$$I_{ig} \geq I_{opt}(\rho) \times \max\left(1, \frac{\mathcal{R}}{\mathcal{R}_0}\right) \times \begin{cases} \min\left(1; \dfrac{r_b}{r_{\mathrm{opt}}}\right), & r_b \leq 2.5 r_{\mathrm{opt}} \\ 0.4, & r_b \geq 2.5 r_{\mathrm{opt}} \end{cases} \tag{5-1}$$

$$T_{\mathrm{hot}} = \left[\frac{I_{\mathrm{ig}}^{\mathrm{laser}}}{1.2 \times 10^{19}\ \mathrm{W/cm^2}} \left(\frac{\lambda_{\mathrm{ig}}}{1.06\ \mu\mathrm{m}}\right)^2\right]^{1/2} \ \mathrm{MeV} \tag{5-1}$$

$\mathcal{R}(\mathrm{g/cm^2}) = 0.6 T_{\mathrm{hot}}\ (\mathrm{MeV})$

$$\mathcal{R} = 0.55 f_{\mathcal{R}} \frac{\lambda_{\mathrm{ig}}}{1.06\ \mu\mathrm{m}} \left(\frac{I_{\mathrm{ig}}^{\mathrm{laser}}}{1.2 \times 10^{19}\ \mathrm{W/cm^2}}\right)^{1/2} \ \mathrm{g/cm^2} \tag{5-1}$$

Figure 4.1 in Section 4.1

Two slope temperature

$$\mathcal{R} = 0.55 f_{\mathcal{R}} \frac{\lambda_{\mathrm{ig}}}{1.06\ \mu\mathrm{m}} \left(\frac{I_{\mathrm{ig}}^{\mathrm{laser}}}{1.2 \times 10^{19}\ \mathrm{W/cm^2}}\right)^{1/2} \ \mathrm{g/cm^2} \tag{5-1}$$

References in **Section5**

[1] N. Miyanaga *et al.,* 10-kJ PW laser for the FIREX-I program. *J. Phys. IV France* **133**, 81-87 (2006).

[2] Y. Iwasa *et al.,* Cu-oleate microspheres fabricated by emulsion method as novel targets for

fast ignition laser fusion experiments. *Fusion Eng. Des*. **125**, 89-92 (2017).

[3]

[4]

6. Conclusion

The quest for the inertial confinement fusion (ICF) ignition is a grand challenge, as exemplified by extraordinary large laser facilities. Fast isochoric heating of a pre-compressed plasma core with a high-intensity short-pulse laser is an attractive and alternative approach to create ultra-high-energy-density states like those found in ICF ignition sparks. This avoids the ignition quench caused by the hot spark mixing with a surrounding cold fuel, which is a crucial problem of the currently pursued ignition scheme. High-intensity lasers efficiently produce relativistic electron beams (REB). A part of the REB kinetic energy is deposited in the core, and then the heated region becomes the hot spark to trigger the ignition. However, only a small portion of the REB collides with the core because of its large divergence.

Here we have demonstrated enhanced laser-to-core energy coupling with the magnetized fast isochoric heating. The method employs a kilo-tesla-level magnetic field that is applied to the transport region from the REB generation point to the core which results in guiding the REB along the magnetic field lines to the core. 7.7 ± 1.3 % of the maximum coupling was achieved even with a relatively small radial area density core ($\rho R \sim 0.1$ g/cm^2). The guided REB transport was clearly visualized in a pre-compressed core by using Cu-Kα imaging technique. A simplified model 17 coupled with the comprehensive diagnostics yields 6.2% of the coupling that agrees fairly with the measured coupling. This model also reveals that an ignition-scale areal density core ($\rho R > 0.3$ g/cm^2) leads to much higher laser-to-core coupling (> 10%), this coupling is much higher than that obtained with the current ICF scheme.

Publications

1. **S. Sakata**, S. Lee, T. Johzaki, H. Sawada, Y. Iwasa, H. Morita, K. Matsuo, K. F. F. Law, A. Yao, M. Hata, A. Sunahara, S. Kojima, Y. Abe, H. Kishimoto, A. Syuhada, T. Shiroto, A. Morace, A. Yogo, N. Iwata, M. Nakai, H. Sakagami, T. Ozaki, K. Yamanoi, T. Norimatsu, Y. Nakata, S. Tokita, J. Kawanaka, N. Miyanaga, H. Shiraga, K. Mima, H. Nishimura, M. Bailly-Grandvaux, J. Santos, H. Nagatomo, H. Azechi, R. Kodama, Y. Arikawa, Y. Sentoku and S. Fujioka 「Magnetized Fast Isochoric Laser Heating for Efficient Creation of Ultra-High-Energy-Density States」*arXiv* 1712.06029 (2017). (under review in *Nature*)

2. **S. Sakata**, Y. Arikawa, S. Kojima, T. Ikenouchi, T. Nagai, Y. Abe, H. Inoue, A. Morace, M. Utsugi, R. Kato, H. Nishimura, M. Nakai, H. Shiraga, S. Fujioka, and H. Azechi 「Photonuclear reaction based high-energy x-ray spectrometer to cover from 2 MeV to 20 MeV」*Rev. Sci. Instrum.* **85**, 11D629 (2014).

3. **S. Sakata**, Y. Arikawa, S. Kojima, Y. Abe, T. Nagai, H. Inoue, R. Kato, M. Nakai, H. Shiraga, H. Azechi 「Development of the High Energy Bremsstrahlung X-Ray Spectrometer by Using (γ, n) Reaction」*Plasma and fusion Research*: Regular articles, **9**, 4404112 (2014).

4. K. F. F. Law, M. Bailly-Grandvaux, A. Morace, **S. Sakata**, K. Matsuo, S. Kojima, S. Lee, X. Vaisseau, Y. Arikawa, A. Yogo, K. Kondo, Z. Zhang, C. Bellei, J. J. Santos, S. Fujioka, and H. Azechi「Direct measurement of kilo-tesla level magnetic field generated with laser-driven capacitor coil target by proton deflectmetry」*Appl. Phys. Lett*. **108** (9), 091104 (2016).

5. S. Kojima, T. Ikenouchi, Y. Arikawa, **S. Sakata**, Z. Zhang, Y. Abe, M. Nakai, H. Nishimura, H. Shiraga, T. Ozaki, S. Miyamoto, M. Yamaguchi, A. Takemoto, S. Fujioka and H. Azechi Development of Compton X-ray spectrometer for high energy resolution single-shot high-flux hard X-ray spectroscopy」*Rev. Sci. Instrum.* **87**, 043502 (2016).

6. Y. Arikawa, T. Nagai, Y. Abe, S. Kojima, **S. Sakata**, H. Inoue, M. Utsugi, Y. Iwasa, T. Murata, N. Sarukura, M. Nakai, H. Shiraga, S. Fujioka and H. Azechi「Development of multichannel low-energy neutron spectrometer」*Rev. Sci. Instrum.* **85**, 18C513 (2014).

7. K. Matsuo, H. Nagatomo, Z. Zhang, Ph. Nicolai, T. Sano, **S. Sakata,** S. Kojima, S. Lee, K. F. F. Law, Y. Arikawa, Y. Sakawa, T. Morita, Y. Kuramitsu, S. Fujioka, and H. Azechi 「Magnetohydrodynamics of laser-produced high-energy-density plasma in a strong external

magnetic field」*Phys. Rev.* E **95**, 053204 (2017).

8. S. Fujioka, T. Johzaki, Y. Arikawa, Z. Zhang, A. Morace, T. Ikenouchi, T. Ozaki, T. Nagai, Y. Abe, S. Kojima, **S. Sakata**, H. Inoue, M. Utsugi, S. Hattori, T. Hosoda, S. H. Lee, K. Shigemori, Y. Hironaka, A. Sunahara, H. Sakagami, K. Mima, Y. Fujimoto, K. Yamanoi, T. Norimatsu, S. Tokita,Y. Nakata, J. Kawanaka, T. Jitsuno, N. Miyanaga, M. Nakai, H. Nishimura, H. Shiraga, H. Nagatomo, and H. Azechi,「Heating Efficiency Evaluation with Mimicking Plasma Conditions of Integrated Fast-Ignition Experiment」*Phys. Rev.* E **91**, 063102 (2015).

9. S. Fujioka, Y. Arikawa, S. Kojima, T. Johzaki, H. Nagatomo, H. Sawada, S. H. Lee, T. Shiroto, N. Ohonishi, A. Morace, X. Vaisseau, **S. Sakata**, Y. Abe, K. Matsuo, K. F. F. Law, S. Tosaki, A. Yogo, K. Shigemori, Y. Hironaka, Z. Zhang, A. Sunahara, T. Ozaki, H. Sakagami, K. Mima, Y. Fujimoto, K. Yamanoi, T. Norimatsu, S. Tokita, Y. Nakata, J. Kawanaka, T. Jitsuno, N. Miyanaga, M. Nakai, H. Nishimura, H. Shiraga, K. Kondo, M. Bailly-Grandvaux, C. Bellei and H. Azechi,「Fast ignition realization experiment with high-contrast kilo-joule peta-watt LFEX laser and strong external magnetic field」*Phys. Plasmas* **23**, 056308 (2016).

10. M. Bailly-Grandvaux, J.J. Santos,, C. Bellei, P. Forestier-Colleoni, S. Fujioka, L. Giuffrida, J.J. Honrubia, D. Batani,1 R. Bouillaud, M. Chevrot, J.E. Cross, R. Crowston, S. Dorard, J.-L. Dubois, M. Ehret, G. Gregori, S. Hulin, S. Kojima, E. Loyez, J.-R. Marques, A. Morace, Ph. Nicolai, M. Roth, **S. Sakata**, G. Schaumann, F. Serres, J. Servel, V.T. Tikhonchuk, N.Woolsey, and Z. Zhang「Guiding of relativistic electron beams in dense matter by laser-driven magnetostatic fields」accepted in *Nat. commun.*

Awards

1. プラズマ・核融合学会賞　若手学会発表賞 「高速点火核融合実験における高エネルギーX 線スペクトル計測」 2013 年 12 月 6 日 第 2013 若手 03 号

2. 第 10 回 核融合エネルギー連合講演会　若手優秀発表賞「高速点火核融合実験における光核反応を用いた高エネルギーX 線分光計測」2014 年 6 月 20 日 第 2014 連講 07 号

3. レーザー学会学術講演会第 37 回年次大会　優秀論文発表賞 「外部磁場導入による高点火方式レーザー核融合の加熱効率向上の実証」2017 年 1 月 9 日 09aVI04